

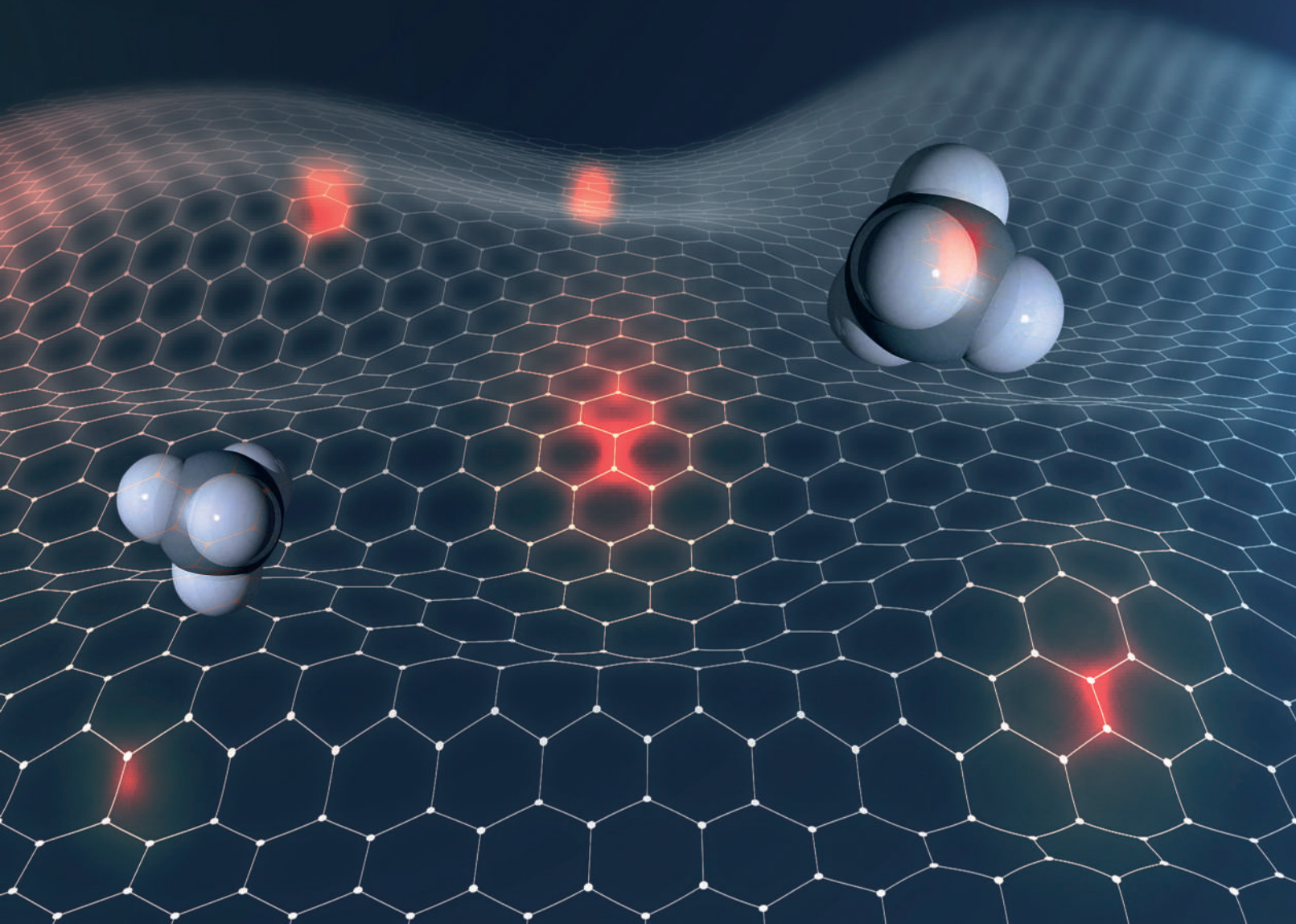


www.viserdata.com

RESEARCH AND APPLICATION OF **MATERIALS SCIENCE**

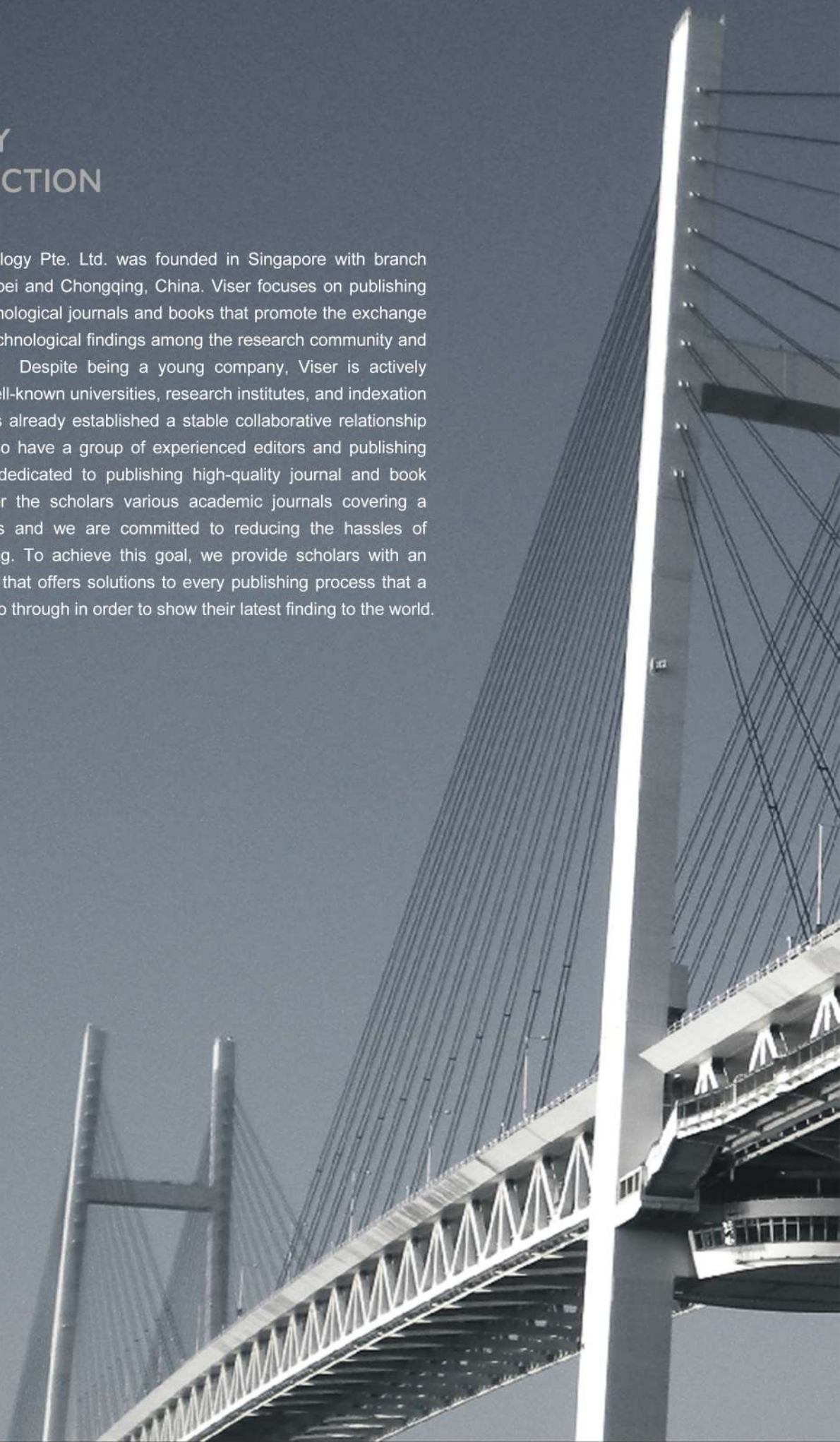
ISSN:2661-4464(online) 2661-4456(print)

Volume 1 No. 2 2019



COMPANY INTRODUCTION

Viser Technology Pte. Ltd. was founded in Singapore with branch offices in both Hebei and Chongqing, China. Viser focuses on publishing scientific and technological journals and books that promote the exchange of scientific and technological findings among the research community and around the globe. Despite being a young company, Viser is actively connecting with well-known universities, research institutes, and indexation database, and has already established a stable collaborative relationship with them. We also have a group of experienced editors and publishing experts who are dedicated to publishing high-quality journal and book contents. We offer the scholars various academic journals covering a variety of subjects and we are committed to reducing the hassles of scholarly publishing. To achieve this goal, we provide scholars with an all-in-one platform that offers solutions to every publishing process that a scholar needs to go through in order to show their latest finding to the world.



Research and Application of Materials Science

Editor-in-Chief: Zidong Wang

Associate Editors: Ting Zhu Mingliang Ge Jing Wang

Editorial Board Members:

Zhiqiang Cao	Jingxin Hao	Wanwu Ding	Jianqiang Zhang	Yuejin Qian
Zijian Song	Xiaofeng Fan	Wen Lei	Xinglong Dong	Enshan Han
Youwei Liao	Haizhu Sun	Fangchang Cai	Jianjian Zhang	Shaohua Luo
Feng Gao	Chunlin Song	Haiqiao Wang	Lili Zhao	Jiangmiao Yu
Qiang Luo	Linhui Zhang	Zuci Quan	Lingmin Yu	Zhinan Yang
Yong Han	Ziming Yang	Daming Zhuang	Bin Xiang	Xiaoni Zhang
Ying Liu	Zhaoxia Hou	Guobao Li	Shuanglong Feng	Suyun Tian
Xinli Guo	Chengchang Jia	Jinwu Kang	Wenbo Bu	Wanming Lin
Xiaohong Zhan	Jian Gu	Guoxuan Xiong	Weiwei Wang	Bo Wu
Xiaoliang Zhang	Lei Guo	Dongmian Zang	Ziliang Chen	Hui Li
Bo Jiang	Cong Zhang	Fugen Sun	Yongjun Feng	Zhanyong Zhao
Yi Zhong	Xizhang Wang	Jinghuai Zhang	Xiaoxu Liu	Wenli Gao



Publisher: Viser Technology Pte. Ltd.

ISSN: 2661-4464(online)

2661-4456(print)

Frequency:Semi-annual

Add.:21 Woodlands Close, #08-18,

Primz Bizhub SINGAPORE (737854)

https://www.viserdata.com/

Editors:

Yajun Lian

Yanli Liu

John Wilson

Nike Yough

Mart Chen

Qiuyue Su

Debra Hamilton

Xin Di

Jennifer M Dohy

Xiuli Li

Edward Adam Davis

Liangjun Qiu

Designer: Anson Chee

Research and Application of Materials Science

Volume 1 No.2 (2019)

CONTENTS

Experimental Investigation on Vibration Reduction Performance of Fiber Metal Laminate Beams with MRE Core	1
Jintong HAN, Wenyu WANG, Xintong WANG, Xiaoyue HU, Ziheng WANG, Zhijiang GAO, Hui LI	
Tribological property study of xanthate acetic ester in hydrogenated oil	5
Juanhong LEI, Jian LIU, Liping XIONG, Xue YANG, Zhongyi HE	
Recent Progress on Catalysts towards Electrocatalytic Nitrogen Reduction Reaction.....	10
Xue YAO , Rui ZHAO , Zhengtong JI , Xingyou LANG , Yongfu ZHU, Qing JIANG	
Kansei Engineering Analysis of Purple-clay Teapot Based on Online Comment Data.....	21
Xinyu ZHANG , Bin QI , Yanpu YANG, Xiaoming SUN	
Biomass Straw Based Activated Porous Carbon Materials for High-Performance Supercapacitors	27
Mengdie GUAN, Xinle ZHANG, Yingping WU, Qihao SUN, Dongqi DONG, Xiaoling ZHANG, Jie WANG	
Effect of Heat Treatment on Microstructure and Mechanical properties of high strength low alloy (HSLA) steel	31
Siyuan ZHAO , Kaixuan CHEN, Yalikus•WUQIKUN, Xiaohua CHEN, Zidong WANG	
Adsorption of U(VI) onto Amidoxime-functionalized Hydrothermal Carbon in the Presence of Ca-U(VI)-CO₃ Complexes.....	39
Yinghui XIE, Zhimmin DONG, Haoyan ZHANG, Runze ZHOU, Yunhai LIU, Zhibin ZHANG	
Preparation of cobalt ferrite nanoparticles using fulvic acid as a capping agent and its effect on catalytic activity	48
Jinxing LI, Abdelrahman A. Badawy, Guanben DU, Xiaojian ZHOU, Hisham A. Essawy	

Experimental Investigation on Vibration Reduction Performance of Fiber Metal Laminate Beams with MRE Core

Jintong HAN¹, Wenyu WANG^{1,2}, Xintong WANG², Xiaoyue HU², Ziheng WANG², Zhijiang GAO², Hui LI^{2*}

1 Northeast Yucai Foreign Language School, Shenyang, Liaoning, China, 110819;

2 School of Mechanical Engineering & Automation, Northeastern University, Shenyang, Liaoning, China, 110819

*Corresponding Author: Hui Li; Wenhua Road No. 11, Northeastern University, Shenyang, Liaoning, 110819, China; lh200300206@163.com

Abstract:

The vibration reduction characteristics of composite beams filled with magnetorheological elastomer core are studied experimentally. The fiber metal laminates with magnetorheological elastomers core is self-designed and prepared. Internal magnetic field is applied to the beam to explore its action of damping vibration performance under the magnetic field for the first time. The composite elements test system with controllable magnetic field intensity is designed and the function of each part is introduced. Then, a set of reasonable and standard vibration test flow of this type of composite beam under different magnetic field intensity is clarified, and the practical test is conducted. It has been found that the composite beam has excellent damping performance with the first 4 damping ratios being greater than 10%. Moreover, after the magnetic field is applied, its damping results can be further improved to meet the active control purpose.

Keywords: magnetorheological elastomer; fiber metal hybrid composite beam; magnetic field intensity; vibration characteristics; damping ratio

1. Introduction

Fiber metal laminate (FML) is a new type of non-homogeneous composite materials that combine the superior ductility and corrosion resistance of metal materials, and the advantage of lightweight and high strength of fiber-reinforced composite materials [1-3]. Nowadays, there are an increasing number of FML plates being used in the fuselage skin, vertical and horizontal tail leading edge, rectifying plate, fairing, upper fuselage siding and the upper slab of the military and civil aircraft [4-5]. Damping is an important indicator of the dynamic properties of this type of materials and structures, which is very critical to anti-vibration, shock resistance and noise control [6-8]. Magnetorheological Elastomer (MRE) is an upgraded version of the magnetically controlled fluid magnetorheological fluid (MRF) material, which overcomes the shortcomings of easy settlement and poor stability of MRF [9-11]. If the adjustable damping properties of the MRE can be effectively utilized, the vibration resistance, stability and fatigue durability of the whole laminate structure can be greatly improved.

At present, some researchers have carried out lots of researches on the vibration control problems of metal,

composite beam, plate and shell structures with MRE core. Choi et al. [12] studied the vibration response to metal beams filled with an MRE core, and found that with the increase in thickness of the MRE core, the structural damping performance tends to rise. Dwivedy et al. [13] used the finite element method to analyze the vibration and stability of metal beam structures with an MRE core under various boundary conditions, and verified the performance advantages of this type of structure in the active vibration control. Ni et al. [14] studied the vibration response of a metal sandwich beam filled with an MRE core under random excitation, and found that the change of the external magnetic field has an important influence on the shear modulus of the structure. Deng et al. [15] developed an adaptive tuning vibration absorber (ATVA) based on MRE. Through test comparison, it was found that ATVA was superior to the traditional passive damper in terms of vibration absorption capacity. Wei et al. [16] studied the vibration control of a metal sandwich beam filled with an MRE core, and found that in different excitation frequency ranges, the control effect of the applied magnetic field was quite different. Usually, the closer to the natural frequency, the better it will be for the vibration control effect of such

beam structure. Hu et al.^[17] studied the suppression effect of the vibration response to metal sandwich beams filled with MRE and MRF materials. It was found that their natural frequencies decreased with the increase in the applied magnetic field intensity, and the MRE has better vibration damping performance than that of the MRF.

The literature survey of the work presented here proves to be limited research work on MRE material applied in the field of active vibration control of FML composite materials, especially with the lack of systematic analysis and solution of structural damping characteristics. Therefore, from the perspective of integrated design of structure and function, the fiber metal laminates with an MRE core (MRE-FML) are developed in this paper. Further, by taking the beam structure with MRE core as an example, its vibration reduction performances under different magnetic field intensities are investigated and evaluated based on the experimental results.

2. Preparation of the MRE-FML beam

The studied MRE-FML beam is composed of two metal layers, two fiber-reinforced layers and an MRE core, whose structural schematic is shown in Fig. 1.

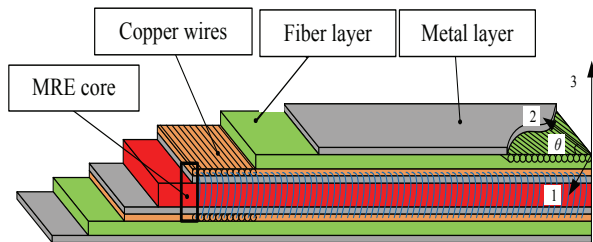


Figure 1. Theoretical model of MRE-FML composite beam

Silicone rubber and silicone oil were used as the matrix materials, and carbonyl iron powders were used as the ferromagnetic particles of the MRE. The mass ratio between carbonyl iron powders, silicone rubber and silicone oil is 7:1.5:1.5. During the preparation process, firstly, weigh a certain amount of carbonyl iron powders in a beaker using an electronic scale. After adding the corresponding proportion of silicone oil and rubber materials, stir the mixture with a glass rod until it is even, and then let it stand for 30 minutes to remove bubbles (the time should not be too long to avoid solidification). Next, an aluminum alloy beam was placed in a specific mold, and the viscous mixture of the uncured MRE was evenly spread on the surface of aluminum alloy beam. Subsequently, another aluminum alloy beam is symmetrically covered on the uncured MRE. Then, this laminated structure was repeatedly rolled using a press roll and molded at room temperature for 24 hours. Afterwards, the copper coils were wound on the both surface to the sandwich structure to finish the fabrication of the MRE core. Noted that it already includes the two layers of coils, two layers of aluminum alloy and one layer of MRE material. The detailed material composition of MRE core is listed in Table 1.

Table 1. MRE core material composition

Order	Type	mass/g	thickness/mm
1	aluminum alloy(each layer)	6	0.3
2	copper coil	3	0.3
3	carbonyl iron powder	28	
4	silicone oil	6	2
5	silicone rubber	6	

After the MRE core materials were fabricated, the unidirectional carbon-fiber fabrics and epoxy resins were laid to form the fiber-reinforced layers (whose laying information is $[(0^\circ/90^\circ)_3]$) on their upper and lower sides, and the two layers of aluminum alloy were laid on the outside of the used fiber layers. Finally, press this laminated structure tightly with a tempered glass plate to remove bubbles (which needs to be done by repeated rolling with a foam roller). When the whole structure was fully cured, its edge burrs need to be removed by a table saw to obtain the standard MRE-FML beam specimen. Only in this way, the prepared MRE-FML beam can meet the test requirements in the experiment.

3. Vibration reduction performance test of the MRE-FML beam specimen

3.1. Test objects and system

In this paper, the MRE-FML beam prepared in Section 1 is considered as the research object. Firstly, a clamping fixture, as shown in Fig. 2, is used to clamp one of the short edge. The length, width and thickness of the beam under restraint are $200 \times 30 \times 5$ mm (the clamping length is 40 mm).

Fig. 2 shows the developed vibration test system of the MRE-FML beam considering the internal magnetic field effect. By adjusting this internal magnetic field intensity, the damping performance of MRE-FML beam can be quantitatively controlled. The vibration test system mainly includes: (1) PCB086C01 modal force hammer; (2) BK4517 lightweight accelerometer; (3) LMS SCADAS 16-channel data acquisition; (4) DELL M4800 laptop workstation; (5). 24V DC power supply and 2Ω resistance.

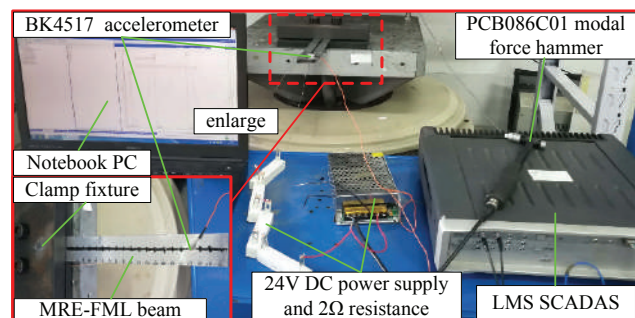


Figure 2 Vibration test system of MRE-FML beam under magnetic field

3.2. Test procedure the MRE-FML beam

The detailed test procedures are summarized as follows:

(1) Connect the experimental circuit to ensure the test reliability of all connected parts

Firstly, connect the copper wires in the MRE-FML beam to the circuit, and turn on the circuit switch to adjust the resistance to an appropriate value. Noted that this step is necessary before the formal experiment, which can ensure the test stability and reliability of all connected sensors and instruments.

(2) Test the natural frequency and damping characteristics of the MRE-FML beam without the magnetic field

Employ the PCB086C01 modal force hammer and BK4517 lightweight accelerometer to conduct the modal experiment on the MRE-FML beam without the magnetic field, where the excitation and response signals are acquired in real time by the LMS SCADAS 16-channel data acquisition. Then, based on the experimental frequency response function data, the first 4 natural frequencies and modal damping ratios can be obtained by PolyMAX method in LMS Test.Lab 14A software.

(3) Test the natural frequency and the damping performance of MRE-FML beam after the magnetic field is applied

After the current in the copper wires of MRE-FML

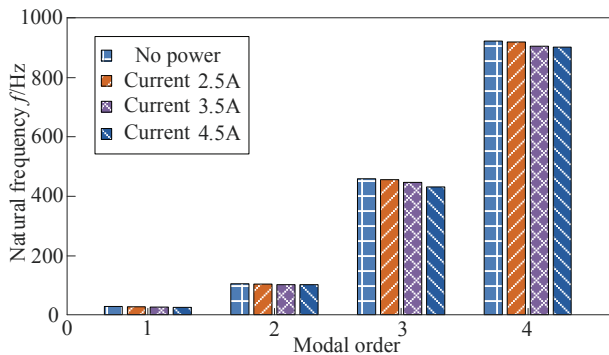


Figure 3. The first four natural frequencies under different magnetic field conditions

Analysis of the above results shows that:

(1) After the magnetic field is applied, the natural frequencies of all orders of the MRE-FML beam show a trend of decrease. The natural frequencies of the third and fourth orders decrease by 2% to 5%, while the natural frequencies of the first and second orders do not change significantly. This may be because the magnetorheological effect is relatively small under low magnetic field intensity, which makes the change of low order natural frequency of laminated beams not obvious.

(2) The MRE-FML beam has excellent passive damping performance with the first 4 damping ratios being greater than 10%, which is significantly greater than the general damping behavior of composite structure, such as fiber reinforced or fiber-metal laminates (which is usually 1-3%). Moreover, after the magnetic field is applied, its

beam is kept on 1 minute (to let the deformation of MRE core reach a stable state), the modal experiment on the MRE-FML beam with the magnetic field (this time with the current of 2.5A) is carried out again. Then, the first 4 natural frequencies and modal damping ratios can be obtained by using the same test techniques.

(4) Test the natural frequency and damping performance of MRE-FML beam under different magnetic field conditions

Set other two different currents in the copper wires of MRE-FML beam, such as 3.5A and 4.5A, and measure the first 4 natural frequencies and modal damping ratios with the same excitation position and the response position used in the step(3). Then, the effect of vibration reduction can be compared and evaluated under different magnetic field conditions.

4. Experimental investigation of vibration reduction performance of MRE-FML beam

Here, the influence of different magnetic field conditions on the natural frequencies and damping behavior of the MRE-FML beam is investigated, which is based on a series of experimental results (whose test procedure has already been described in Section 3.2). Fig. 3 and Fig. 4 show the first 4 natural frequencies and modal damping ratios.

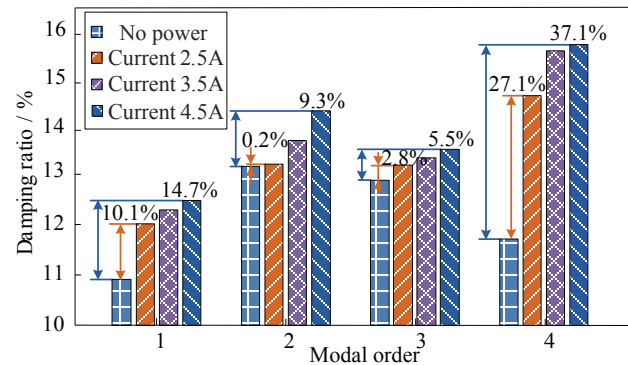


Figure 4. The first four damping ratios under different magnetic field conditions

damping results can be further improved. For example, the increased degree of first four damping ratios reach to 14.7, 9.3, 5.5 and 37.1%, respectively when the current is raised to 4.5A. This proves the feasibility that continuously increasing magnetic field intensity (which is proportional to current) can facilitate the improvement of active damping performance. This increased active damping performance is due to the raised loss factor of MRE materials when the applied magnetic field intensity is increased. Also, this means that the damping performance of the MRE-FML beam can be accurately controlled, which can facilitate to achieve the goal of the quantified control of structural vibration response. However, it should be noted that since the external magnetic field is generated by the current which will lead to an increase in the temperature of the winding copper coil, in the following studies, it is necessary

to quantitatively evaluate the influence of temperature variation on the damping performance.

5. Conclusion

In this paper, by taking the beam structure as an example, MRE-FML structural functional integration materials are prepared, and relevant test system is established to study its damping and vibration reduction performance. It has been found that:

(1) MRE-FML has excellent damping performance, which can be further improved after the magnetic field is applied. Especially, the fourth order damping was increased by 35%.

(2) The damping performance of the MRE-FML beam can be precisely controlled by changing the magnetic field intensity.

Therefore, the vibration response can be precisely controlled. In the future research, it is necessary to carry out more theoretical and experimental studies, especially in active vibration control strategies and methods.

Acknowledgements: This study was supported by the National Natural Science Foundation of China (granted No. 51505070), the Fundamental Research Funds for the Central Universities of China (granted No. N160313002, N160312001, N170302001, N180302004, N180703018, N180312012 and N180313006), the National Key Laboratory of Science and Technology on Advanced Composites in Special Environments, Harbin Institute of Technology (granted No. 6142905192512).

References

- [1] Marsh G. Airframers exploit composites in battle for supremacy[J]. Reinforced Plastics, 2005, 49(3):26-32.
- [2] Xue P C, Li H, Chang Y L, et al. Natural frequency calculation and validation of fiber reinforced composite thin plate under cantilever boundary[J]. Journal of Aerospace Power, 2016, 31(7):1754-1760.
- [3] Xu Z, Li H, Xue P C, et al. Natural Characteristics Analysis and Validation of Fiber Metal Laminates Thin Plates Under Cantilever Boundary[J]. Journal of Northeastern University (natural science), 2018, 39(12):1737-1742.
- [4] Tao J, Li H G, Pan L, et al. Research and development trend of fiber metal laminates[J]. Journal of Nanjing University of Aeronautics & Astronautics, 2015, 47(5):626-636.
- [5] Cao Z Q. Fiber metal laminates and their applications in aircraft structures[J]. Aeronautical Manufacturing Technology, 2006(6):60-62.
- [6] Ren Y S, Liu L H. Research progress on structural damping of fiber reinforced composites[J]. Mechanics in Engineering, 2004, 26(1):9-16.
- [7] Li H, Sun W, Chang Y L, et al. Time domain test method for nonlinear damping of a fiber-reinforced composite thin plate with amplitude dependence[J]. Journal of Vibration and Shock, 2018, 37(5):169-174.
- [8] Li H, Niu Y, Liang X L, et al. Time-domain test method for nonlinear damping of fiber reinforced composite thin plate based on nonlinear squeezing transform[J]. Journal of Aerospace Power, 2018, 33(6):1456-1463.
- [9] Modesto T. López-López, Kuzhir P , Bossis G , et al. Preparation of well-dispersed magnetorheological fluids and effect of dispersion on their magnetorheological properties[J]. Rheologica Acta, 2008, 47(7):787-796.
- [10] Xiong C, Lv J G, Zhang J Q, et al. Research on the characteristics, mechanism and application of magneto-rheological intelligent materials[C]// National Conference on Composite Materials. 2002.
- [11] Wang J X, Meng G. Research advances in magnetorheological elastomers[J]. Journal of Functional Materials, 2006, 37(5):706-709.
- [12] Choi W J, Xiong Y P, Sheno R A. Vibration Characteristics of Sandwich Beams with Steel Skins and Magnetorheological Elastomer Cores[J]. Advances in Structural Engineering, 2010, 26(13):837-844.
- [13] Dwivedy S K, Mahendra N, Sahu K C. Parametric instability regions of a soft and magnetorheological elastomer cored sandwich beam[J]. Journal of Sound & Vibration, 2009, 325(4-5):686-704.
- [14] Ni Y Q, Ying Z G, Chen Z H. Magneto-rheological elastomer (MRE) based composite structures for micro-vibration control[J]. Earthquake Engineering and Engineering Vibration, 2010, 9(3):345-356.
- [15] Deng H X, Gong X L, Wang L H. Development of an adaptive tuned vibration absorber with magnetorheological elastomer[J]. Smart Materials and Structures, 2006, 15(5):N111-N116.
- [16] Wei K X, Meng G, You H, et al. Experimental study on vibration response characteristics of a magnetorheological elastomer sandwich beam[J]. Journal of Vibration and Shock, 2009, 28(10):81-83.
- [17] Hu G L, Li B B, Jiang M, et al. Analysis of Vibration Control Performance of Magnetorheological Sandwich Beam Based on MRF and MRE Materials[J]. Machine Tool & Hydraulics, 2018, 46(11):101-105.

Tribological property study of xanthate acetic ester in hydrogenated oil

Juanhong LEI, Jian LIU, Liping XIONG, Xue YANG, Zhongyi HE*

School of Material Science and Engineering, Eastchina Jiaotong University, Nanchang City, China

*Corresponding Author: Zhongyi HE, Corresponding address, Nanchang City 330013, China; email address:hzy220567@163.com

Abstract:

Xanthate was used as an initial reactant to synthesis two kinds of novel xanthate-containing acetic ester additives (HX and OX), and a four-ball machine was used as tribological tester to appraise their tribological behaviors in hydrogenated oil (10cst). The test results indicated that the as-synthesized additives possess good extreme pressure, antiwear and antifricition properties. The shorter carbon chains acetic ester, the better tribological properties the higher sulfur content. The action mechanism was estimated by analysis of the XPS (X-ray photoelectron spectroscopy) and SEM (scanning electron microscope) results of the worn steel ball surface, and the results illustrated that the protective film containing ferric sulfide and ferric sulfate compound was formed on the worn steel ball surface by xanthate acetic ester, and the protective film has good tribological properties.

Keywords: acetic ester derivative; additive; hydrogenated oil; tribological mechanism

1. Introduction

The modern industry needs better processing conditions, so it needs better lubricants in some processing fields. Many additives^[1] play a vital role in lubricating oil, because of its good guarantee in support of lubrication capability and satisfy the specific requirement. In many studies, it was reported that sulphur-containing^[2] compounds, such as sulfurized isobutylene, dibenzyl disulfide, etc, have the capability to improve lubricating oil extreme pressure performance. Sulfuration alkene is an excellent lubricant for offering effective protect to avoid mechanical fatigue, sintering and wear, so it is used in mechanical engineering oil, such as gear oil. Xanthate additive is a compound containing sulfur element, some research show that the binding energy of carbon-sulfur in xanthate is higher than that of sulfurized isobutylene, which makes the reaction activity of xanthate lower, therefore the xanthate is more stability in higher temperature condition and possesses lower corrosivity. The tribological properties of the target compound can be improved by adding xanthate groups to it. Some xanthate-containing triazine derivatives have been reported that they have outstanding tribological performance^[3].

Two xanthate-containing ester target products were synthesized by using xanthate and chloroethyl chloroacetate as raw materials, the main purpose is to make the additive

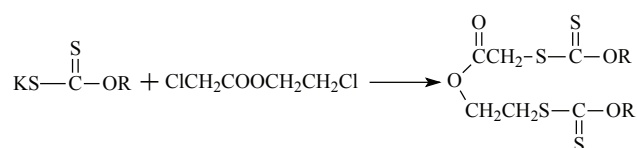
molecules have more xanthate functional groups. Their tribological behaviors of as-synthesis derivatives were appraised with a four-ball tribotester. The SEM and XPS analysis results were used to discuss their tribological mechanism in hydrogenated oil(10cst).

2. Experimental details

2.1 Base stock and additive

The base stock used is the hydrotreating oil produced in Daqing Refinery Factory, China. The hydrotreating oil (10cst) was without any pretreated before use, and its $v_{40\text{C}}$ is $51.71 \text{ mm}^2 \cdot \text{s}^{-1}$, the flashpoint is $247 \text{ }^\circ\text{C}$, viscosity coefficient is 126.

The two xanthate acetic esters were synthesized according to the way in Scheme 1.



Where R= $\text{C}_{16}\text{H}_{33}$ (HX); C_8H_{17} (OX)

Scheme 1. Reaction pathway of additives

The elemental analysis results of HX are as follow: C is 63.88(63.33), H is 10.09(10.00), S is 17.19(17.78). And

the elemental analysis results of OX are as follow: C is 53.56(53.23), H is 8.11(8.06), S is 24.99(25.81), the values in brackets are the theoretical analysis values. The test values of additives are basically the same as the theoretical values, the difference is within the experimental error range. Connecting with IR analysis results, it can be able to determine its structure.

2.2 Testing apparatus and worn surface analysis

Their tribological properties were evaluated with a four-ball tester, which according to the tribological testing standards (GB3142-82), similar to ASTM D-2783^[4]. The testing conditions are as below: rotating speed is 1450 rpm, the test lasted 30 min and room temperature. The used ball material is GCr15 bearing steel (AISI52100), and the hardness of the ball is 59–61 HRC. The average of wear scar diameters of three lower steel balls (code as WSD) was determined by an optical microscope, and its accuracy is ± 0.01 mm. The friction coefficient is calculated according to the data recorded automatically of the four-ball tribotester.

After the test, ultrasonic cleaning of the upper steel ball was performed with petroleum ether^[4] for XPS analysis (PHI-5702 X-ray photoelectron spectrometer, USA), with the additive concentration of 1.0 wt.% under 392 N for 30 min. Using the MgK α radiation as the excitation source, the binding energies of the target elements were determined at pass energy of 29.35eV and a resolution of 0.3eV, using the binding energy of C1s (284.6eV) as the reference. The worn morphology analysis^[5] of the lower steel ball was performed by a JEM-1200EX type scanning electron microscope (SEM), to observe the wear mark on the rubbed surface.

3. Results and discussion

3.1. The P_B value

The maximum non-seizure load (P_B value) of different content additives/10Cst is shown in Table1.

Table1 The P_B value of oil samples in different additives contents

Additives	P_B value (N)			
	0.0%	0.5 %	1.0%	1.5 %
HX	593.6	628.4	646.8	706.1
OX	593.6	632.8	739.5	788.3

From Table 1, the P_B values of HX and OX at any content are much higher than the P_B values of 10cst, and the P_B value increases when the additive concentration increase from 0.5wt% to 1.5wt%. The P_B values of OX at any content are higher than that of HX, for the higher sulfur content than HX at the same condition. When the HX and OX concentration was 1.5%, it can improve the P_B values of 10cst by 18.9% and 32.8% respectively, and this indicated that HX and OX have the excellent capacity in improving the load-carrying of base stock. The P_B value is associated with sulfur content, the higher sulfur concentration, the better load-carrying performance of 10cst.

3.2 Friction-reducing Performance

The friction coefficient curve of HX and OX in different contents under 392N, at 1.0wt% content in different loads, were shown in Figure 1.

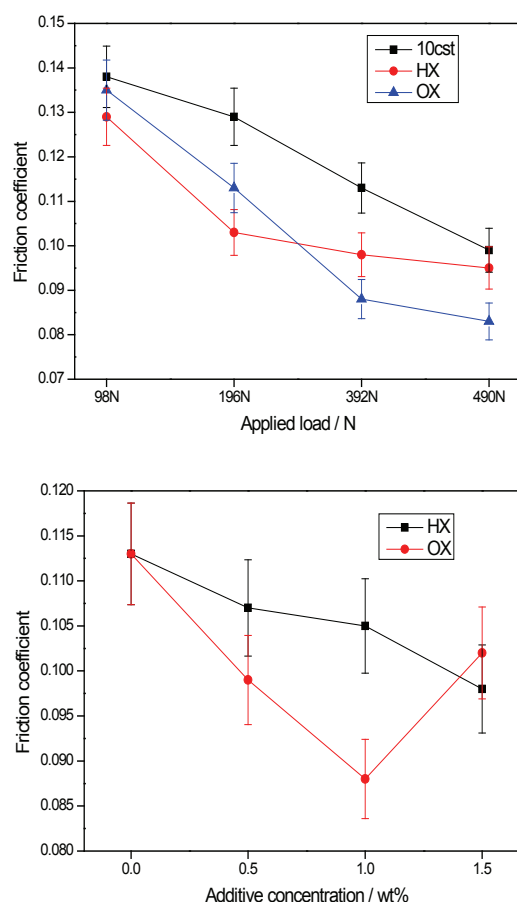


Figure 1 Friction coefficient of oil samples various applied load, additives concentration

From Figure 1(left), all the friction coefficient values of a lubricating stock decreased when the applied load increasing, meaning that the HX and OX possess good antifriction behavior under a wide load range. As shown in Figure 1(right), the applied load was 392N, the friction coefficient of 10cst was 0.114. When 1.0wt% HX was added in 10cst, the friction coefficient was 0.098, declining by 13.3%, and reduced 22.1% to 0.088 by adding 1.0wt% HX in 10cst. And the antifriction performances of OX-containing oil samples are better than the HX-containing oil samples at the same additive content. With the higher amount of OX, the friction coefficient values of oil samples increased. The decrease of friction coefficient of oil samples can be attributed to the strength of the formed adsorption and/or tribochemistry reaction film caused by the HX (OX) on the lubricating interface^[4]. When more HX (OX) was added to 10cst, there were more additives molecules adsorbed on the metal surface, which can form thicker adsorption layer. More tribochemistry products are generated in the metal surfaces to form a tribochemistry film, and the tribochemistry film also can prevent the asperities from direct contact,

which made the friction coefficients smaller. When the content additives arrived to some degree, the physical and chemical adsorption and tribochemical reaction process showed saturate tendency finally. It will cause corrosion worn when additive content over the better-adding concentration, then the friction coefficient will increase.

3.3 Antiwear performance

Figure 2 shows the relationship of WSD with additives concentrations at 392 N, and applied load with 1.0% the concentration of additives in 10cst.

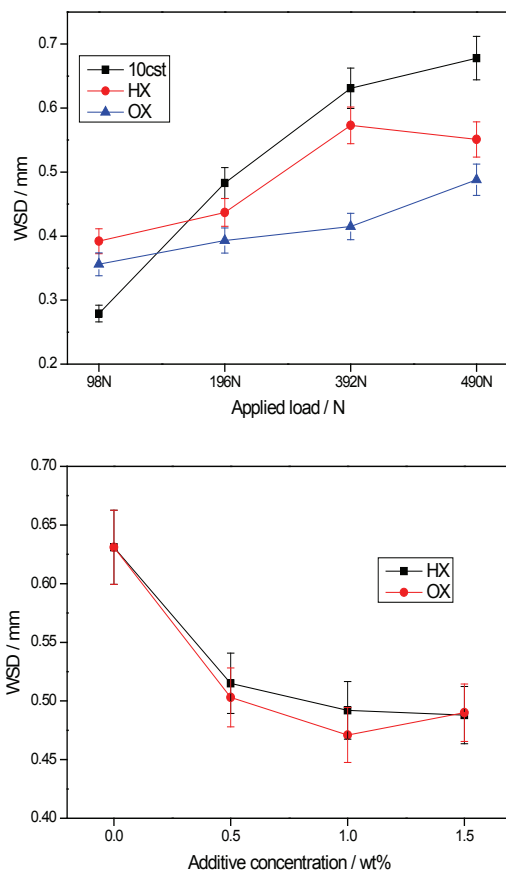


Figure 2 Variations in the WSD with concentration and applied load (N)

All HX and OX exhibit good antiwear properties in all applied loads. The WSD values increase as the applied load increasing from 98N to 490N. The increase of WSD of base oil is the largest. The WSD value of OX and 10cst are both smaller than that of HX at the same content and applied load.

The xanthate-containing ester additive reduces the WSD of 10cst significantly, meaning that they have very good antiwear property. As the additive concentration increased, the WSD value decreased. The sulfur content increased when added more HX/OX additives in 10cst, and the antiwear capability was increased as well. It may be the result of the boundary protective film formed by HX/OX and/ or their decomposition products on the lubricating surface through tribochemistry reaction during

the tribological process.

3.4 Discussion of the lubricating mechanism of HX/OX

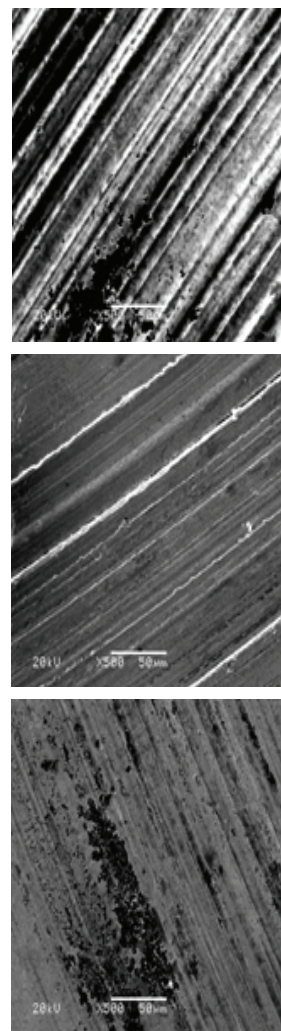


Figure 3 SEM of worn steel ball surface lubricated with 10Cst(left) and 1.0wt% HX (middle); OX(right) at 392N, 30min

The SEM photographs are shown in Figure 3. When there are only lubricated with 10cst, severe scuffing occurs on the worn steel ball surface, with the grain abrasion characteristic^[6]. There have only friction tracks to a small extent on the steel ball surface as lubricated with HX and OX, and there existed some black cavities on the surface, which may be due to the corrosive worn made by sulfur element. It is because that there exist tribochemical reactions between steel ball surface and sulfur element in HX/OX, to generate tribochemisorption^[3] during the lubricating process. The corrosive degree of steel ball lubricated by OX is bigger than that of HX, for the higher sulfur contents of OX. From the above analysis, it can be seen that the tribological performances of HX and OX are decided heavily by the ability of formed boundary protective film through adsorption (physisorption, chemisorption) and tribochemical reaction in the lubricating process.

In order to further explore the tribological mechanism

of these kinds of xanthate acetic ester in 10cst, XPS analysis was used to analyze the worn steel ball surface lubricated by 1.0wt% HX in 10cst, and the analysis results of characteristic elements are shown in Figure 4.

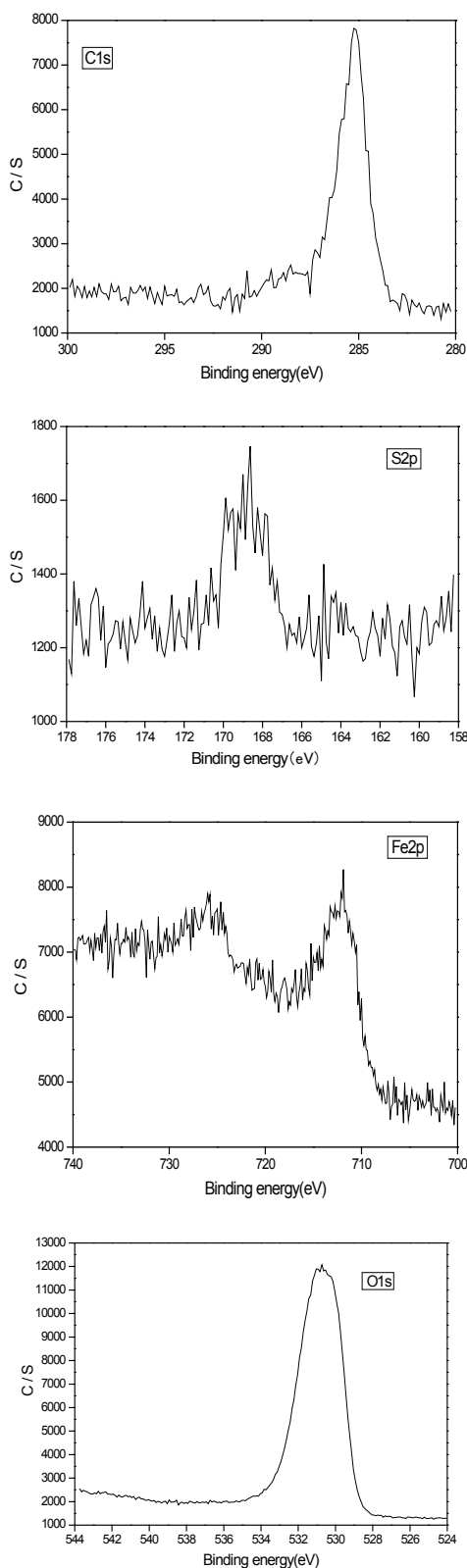


Figure 4 The XPS spectra of C_{1s} , S_{2p} , Fe_{2p} , O_{1s} (1.0wt% HX/10cst)

The peak of S_{2p} spectrum^[8] was located at 168.8eV and 170.0eV, which belong to ferric sulfide and ferric sulfate respectively. The formation of ferric sulfide and ferric sulfate indicates the tribochemical reaction had taken between HX with the metal surface in the lubricating process. The Fe_{2p} peak located at 711.3 eV and 724.8eV, which attributed to iron oxide and/or sulfide^[9], indicating that there existed oxidize or sulfurize on the lubricated steel surface because of the friction heat. The O_{1s} peak located around 531.0 eV, belonging to iron oxide, and that means tribochemical reaction had occurred in the steel ball surface with HX during the lubricating process.

The SEM and XPS analysis results proved that the HX and OX may be decomposed to generate xanthate (or other sulphur-containing compounds)^[7], so a relatively stable boundary lubrication film has been formed on the steel ball surface. The stable protect film is a complex lubricating film, which consists of adsorption layer and triboreaction layer. The triboreaction producing come from the tribochemical reaction between actively sulfur elements in the xanthate group and the freshly metal surface to form $FeSO_4$, and / or FeS ^[10], and the surface film possessing extreme pressure and antiwear capability. The surface film can avoid the direct contact of steel ball and other steel balls, so it can reduce the metal stock abrasion. Because of the stable reaction and adsorption film, the novel xanthate-containing ester can effectively increase the tribological performances of 10cst.

4. Conclusions

From the above results, the following conclusions can be drawn:

(1) The synthesized ester derivatives as additives in 10cst base oil show excellent load-carrying performance at appropriate concentrations, and the P_B values of OX at any content are higher than that of HX, for the higher sulfur content.

(2) The friction-reducing and antiwear capacities of HX and OX are highly susceptible to additive concentration and applied load. And the antiwear and friction-reducing behaviors of OX are better than that of HX at the same condition, for the different sulfur content.

(3) From the analysis results of SEM and XPS, it can be seen that the HX and OX have the behaviors of friction-reducing and antiwear in steel-steel sliding system through adsorption (physisorption, chemisorption) and tribochemical reaction with the steel ball surface. The formed boundary protective lubricating film during lubricating process helps to improve antiwear and friction-reducing capability of oil samples.

Author Contributions: Juanhong LEI and Zhongyi HE designed experiments; Jian Liu and Xue YANG carried out experiments; Liping XIONG analyzed experimental results. Zhongyi HE wrote the manuscript. All authors read and approved the manuscript.

Acknowledgements: The work was support by the National Natural Science Foundation of China (21563012,

51962020); Jiangxi Science Foundation of China (20171BCD40009, 20181BAB203010); Jiangxi Provincial Education Department Foundation of China (GJJ180305).

References

- [1] Wang Rulin, Lube Tribochemistry, China Petrochemistry Press, 1994, (in Chinese).
- [2]. Igartua A, Fernández X, Areitioaurtena O, et al. Biolubricants and triboreactive materials for automotive applications[J]. Tribology International, 2009, 42(4):561-568.
- [3] Yinglei Wu, Zhongyi He, Xiangqiong Zeng, et al. Tribological and anticorrosion behaviour of novel xanthate-containing triazine derivatives in water-glycol[J]. Tribology International, 2017,110:113–124
- [4] Dan Qiao, Haizhong Wang, Dapeng Feng. Benzimidazolyl phosphates as anti-wear additives in poly(ethylene glycol) for steel/steel contacts[J]. Lubrication Science, 2014, 26(1):1–11.
- [5] Zhongyi He, Liping Xiong, Mingxue Shen, Sheng Han, Jianqiang Hu, Wenyuan Xu, Tribological and antioxidation properties study of two N-containing borate ester derivatives as additive in rapeseed oil[J]. PLoS ONE,2018,13(12): e0207267
- [6] Li Chaolong, Xiong Liping, Liu Hong, Xiong Liting, Wang Wei, Tribological Study of Xanthate- containing Acetic Ester as Additives in Hydrogenated Oil[J]. Applied Mechanics and Materials,236-237:123 - 127.
- [7] Xiong Liping, He Zhongyi, Han Sheng, et al. Tribological properties study of N-containing heterocyclic imidazoline derivatives as lubricant additives in water-glycol[J]. Tribology International, 2016, 104:98-108
- [8] Yongjian Gao, Zhijun zhang, Qunji Xue, Study on 1,3,4-thiadiazole derivatives as novel multifunctional oil additives. Materials Research Bulletin. 1999;34:1867-1874.
- [9] K.Komvopoulos, V.Chiaro, B.Pakter, et al, Antiwear tribofilm formation on steel surface lubricated with gear oil containing borate, phosphorus, and sulfur additives, Tribology Transactions. 2002;45(4):568-575.

Recent Progress on Catalysts towards Electrocatalytic Nitrogen Reduction Reaction

Xue YAO , Rui ZHAO , Zhengtong JI , Xingyou LANG , Yongfu ZHU*, Qing JIANG

Key Laboratory of Automobile Materials, Ministry of Education, School of Materials Science and Engineering, Jilin University, Changchun, China

*Corresponding Author: Yongfu ZHU, Key Laboratory of Automobile Materials, Ministry of Education, School of Materials Science and Engineering, Jilin University, Changchun, 130022, China; yfzhu@jlu.edu.cn

Abstract:

The energy-intensive Haber-Bosch process currently dominates the production of ammonia (NH_3), an indispensable chemical for humans. For the sustainable development of society, highly efficient and green strategies to convert nitrogen (N_2) to NH_3 are urgently required. Electrocatalytic N_2 reduction reaction (eNRR) is universally regarded as a promising strategy owing to the mild operating conditions and renewable energy supply. The key for eNRR is the high-performance catalysts, which activate the inert N-N triple bond and thus decrease the energy barrier. Herein, the recent theoretical and experimental progress on eNRR catalysts at room temperature and ambient pressure is summarized, aiming to provide a reference for future design of high-performance eNRR catalysts.

Keywords: electrocatalysis; nitrogen reduction reaction; elemental catalysts; compound catalysts; single-atom catalysts

1. Introduction

Growing human population, expanding industrialization, and potential foreground as hydrogen energy carrier everlastingly increase the requirement of ammonia (NH_3).^[1-5] In industry, currently, NH_3 synthesis largely depends on the Haber-Bosch process, where atmospheric nitrogen (N_2) is reduced to NH_3 using iron-based catalysts.^[6-8] However, such a reduction reaction is proceeded at high temperature and high pressure, and consequently it consumes tremendous amounts of fossil fuels and causes serious greenhouse gas emissions.^[9-12] In this regard, it is pressing to replace the Haber-Bosch process with highly efficient and fossil-free pathways.

Inspired by the biological N_2 fixation, which occurs in mild conditions on nitrogenase enzymes, where FeMo-cofactors are the catalytic active sites,^[13, 14] electrocatalytic N_2 reduction reaction (eNRR) is widely regarded as a promising pathway to synthesize NH_3 , where N_2 and H_2O are needed and the energy sources are renewable and clean.^[15-22] On the one hand, the N-N triple bond is strong with a bond energy of 941 kJ mol^{-1} , so the splitting of this bond is sluggish, resulting in the requirement of highly active catalysts.^[11] On the other hand, the active sites on catalyst surfaces towards

eNRR are usually also active for the reduction of H_2O to hydrogen (H_2), leading to a low Faradaic efficiency, where proton-electron pairs ($\text{H}^+ + \text{e}^-$) in the catalytic system are mainly consumed by the hydrogen evolution reaction (HER) rather than eNRR.^[23-26] Thus, sufficient eNRR catalysts should have high activity and excellent selectivity.

In the field of catalysts design, theoretical calculations provide the guidance while experimental explorations examine the guidance and give suggestions back.^[20, 27-31] Hence, theoretical and experimental studies are both important for optimal catalysts. With this in mind, in this review, we summarize the recent theoretical and experimental progress on eNRR catalysts, mainly focus on the maximum energy barrier and the selectivity, where the former is determined by the change of free energy for the potential determining step (PDS) in theoretical calculations and the latter is reflected by the Faradaic efficiency in experimental tests.

2. Reaction Mechanisms

In general, electrocatalytic reduction of N_2 to NH_3 can be divided into the dissociative mechanism, the associative mechanism, and the Mars-van Krevelen mechanism,

where the reduction is realized with hydrogenation induced by the proton–electron pairs ($H^+ + e^-$), as depicted in Figure 1. For the dissociative mechanism, the adsorbed N_2 molecule is split into two N atoms, i.e. $*N$ and $*N$, where $*$ is an adsorption site of the catalyst. Large energy input is usually required to catalyze eNRR through this mechanism owing to the strong N–N triple bond. The associative mechanism can be further classified into three mechanisms, i.e. the distal mechanism, the alternative mechanism, and the enzymatic mechanism, where six hydrogenation steps are involved for every mechanism. In detail, standing-on adsorbed N_2 molecule is reduced via the distal or alternative mechanism, while lying-on adsorbed one is reduced in the enzymatic mechanism. Moreover, for the distal mechanism, a NH_3 molecule is formed in the first three steps based on the distal N atom, and then the left N atom is further reduced into NH_3 in the last three steps. Different to the case of the distal mechanism, two N atoms of an adsorbed N_2 molecule are alternately hydrogenated in the alternating and enzymatic mechanisms. As regards the Mars-van Krevelen mechanism, which usually occurs on the surfaces of nitrides, a surface N atom is first reduced to NH_3 , causing a N-vacancy. A N_2 molecule will be adsorbed on such a vacancy, and the N atom out of the catalysts is hydrogenated to form the second NH_3 molecule.

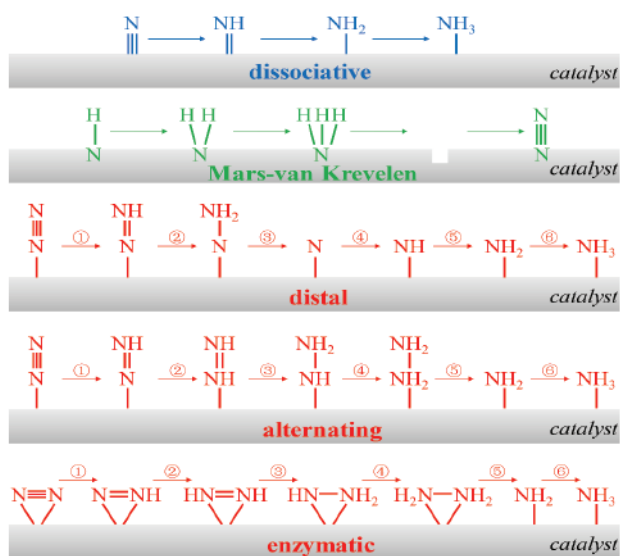


Figure 1. Scheme illustrations of possible eNRR mechanisms, including dissociative, Mars-van Krevelen, distal, alternating, and enzymatic mechanisms. For the Mars-van Krevelen mechanism, the rectangular blank denote a N vacancy. For distal, alternating, and enzymatic mechanisms, six elementary hydrogenation steps are labelled.

3. Elemental Catalysts

3.1. Transition metal

Due to the concept of “accept and backdonate”, where the unoccupied d orbitals accept electrons from adsorbed N_2 and the occupied d orbitals backdonate electrons

to adsorbed N_2 simultaneously, transition metal (TM) atoms usually have high eNRR activity. With the help of density functional theory (DFT) calculations, Skúlason et al. first explored the possibility of forming NH_3 via eNRR on close-packed and stepped TM surfaces,^[32] using the computational hydrogen electrode (CHE) model developed by Nørskov and coworkers.^[33] According to the theoretical calculations, Mo, Fe, Rh, and Ru are the most active TM surfaces (Figure 2). However, the major competing reaction, HER, will significantly decrease the Faradaic efficiency of eNRR on these TM surfaces. In contrast, the bonding of N_2 is more stronger than that of H adatom on early TM surfaces, such as Sc, Y, Ti, and Zr, suggesting that NH_3 should be the main product rather than H_2 on these TM surfaces. Moreover, in Skúlason’s work,^[32] the linear scaling relations were proposed, which shows that binding energy of all the N_2H_x and NH_x species can be expressed on the basis of the binding energy of N adatom. After this pioneering theoretical work, Montoya et al. further highlighted that the linear scaling relations between $*N_2H$ and $*NH_2$ can be used to predict the overpotential of the eNRR process.^[34]

According to above theoretical studies,^[32, 34] especially that Mo is one of the TM atoms on the top of the volcano diagrams, Yang et al. synthesized (110)-oriented Mo nanofilm to catalyze eNRR, and achieved a Faradaic efficiency of 0.72% at an overpotential of 0.14 V and a rate of NH_3 formation of $3.09 \times 10^{-11} \text{ mol s}^{-1} \text{ cm}^{-2}$ under an applied potential of -0.49 V vs reversible hydrogen electrode (RHE).^[35] To reveal the origin of excellent performance of oriented Mo nanofilm, electrochemical tests were done in four Mo-based samples, including commercial Mo foil, Mo-A-R, Mo-D-R-1h, and Mo-D-R-5h, where A is the electrochemical anodization, R is the reduction process, D is the electro-deposition, and 1h and 5h are the time of electro-deposition. Among these four samples, Mo-D-R-5h shows the best catalytic performance, as shown in Figure 3. This is because Mo-D-R-5h possesses the highest (110) orientation and lowest (211) orientation, where Mo(110) plane can bind N adatom more strongly than H adatom while HER is the predominant reaction on Mo(211) plane.

In usual, noble metals have excellent activity to various reactions. Bao et al. synthesized tetrahedral gold nanorods (THH Au NRs), which are enclosed by stepped facet and composed of (210) and (310) sub-facets, to endow the eNRR with a NH_3 yield of $1.648 \mu\text{g h}^{-1} \text{ cm}^{-2}$.^[8] According to DFT calculations, the PDS of Au(210) and Au(310) sub-facets are both the first hydrogenation of adsorbed N_2 . Similarly, taking Au as the raw materials, Nazemi et al. synthesized hollow gold nanocages (AuHNCs) to catalyze eNRR under ambient conditions,^[36] and it obtained a Faradaic efficiency of 30.2% at -0.4 V vs. RHE and a NH_3 yield of $3.9 \mu\text{g cm}^{-2} \text{ h}^{-1}$ at -0.5 V vs. RHE in 0.5 M $LiClO_4$ aqueous solution (Figure 4). Moreover, the eNRR rate was also evaluated using solid Au nanoparticles of various shape with similar nanoparticle concentrations, including rods (NRs), spheres (NSs), and

cubes (NCs).^[36] The NH_3 yield rate and Faradaic efficiency of solid Au nanoparticles were significantly lower than those of AuHNCs, where Au NRs are the worst among solid nanoparticles. This is because the number of coordination unsaturated surface atoms increases for nanoparticles with sharper edges, where coordination unsaturated surface atoms are active for adsorbing and reducing N_2 . The authors concluded that the cavity can entrap N_2 molecules, resulting in the high frequency collisions with the hollow Au cages and increasing residence time of N_2 molecules on the nanoparticle inner surface, and AuHNCs thus shows excellent eNRR performance.^[36] Besides Au, Ag also has proved its worth in eNRR. Huang et al. synthesized Ag nanosheet to act as high-performance eNRR catalysts at ambient conditions.^[37] Electrochemical tests showed that a Faradaic efficiency of 4.8% and a NH_3 yield rate of $4.62 \times 10^{-11} \text{ mol s}^{-1} \text{ cm}^{-2}$ at 0.60 V vs RHE were achieved on Ag nanosheet, and little changes in Faradaic efficiency and the NH_3 yield rate can be seen after several times of recycling tests on this catalyst.

3.2. Nonmetal

Recently, Légaré et al. presented that N_2 binding and reduction can be realized by a non-metal element, boron,

because the empty sp^2 and occupied p orbitals of boron atom can accept electrons from and backdonate electrons to N_2 ,^[38] similar to the cases of TM atoms. Based on this observation, Liu et al. proposed that inorganic boron monolayer can catalyze eNRR with the help of DFT calculations.^[39] Two types of boron monolayer were considered, α -sheet and β_{12} -sheet, and the maximum free energies of eNRR were 0.77 eV and 1.22 eV for them, respectively. Moreover, the authors found that the catalytic performance will be improved if two boron-sheets are deposited on Ag and Cu surfaces. In experiments, Zhang et al. synthesized boron nanosheet (BNS) to catalyze eNRR. The corresponding DFT calculations suggested that the boron atoms of both oxidized and H-deactivated BNS can catalyze eNRR more effectively than the clean BNS.^[40]

In addition, encouraged by the principle of “like dissolves like”, Zhang et al. synthesized well-exfoliated few-layer black phosphorous nanosheets as metal-free eNRR catalysts. Such catalysts were efficient for eNRR, and a high NH_3 yield of $31.37 \mu\text{g h}^{-1} \text{ mg}_{\text{cat}}^{-1}$ under ambient conditions can be attained.^[41] DFT calculations revealed that the selective reduction of N_2 to NH_3 occurs on the zigzag and diff-zigzag edges with the alternating mechanism due to the active orbitals and electrons.

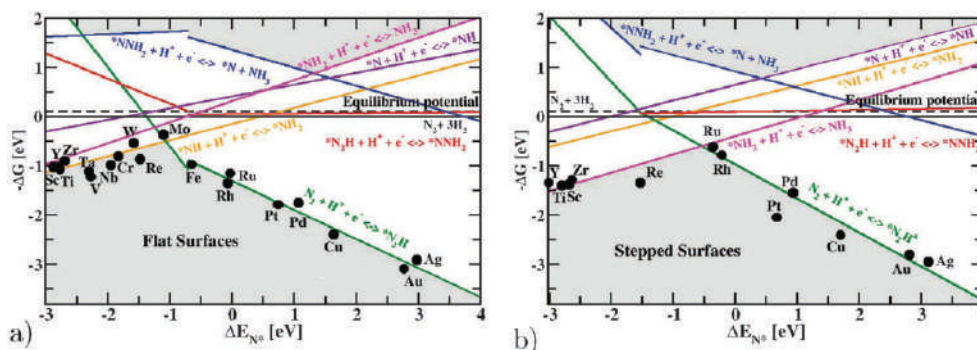


Figure 2. Negative of the change of the free energy ($-\Delta G$) is proportional to the onset potential, for all the charge transfer steps of ammonia synthesis as a function of the nitrogen binding energy at $U = 0$ V for (a) flat surfaces and (b) stepped surfaces via the Heyrovsky-type associative mechanism. Reproduced from Ref.[32] with permission from the PCCP Owner Societies.

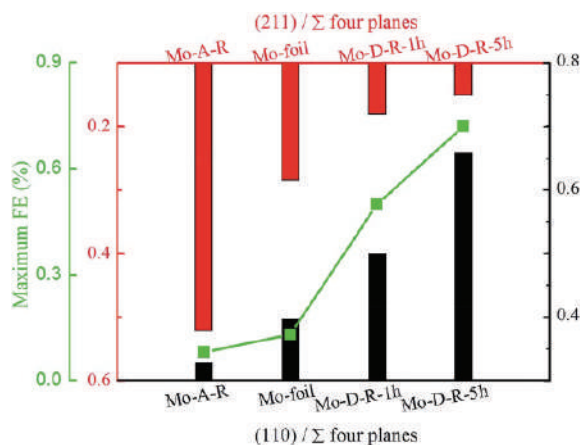


Figure 3. The relationship among the (110) orientation, (211) orientation and maximum Faradaic efficiency of four Mo-based electrochemical catalysts. Reproduced from Ref. [35] with permission from The Royal Society of Chemistry.

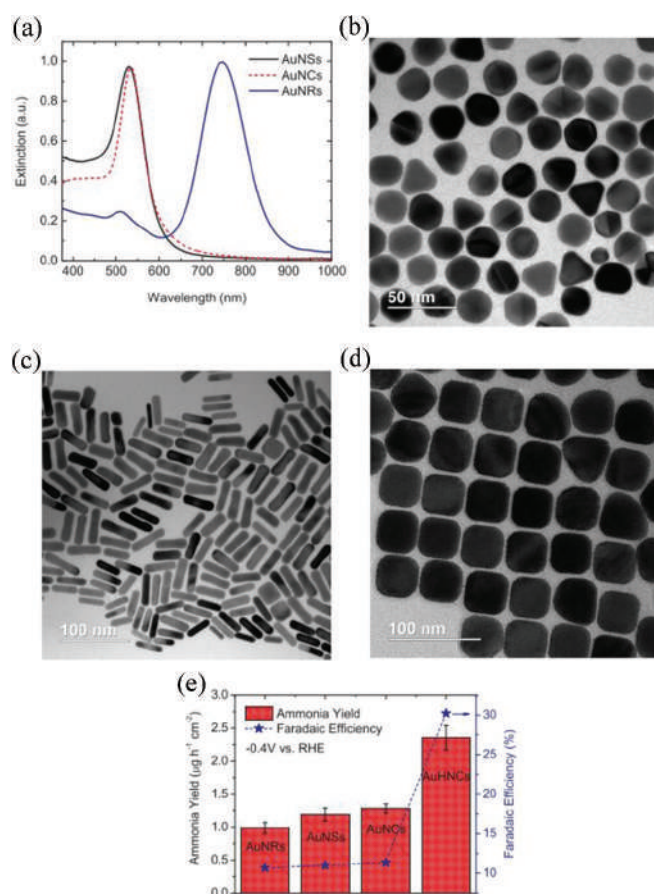


Figure 4. (a) UV-vis extinction spectra of AuNSs, AuNCs, and AuNRs. (b), (c), and (d) are the TEM images of AuNSs, AuNRs, and AuNCs, respectively. (e) Ammonia yield rate and Faradaic efficiency for nanoparticles of various types and shapes at the potential of -0.4 V vs RHE in 0.5 M LiClO₄ aqueous solution. Reproduced from Ref. [36] with permission from Elsevier B. V.

4. Compound Catalysts

4.1. Single-atom catalysts

Zhang et al. first proposed the single-atom catalyst in 2011,^[42] where a single-atom catalyst with atomically dispersed Pt atoms anchored on the surface of iron oxide was prepared to catalyze the CO oxidation. After this, single-atom catalysts have been fascinating systems in the field of catalysis owing to 100% active atomic utilization efficiency and uniform active centers with low atomic coordination number.^[43-46] To expose the active centers as much as possible, 2D materials are the preferred supports. So, the following discussions are focused on single-atom catalysts towards eNRR with the supports of 2D materials.

4.1.1. Single-TM-atom catalysts

Owing to the concept of “accept and backdonate” as aforementioned, TM atoms are also welcomed active centers in single-atom catalysts. Since 2D materials are the popular supports, it is necessary to discuss the eNRR catalysts with graphene, the well-known 2D material, being the support. Inspired by the fact that Fe plays an important role in activating N₂ in nitrogenases enzymes,^[47] Li et al. proposed that the FeN₃ active center supported on graphene was highly active for

N₂ reduction.^[48] The FeN₃ active center is highly spin-polarized, contributing to the adsorption and activation of N₂ molecule. After evaluating the three possible associative mechanisms, PDS of the FeN₃-embedded graphene is *N₂ + H⁺ + e⁻ → *N₂H or *NH₂ + H⁺ + e⁻ → *NH₃. Moreover, according to the charge population analysis, the FeN₃ active center acts as an electrons transmitter between graphene and adsorbed species.^[48] Similarly, with Fe being the active center, Wei et al. proposed that Fe-doped monolayer phosphorene as an eNRR catalyst using the spin-polarized DFT.^[49]

As for the systematic study on the possibility of graphene as the support of eNRR catalysts, Choi et al. systematically studied the single-TM-atom catalysts with defective graphene being the support, where 30 TM atoms with La being the representative of La-Gd were embedded into four models, including M@C₃, M@C₄, M@N₃, and M@N.^[50] Among 120 catalysts, Ti@N₄ and V@N₄ have the best catalytic activity with the PDS of 0.69 and 0.87 eV (Figure 5a, c), respectively, which are lower than that of the Ru(0001) stepped surface (0.98 eV). Besides the high activity, significantly improved eNRR selectivity on these catalysts was also found, compared to the corresponding surface of bulk metal (Figure 5b).

Such an excellent selectivity is the result of resemble effect, where *H on top site is the most stable for single-TM-atom catalysts while bridge or hollow site is preferred for pure metal. Moreover, due to the metal-support interaction, electronic structure of TM atoms are quite different from those of bulk TM. Charge transfer is universally present between metal and support, resulting in that the anchored TM atoms usually carry positive charge, hindering H⁺ approaching the metal.^[50]

Similar to Fe, Mo plays a key role in FeMo-cofactor of nitrogenases enzymes as well, and Mo-N_x complexes are promising eNRR molecular catalysts.^[51, 52] So, incorporating Mo-N_x moiety into 2D heterogeneous catalysts seems to be a highly efficient strategy for eNRR catalysts. In this regard, Zhao et al. proposed an advanced eNRR catalyst with Mo atoms anchored on the boron-vacancy of monolayer BN.^[53] Mo is the optimal one between Sc to Zn, Mo, Ru, Rh, Pd, and Ag, because of its abilities to adsorb N₂, selectively stabilize *N₂H and destabilize *NH₂. According to DFT calculation, lying-on and standing-on adsorbed N₂ were both stable on Mo-embedded BN, and eNRR can be processed on Mo-embedded BN at a potential of -0.35 V via the enzymatic mechanism. Similar to the FeN₃-embedded graphene, central Mo atom in Mo-embedded BN is also spin-polarized, and Mo-N₃ acts as a electron transmitter in the whole reduction process. In addition, Ling et al. proposed that Mo supported on N-doped graphene can catalyze eNRR with a overpotential of 0.24 V via the enzymatic mechanism,^[54] and Ou et al. proposed that Mo supported on N-doped black phosphorus can catalyze eNRR with a potential of 0.18 V via the distal mechanism.^[55]

Besides Fe and Mo, which are important elements in cofactors of nitrogenases enzymes, other TM atoms also act well in boosting eNRR. Single Pt atom embedded in monolayer g-C₃N₄ as efficient single-atom catalysts for NH₃ synthesis was explored by Yin et al.^[56] With DFT calculations, they found that Pt/g-C₃N₄ has excellent activity to catalyze eNRR with a low potential of -0.24 V at ambient conditions. Moreover, Pt/g-C₃N₄ is stable, and it has excellent conductivity. It is believed that the excellent activity of Pt/g-C₃N₄ came from its significant deviation from the linear scaling. To further study the origin of this deviation, N₂H and NH₂ adsorptions on Pt(111), an isolated Pt atom, and Pt/g-C₃N₄ were comparatively studied.^[56] In comparison with Pt(111) and an isolated Pt atom, embedding the isolated Pt atom in g-C₃N₄ completely cancels out the stability enhancement of *NH₂, while maintaining the stability of *N₂H. The single Pt atom and g-C₃N₄ work in concert to stabilize *N₂H and destabilize *NH₂, providing highly active sites for eNRR.

Embedding TM active centers into 2D materials has been extensive studied, and great progress has been made. Meanwhile, it is notable that discovering new materials is always attractive for new advances. In eNRR, by means of DFT calculations, Chen et al. designed a new

cobweb-like 2D MoC₆ structure (Figure 6a), and they found that MoC₆ can efficiently realize the N₂ to NH₃ process under ambient conditions.^[57] They suggested a feasible pathway to synthesis the MoC₆ structure, where two process are involved: the synthesis of graphyne, and the deposition of Mo atoms. For the catalytic process, N₂ is adsorbed on the bridge site from the orientation relationship of the frontier molecular orbitals (Figure 6b), and the following reduction of N₂ to NH₃ can be realized at a potential of -0.54 V via the enzymatic pathway (Figure 6c). Moreover, the adsorption energy of N₂ is -0.36 eV, stronger than that of H atom (-0.15 eV), showing that competing HER is inhibited.

4.1.2. Single-nonmetal-atom catalysts

The unique electronic structure of boron atom enables it to be alternative element for TM atoms as aforesaid, which means that single-nonmetal-atom catalysts and metal-free catalysts are possible for boosting eNRR. Yu et al. synthesized a boron-doped graphene as an efficient metal-free eNRR catalyst.^[58] Electron density redistribution in the graphene support is realized by doping boron, and the electron-deficient doping boron increases the adsorption energy of N₂ molecules. Among three boron-doped graphene structures, including BC₃, BC₂O, and BCO₂, BC₃ presents the lowest energy barrier of 0.43 eV for eNRR. After electrochemical tests, an excellent performance with a NH₃ production rate of 9.8 μg·hr⁻¹·cm⁻² and a Faradic efficiency of 10.8% at 0.5 V vs RHE was presented, while the performance of undoped graphene is poor.^[58] As for theoretical explorations, Ling et al. proposed that N₂ molecule can be efficiently adsorbed and reduced to NH₃ on B/g-C₃N₄, and the whole reduction process can be proceeded at a low potential of 0.20 V via the enzymatic mechanism. Meanwhile, B/g-C₃N₄ can absorb visible light well, which renders it ideal for solar-driven reduction of N₂.^[59] Ji et al. proposed that a boron-interstitial-doped C₂N layer can be an excellent metal-free eNRR catalyst. The doping boron is positive and magnetic, contributing to its high activity and high selectivity. The eNRR process prefers to proceed via the enzymatic mechanism with a potential of 0.15 V.^[60] Lv et al. proposed that B/g-CN can activate the adsorbed N₂ and further convert it to NH₃ with a overpotential of 0.15 V, and the activation barrier of PDS is 0.61 eV.^[61] Furthermore, Liu et al. modeled 21 catalysts with boron atoms anchored on eight 2D materials, including graphene, boron nitride, boron sulfide, black phosphorus, S-triazine-based g-C₃N₄, tri-s-triazine-based g-C₃N₄, h-MoS₂, and T-MoS₂, as shown in Figure 7a.^[62] Among these eNRR catalysts, single boron atoms supported on graphene or substituted into h-MoS₂ shows best catalytic activity towards eNRR. According to the charge analysis, the authors found that the catalytic activity is highly related to the charge transfer between the boron atom and the substrate. Boron site with more electrons has higher possibility to inject electron and activate N₂, and boron site with positive charge is obviously beneficial to inhibit HER, as indicated in Figure 7b.^[62]

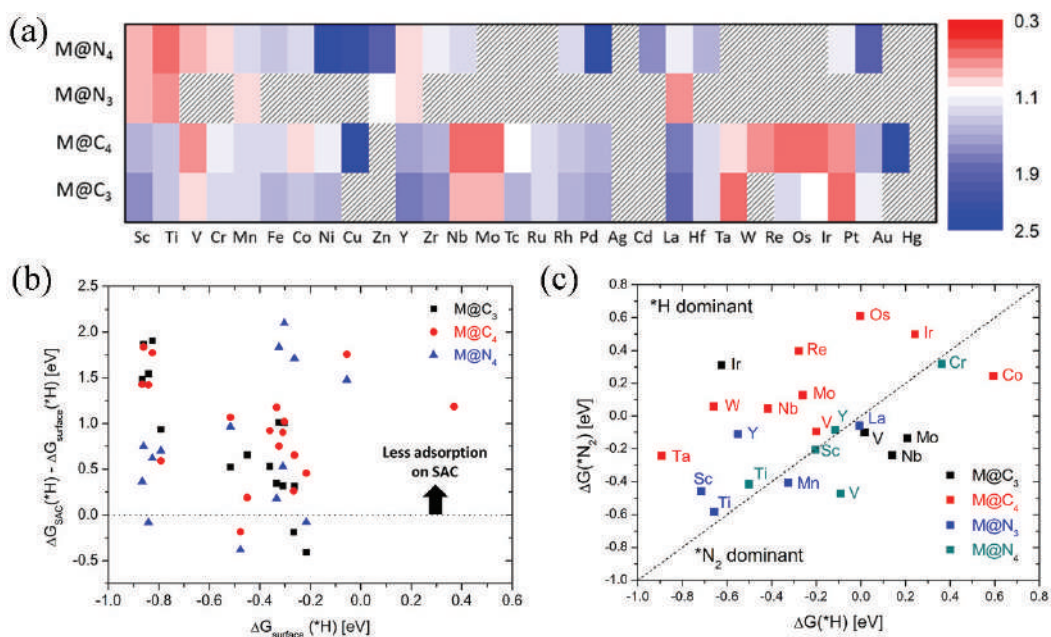


Figure 5. (a) Free energy (ΔG) of PDS on 120 single-atom catalysts, where single-atom catalysts filled with patterns represent thermodynamically unstable single-atom catalysts. (b) Difference between H adsorption free energy on the single-atom catalysts ($\Delta G_{SAC}(*H)$) and adsorption free energy on the surface ($\Delta G_{surface}(*H)$) of the same metal atoms. (c) Calculated $\Delta G(*H)$ and $\Delta G(*N_2)$ on single-atom catalysts that satisfy $\Delta G_{PDS} \leq 1.0$ eV. Dashed line indicates $\Delta G(*H) = \Delta G(*N_2)$. Reproduced from Ref. [50] with permission from American Chemical Society.

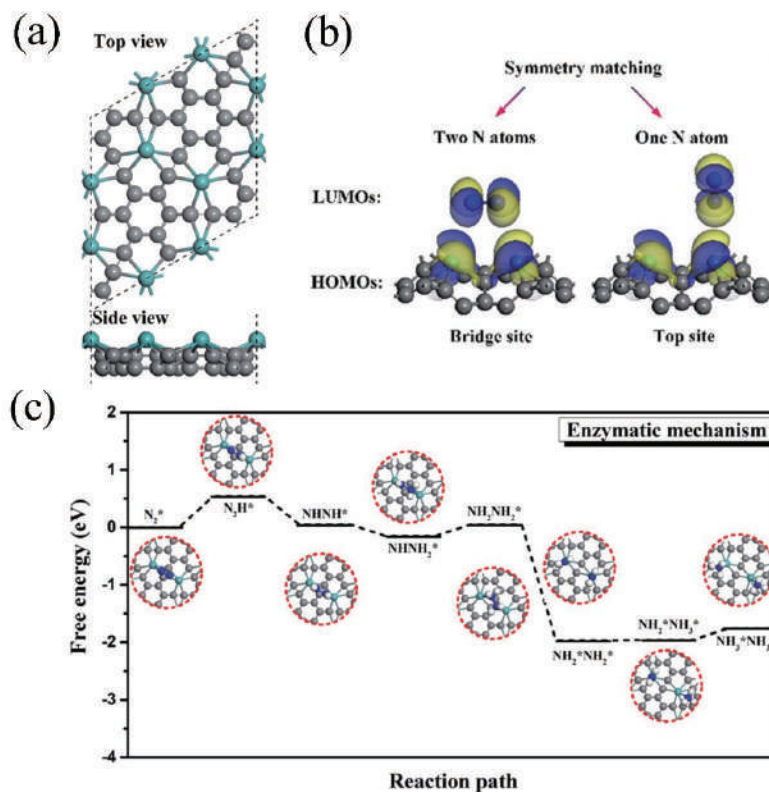


Figure 6. (a) Top and side views of the 2D MoC_6 , where black balls denote C atoms and the other balls denotes Mo atoms. (b) Symmetry matching between the lowest unoccupied molecular orbitals (LUMOs) of N_2 and the highest occupied molecular orbitals (HOMOs) of MoC_6 , including bridge site and top site. The yellow and blue shadows represent frontier molecular orbitals. (c) The enzymatic mechanism for eNRR on MoC_6 . The free energy profiles and the structures of intermediates are shown in the reaction path. Reproduced from Ref. [57] with permission from The Royal Society of Chemistry.

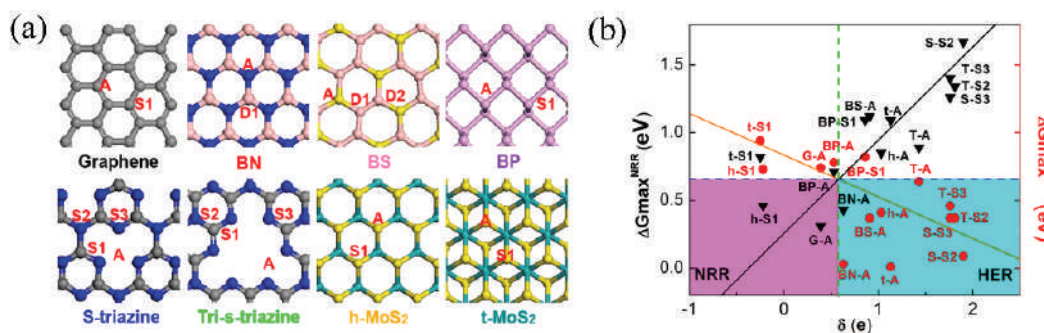


Figure 7. Proposed 2D materials and potential B-sites. The numbers indicate different bonding environments described in the text. Black, blue, rose, yellow, purple, and cyan spheres represent C, N, B, S, P, and Mo, respectively. (b) Computational screening of 14 catalyst combinations in terms of $\Delta G_{\max}^{\text{HER}}$ and $\Delta G_{\max}^{\text{NRR}}$ vs Bader charge (δ , in units of e) of single boron in or on a 2D substrate. Reproduced from Ref. [62] with permission from American Chemical Society.

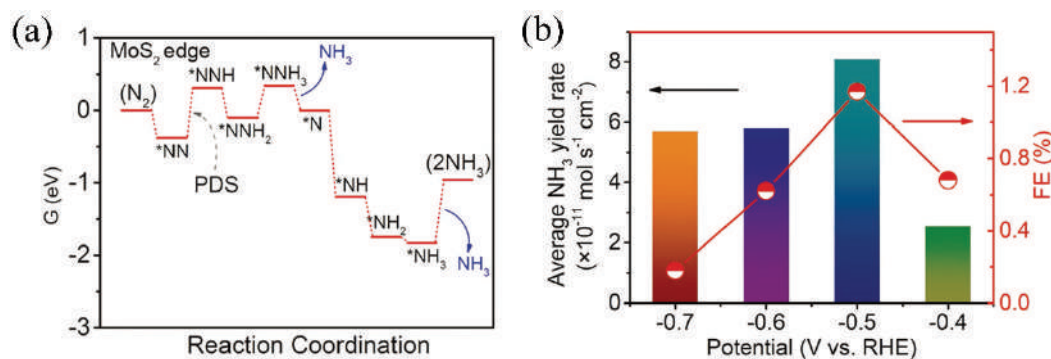


Figure 8. Free-energy profile for eNRR at MoS₂ edge site. (b) Average NH₃ yields and Faradaic efficiencies (FEs) of MoS₂/CC at different potentials in 0.1 M Na₂SO₄ at room temperature and ambient pressure. Reproduced from Ref. [66] with permission from Wiley-VCH.

4.2. Transition metal nitrides

Abghoui et al. proposed that the transition metal mononitrides can act as cost-efficient catalysts to convert N₂ molecule to NH₃ under ambient conditions, where a low applied bias is only required.^[63] By means of DFT calculations, the most promising catalysts are VN, ZrN, NbN and CrN among 25 considered TM mononitrides. Moreover, the competing HER is inhibited for above four mononitrides, which differs to the cases of pure metals. Since the structural particularity of TM mononitrides, the authors explored the poisoning and possible decomposition, and they pointed that, under operating conditions, ZrN, NbN and CrN should be single-crystal surfaces because polycrystalline surfaces may be decomposed, while polycrystalline surfaces of VN may be used.^[63] Li et al. proposed that transition metal binitride nanosheet, MoN₂, as an eNRR catalyst at ambient conditions with the scheme of DFT.^[64] Different to transition metal mononitrides, MoN₂ is a 2D layered material. According to calculations, MoN₂ acts well in adsorbing and activating N₂ molecule, but large energy is required to refresh the MoN₂ surface. To improve the performance, Fe-doping was used, which can significantly improve it to proceed the whole reduction reaction with an overpotential of 0.47 V.

In experiments, Zhang et al. synthesized MoN

nanosheets array grown on carbon cloth (MoN NA/CC) to catalyze eNRR.^[65] This catalyst achieved a NH₃ yield of $3.01 \times 10^{-10} \text{ mol s}^{-1} \text{ cm}^{-2}$ and a Faradaic efficiency of 1.15% at -0.3 V vs RHE in 0.1 M HCl under ambient conditions. After theoretical calculations of free energy profile, the PDS of MoN NA/CC to catalyze eNRR is the second protonation of the surface N.

4.3. Transition metal dichalcogenides

As emerging 2D materials, transition metal dichalcogenides have attracted worldwide interests because of the unique physical, chemical, and mechanical properties. Zhang et al. first explored the possibility of MoS₂ as an eNRR catalyst.^[66] To evaluate the possibility of MoS₂ to catalyze eNRR, the electronic structures of MoS₂ and the energy profile of eNRR were explored using DFT calculations. The results showed that the basal plane is inert to absorb N₂ molecule while the edge appeared to be active, and the energy profile indicated that the PDS is the first hydrogenation of $^*\text{N}_2$ with a barrier of 0.68 eV (Figure 8a). After this, the authors synthesized MoS₂ nanosheet array grown on carbon cloth (MoS₂/CC) to catalyze eNRR, and the NH₃ yield rate and Faradaic efficiency can reach $8.08 \times 10^{-11} \text{ mol s}^{-1} \text{ cm}^{-2}$ and 1.17%, respectively. Moreover, Li et al. further improved the performance of MoS₂ on eNRR by synthesizing defect-rich MoS₂ nanoflowers, where the active centers are on the basal

plane.^[67] In 0.1 M Na₂SO₄, this catalyst attained a Faradic efficiency of 8.34% and a NH₃ yield of 29.28 μg h⁻¹ mg⁻¹_{cat.} at -0.40 V versus RHE, significantly higher than those of defect-free MoS₂ nanosheet (2.18% and 13.41 μg h⁻¹ mg⁻¹_{cat.}). The vacancy with one missing Mo atom and two missing S atoms was regarded as the active sites, and the PDS of the eNRR process was calculated to be *NH₂→*NH₃ with the PDS of 0.60 eV, which is less than the edge Mo atoms (0.68 eV).^[66]

The edge Mo atoms and the defect in basal plane of MoS₂ can be active centers for eNRR, suggesting the potential of transition metal dichalcogenides as efficient eNRR catalysts. In addition, as a 2D material, MoS₂ absolutely can act as support to anchor the active centers. Suryanto et al. synthesized Ru/MoS₂ to catalyze eNRR, and a Faradaic efficiency of 17.6% and a NH₃ yield rate of 1.14 × 10⁻¹⁰ mol cm⁻² s⁻¹ were obtained at 50 °C.^[68] The corresponding DFT calculations carried out with a hcp Ru₁₁₇ nanocluster on MoS₂ suggested that PDS is *NH₂→*NH₃ with a barrier of 0.35 eV through the dissociative mechanism. In this model, the S-vacancies on MoS₂ provides a fundamental role in eNRR process to provide H adatom, where the already formed *H can be transferred to nearby bound *N₂ or *NH_x.^[68]

Besides conventional MoS₂, a new class of 2D materials called “Janus” MoSSe has been recently synthesized with Mo atomic layer being sandwiched between S and Se ones.^[69, 70] Similar to MoS₂, MoSSe has shown good catalytic performances.^[71, 72] As for its possible application in eNRR, Li et al. performed a theoretical screening of different TM atoms anchored on the S- or Se-vacancy of monolayer MoSSe as efficient eNRR catalysts.^[73] According to the screening, Mo atom anchored on the S-vacancy presents the highest activity with a potential of -0.49 V, while HER is significantly inhibited due to larger free energy of *H adsorption.

4.4. Transition metal carbides

From the d orbital theory, transition metal carbides should have good adsorption ability for electron-enriched adsorbates because of the unoccupied d orbitals.^[74] Among various transition metal carbides, Mo₂C has exhibited a potential application in catalytic hydrogenation.^[75, 76] Moreover, the Mo-based materials have shown excellent performance in eNRR as stated above. According to this, Cheng et al. synthesized Mo₂C nanodots supported on ultrathin carbon nanosheets (Mo₂C/C) to fix N₂ molecule and catalyze the eNRR. The as-synthesized Mo₂C/C nanosheets presented promising catalytic performance with a NH₃ yield rate of 11.3 μg h⁻¹ mg⁻¹_{cat.} and a Faradic efficiency of 7.8% under ambient conditions.^[77]

Outlook: Exploring highly-performance eNRR catalysts has emerged as a new research hotspot. In theoretical calculations, various catalysts show excellent catalytic activity, especially the single-atom catalysts. However, most practically synthesized catalysts towards eNRR are based on the active centers from the defects. Though

several single-atom eNRR catalysts have been fabricated, the corresponding loading of active site is usually kept at a low level or the heteroatoms are usually aggregated to nanoclusters. On the other hand, theoretical calculations neglect some important respects, such as the electrode-catalyst interface, the catalyst-electrolyte interface, and the mass and electron transportation. More instructive theoretical calculation should be developed, and consequently bridge the gap between theoretical calculations and experiments.

Acknowledgement: This project is financially supported by the National Natural Science Foundation of China (Nos. 61674069 and 51631004), the Key Scientific and Technological Research and Development Project of Jilin Province (20180201080GX), the Fundamental Research Funds for the Central Universities, and the Program for JLU Science and Technology Innovative Research Team (No. 2017TD-09).

References

- [1] S.L. Foster, S.I.P. Bakovic, R.D. Duda, S. Maheshwari, R.D. Milton, S.D. Minteer, M.J. Janik, J.N. Renner, L.F. Greenlee, Catalysts for nitrogen reduction to ammonia, *Nature Catalysis* 1(7) (2018) 490.
- [2] J. Guo, P. Chen, Catalyst: NH₃ as an energy carrier, *Chem* 3(5) (2017) 709-712.
- [3] C.H. Christensen, T. Johannessen, R.Z. Sørensen, J.K. Nørskov, Towards an ammonia-mediated hydrogen economy?, *Catal. Today* 111(1-2) (2006) 140-144.
- [4] S.J. Li, D. Bao, M.M. Shi, B.R. Wulan, J.M. Yan, Q. Jiang, Amorphizing of Au nanoparticles by CeOx-RGO hybrid support towards highly efficient electrocatalyst for N₂ reduction under ambient conditions, *Adv. Mater.* 29(33) (2017) 1700001.
- [5] M.M. Shi, D. Bao, S.J. Li, B.R. Wulan, J.M. Yan, Q. Jiang, Anchoring PdCu amorphous nanocluster on graphene for electrochemical reduction of N₂ to NH₃ under ambient conditions in aqueous solution, *Advanced Energy Materials* 8(21) (2018) 1800124.
- [6] Y. Ashida, K. Arashiba, K. Nakajima, Y. Nishibayashi, Molybdenum-catalysed ammonia production with samarium diiodide and alcohols or water, *Nature* 568(7753) (2019) 536.
- [7] R.D. Milton, R. Cai, S. Abdellaoui, D. Leech, A.L. De Lacey, M. Pita, S.D. Minteer, Bioelectrochemical Haber–Bosch Process: An Ammonia-Producing H₂/N₂ Fuel Cell, *Angew. Chem. Int. Ed.* 56(10) (2017) 2680-2683.
- [8] D. Bao, Q. Zhang, F.L. Meng, H.X. Zhong, M.M. Shi, Y. Zhang, J.M. Yan, Q. Jiang, X.B. Zhang, Electrochemical reduction of N₂ under ambient conditions for artificial N₂ fixation and renewable energy storage using N₂/NH₃ cycle, *Adv. Mater.* 29(3) (2017) 1604799.
- [9] P.J. Chirik, Nitrogen fixation: one electron at a time, *Nature chemistry* 1(7) (2009) 520.

- [10] Z.W. Chen, J.M. Yan, Q. Jiang, Single or Double: Which Is the Altar of Atomic Catalysts for Nitrogen Reduction Reaction?, *Small Methods* (2018) 1800291.
- [11] X. Cui, C. Tang, Q. Zhang, A review of electrocatalytic reduction of dinitrogen to ammonia under ambient conditions, *Advanced Energy Materials* 8(22) (2018) 1800369.
- [12] B.H. Suryanto, H.-L. Du, D. Wang, J. Chen, A.N. Simonov, D.R. MacFarlane, Challenges and prospects in the catalysis of electroreduction of nitrogen to ammonia, *Nature Catalysis* (2019) 1.
- [13] B.K. Burgess, D.J. Lowe, Mechanism of molybdenum nitrogenase, *Chem. Rev.* 96(7) (1996) 2983-3012.
- [14] R.R. Eady, Structure–function relationships of alternative nitrogenases, *Chem. Rev.* 96(7) (1996) 3013-3030.
- [15] Y. Wan, J. Xu, R. Lv, Heterogeneous electrocatalysts design for nitrogen reduction reaction under ambient conditions, *Mater. Today* (2019).
- [16] X. Liu, Y. Jiao, Y. Zheng, M. Jaroniec, S.-Z. Qiao, Building Up a Picture of the Electrocatalytic Nitrogen Reduction Activity of Transition Metal Single-Atom Catalysts, *J. Am. Chem. Soc.* 141(24) (2019) 9664-9672.
- [17] X. Guo, H. Du, F. Qu, J. Li, Recent progress in electrocatalytic nitrogen reduction, *Journal of Materials Chemistry A* 7(8) (2019) 3531-3543.
- [18] H. Zhou, J. Li, Z. Wen, Q. Jiang, Tuning catalytic activity of single Mo atom supported on graphene for nitrogen reduction via Se atom doping, *PCCP* (2019).
- [19] Y. Zhang, H. Du, Y. Ma, L. Ji, H. Guo, Z. Tian, H. Chen, H. Huang, G. Cui, A.M. Asiri, Hexagonal boron nitride nanosheet for effective ambient N₂ fixation to NH₃, *Nano Research* 12(4) (2019) 919-924.
- [20] J. Zhao, X. Ren, X. Li, D. Fan, X. Sun, H. Ma, Q. Wei, D. Wu, High-performance N₂-to-NH₃ fixation by a metal-free electrocatalyst, *Nanoscale* 11(10) (2019) 4231-4235.
- [21] X. Li, X. Ren, X. Liu, J. Zhao, X. Sun, Y. Zhang, X. Kuang, T. Yan, Q. Wei, D. Wu, A MoS₂ nanosheet–reduced graphene oxide hybrid: an efficient electrocatalyst for electrocatalytic N₂ reduction to NH₃ under ambient conditions, *Journal of Materials Chemistry A* 7(6) (2019) 2524-2528.
- [22] Y. Liu, M. Han, Q. Xiong, S. Zhang, C. Zhao, W. Gong, G. Wang, H. Zhang, H. Zhao, Dramatically Enhanced Ambient Ammonia Electrosynthesis Performance by In-Operando Created Li–S Interactions on MoS₂ Electrocatalyst, *Advanced Energy Materials* (2019) 1803935.
- [23] A.R. Singh, B.A. Rohr, J.A. Schwalbe, M. Cargnello, K. Chan, T.F. Jaramillo, I. Chorkendorff, J.K. Nørskov, Electrochemical Ammonia Synthesis The Selectivity Challenge, ACS Publications, 2016.
- [24] Y. Huang, T. Yang, L. Yang, R. Liu, G. Zhang, J. Jiang, Y. Luo, P. Lian, S. Tang, Graphene—Boron Nitride Hybrid Supported Single Mo Atom Electrocatalysts for Efficient Nitrogen Reduction Reaction, *Journal of Materials Chemistry A* (2019).
- [25] L. Xia, J. Yang, H. Wang, R. Zhao, H. Chen, W. Fang, A.M. Asiri, F. Xie, G. Cui, X. Sun, Sulfur-doped graphene for efficient electrocatalytic N₂-to-NH₃ fixation, *Chem. Commun.* 55(23) (2019) 3371-3374.
- [26] Y. Ying, K. Fan, X. Luo, H. Huang, Predicting two-dimensional pentagonal transition metal monophosphides for efficient electrocatalytic nitrogen reduction, *Journal of Materials Chemistry A* 7(18) (2019) 11444-11451.
- [27] Z.W. Seh, J. Kibsgaard, C.F. Dickens, I. Chorkendorff, J.K. Nørskov, T.F. Jaramillo, Combining theory and experiment in electrocatalysis: Insights into materials design, *Science* 355(6321) (2017) eaad4998.
- [28] Z.W. Chen, W. Gao, W.T. Zheng, Q. Jiang, Steric Hindrance in Sulfur Vacancy of Monolayer MoS₂ Boosts Electrochemical Reduction of Carbon Monoxide to Methane, *ChemSusChem* 11(9) (2018) 1455-1459.
- [29] C.-X. Zhao, G.-X. Zhang, W. Gao, Q. Jiang, Single metal atoms regulated flexibly by a 2D InSe substrate for CO₂ reduction electrocatalysts, *Journal of Materials Chemistry A* 7(14) (2019) 8210-8217.
- [30] F. Gao, X. Tang, H. Yi, S. Zhao, C. Li, J. Li, Y. Shi, X. Meng, A review on selective catalytic reduction of NO_x by NH₃ over Mn–based catalysts at low temperatures: catalysts, mechanisms, kinetics and DFT calculations, *Catalysts* 7(7) (2017) 199.
- [31] M. Krajčí, J. Hafner, Intermetallic compounds as selective heterogeneous catalysts: insights from DFT, *ChemCatChem* 8(1) (2016) 34-48.
- [32] E. Skúlason, T. Bligaard, S. Gudmundsdóttir, F. Studt, J. Rossmeisl, F. Abild-Pedersen, T. Vegge, H. Jonsson, J.K. Nørskov, A theoretical evaluation of possible transition metal electro-catalysts for N₂ reduction, *PCCP* 14(3) (2012) 1235-1245.
- [33] E. Skúlason, V. Tripkovic, M.E. Björketun, S. Gudmundsdóttir, G. Karlberg, J. Rossmeisl, T. Bligaard, H. Jónsson, J.K. Nørskov, Modeling the electrochemical hydrogen oxidation and evolution reactions on the basis of density functional theory calculations, *The Journal of Physical Chemistry C* 114(42) (2010) 18182-18197.
- [34] J.H. Montoya, C. Tsai, A. Vojvodic, J.K. Nørskov, The Challenge of Electrochemical Ammonia Synthesis: A New Perspective on the Role of Nitrogen Scaling Relations, *ChemSusChem* 8(13) (2015) 2180-2186.
- [35] D. Yang, T. Chen, Z. Wang, Electrochemical reduction of aqueous nitrogen (N₂) at a low overpotential on (110)-oriented Mo nanofilm, *Journal of Materials Chemistry A* 5(36) (2017) 18967-18971.
- [36] M. Nazemi, S.R. Panikkanvalappil, M.A. El-Sayed, Enhancing the rate of electrochemical nitrogen reduction reaction for ammonia synthesis under

- ambient conditions using hollow gold nanocages, *Nano Energy* 49 (2018) 316-323.
- [37] H. Huang, L. Xia, X. Shi, A.M. Asiri, X. Sun, Ag nanosheets for efficient electrocatalytic N₂ fixation to NH₃ under ambient conditions, *Chem. Commun.* 54(81) (2018) 11427-11430.
- [38] M.-A. Légaré, G. Bélanger-Chabot, R.D. Dewhurst, E. Welz, I. Krummenacher, B. Engels, H. Braunschweig, Nitrogen fixation and reduction at boron, *Science* 359(6378) (2018) 896-900.
- [39] C. Liu, Q. Li, J. Zhang, Y. Jin, D.R. MacFarlane, C. Sun, Theoretical evaluation of possible 2D boron monolayer in N₂ electrochemical conversion into ammonia, *The Journal of Physical Chemistry C* 122(44) (2018) 25268-25273.
- [40] X. Zhang, T. Wu, H. Wang, R. Zhao, H. Chen, T. Wang, P. Wei, Y. Luo, Y. Zhang, X. Sun, Boron Nanosheet: An Elemental Two-Dimensional (2D) Material for Ambient Electrocatalytic N₂-to-NH₃ Fixation in Neutral Media, *ACS Catalysis* 9 (2019) 4609-4615.
- [41] L. Zhang, L.X. Ding, G.F. Chen, X. Yang, H. Wang, Ammonia Synthesis Under Ambient Conditions: Selective Electroreduction of Dinitrogen to Ammonia on Black Phosphorus Nanosheets, *Angew. Chem.* 131(9) (2019) 2638-2642.
- [42] B. Qiao, A. Wang, X. Yang, L.F. Allard, Z. Jiang, Y. Cui, J. Liu, J. Li, T. Zhang, Single-atom catalysis of CO oxidation using Pt₁/FeO_x, *Nature chemistry* 3(8) (2011) 634.
- [43] Z.W. Chen, L.X. Chen, C. Yang, Q. Jiang, Atomic (Single, Double, and Triple Atoms) Catalysis: Frontiers, Opportunities, and Challenges, *Journal of Materials Chemistry A* 7(8) (2019).
- [44] Y. Wang, J. Mao, X. Meng, L. Yu, D. Deng, X. Bao, Catalysis with two-dimensional materials confining single atoms: concept, design, and applications, *Chem. Rev.* 119(3) (2018) 1806-1854.
- [45] A. Wang, J. Li, T. Zhang, Heterogeneous single-atom catalysis, *Nature Reviews Chemistry* 2(6) (2018) 65.
- [46] N. Xuan, J. Chen, J. Shi, Y. Yue, P. Zhuang, K. Ba, Y. Sun, J. Shen, Y. Liu, B. Ge, Single-Atom Electroplating on Two Dimensional Materials, *Chem. Mater.* 31(2) (2018) 429-435.
- [47] B.M. Hoffman, D.R. Dean, L.C. Seefeldt, Climbing nitrogenase: toward a mechanism of enzymatic nitrogen fixation, *Acc. Chem. Res.* 42(5) (2009) 609-619.
- [48] X.F. Li, Q.K. Li, J. Cheng, L. Liu, Q. Yan, Y. Wu, X.H. Zhang, Z.Y. Wang, Q. Qiu, Y. Luo, Conversion of Dinitrogen to Ammonia by FeN₃-Embedded Graphene, *J. Am. Chem. Soc.* 138(28) (2016) 8706.
- [49] Z. Wei, Y. Zhang, S. Wang, C. Wang, J. Ma, Fe-doped phosphorene for the nitrogen reduction reaction, *Journal of Materials Chemistry A* 6(28) (2018) 13790-13796.
- [50] C. Choi, S. Back, N.-Y. Kim, J. Lim, Y.-H. Kim, Y. Jung, Suppression of hydrogen evolution reaction in electrochemical N₂ reduction using single-atom catalysts: A computational guideline, *ACS Catalysis* 8(8) (2018) 7517-7525.
- [51] Y. Nishibayashi, Recent progress in transition-metal-catalyzed reduction of molecular dinitrogen under ambient reaction conditions, *Inorg. Chem.* 54(19) (2015) 9234-9247.
- [52] H. Tanaka, Y. Nishibayashi, K. Yoshizawa, Interplay between theory and experiment for ammonia synthesis catalyzed by transition metal complexes, *Acc. Chem. Res.* 49(5) (2016) 987-995.
- [53] J. Zhao, Z. Chen, Single Mo atom supported on defective boron nitride monolayer as an efficient electrocatalyst for nitrogen fixation: a computational study, *J. Am. Chem. Soc.* 139(36) (2017) 12480-12487.
- [54] C. Ling, X. Bai, Y. Ouyang, A. Du, J. Wang, Single molybdenum atom anchored on N-doped carbon as a promising electrocatalyst for nitrogen reduction into ammonia at ambient conditions, *The Journal of Physical Chemistry C* 122(29) (2018) 16842-16847.
- [55] P. Ou, X. Zhou, F. Meng, C. Chen, Y. Chen, J. Song, Single Molybdenum Center Supported on N-Doped Black Phosphorus as an Efficient Electrocatalyst for Nitrogen Fixation, *Nanoscale* (2019).
- [56] H. Yin, S.-L. Li, L.-Y. Gan, P. Wang, Pt-embedded in monolayer gC₃N₄ as a promising single-atom electrocatalyst for ammonia synthesis, *Journal of Materials Chemistry A* 7(19) (2019) 11908-11914.
- [57] Z. Chen, X. Lang, Q. Jiang, Discovery of cobweb-like MoC₆ and its application for nitrogen fixation, *Journal of Materials Chemistry A* 6(20) (2018) 9623-9628.
- [58] X. Yu, P. Han, Z. Wei, L. Huang, Z. Gu, S. Peng, J. Ma, G. Zheng, Boron-doped graphene for electrocatalytic N₂ reduction, *Joule* 2(8) (2018) 1610-1622.
- [59] C. Ling, X. Niu, Q. Li, A. Du, J. Wang, Metal-free single atom catalyst for N₂ fixation driven by visible light, *J. Am. Chem. Soc.* 140(43) (2018) 14161-14168.
- [60] S. Ji, Z. Wang, J. Zhao, A boron-interstitial doped C₂N layer as a metal-free electrocatalyst for N₂ fixation: a computational study, *Journal of Materials Chemistry A* 7(5) (2019) 2392-2399.
- [61] X. Lv, W. Wei, F. Li, B. Huang, Y. Dai, Metal-Free B@ g-CN: Visible/Infrared Light-Driven Single Atom Photocatalyst Enables Spontaneous Dinitrogen Reduction to Ammonia, *Nano Lett.* (2019).
- [62] C. Liu, Q. Li, C. Wu, J. Zhang, Y. Jin, D.R. MacFarlane, C. Sun, Single-boron catalysts for nitrogen reduction reaction, *J. Am. Chem. Soc.* (2019).
- [63] Y. Abghoui, A.L. Garden, J.G. Howalt, T. Vegge, E. Skúlason, Electroreduction of N₂ to ammonia at ambient conditions on mononitrides of Zr, Nb, Cr, and V: A DFT

- guide for experiments, *Acs Catalysis* 6(2) (2015) 635-646.
- [64] Q. Li, L. He, C. Sun, X. Zhang, Computational study of MoN₂ monolayer as electrochemical catalysts for nitrogen reduction, *The Journal of Physical Chemistry C* 121(49) (2017) 27563-27568.
- [65] L. Zhang, X. Ji, X. Ren, Y. Luo, X. Shi, A.M. Asiri, B. Zheng, X. Sun, Efficient electrochemical N₂ reduction to NH₃ on MoN nanosheets array under ambient conditions, *ACS Sustainable Chemistry & Engineering* 6(8) (2018) 9550-9554.
- [66] L. Zhang, X. Ji, X. Ren, Y. Ma, X. Shi, Z. Tian, A.M. Asiri, L. Chen, B. Tang, X. Sun, Electrochemical ammonia synthesis via nitrogen reduction reaction on a MoS₂ catalyst: theoretical and experimental studies, *Adv. Mater.* 30(28) (2018) 1800191.
- [67] X. Li, T. Li, Y. Ma, Q. Wei, W. Qiu, H. Guo, X. Shi, P. Zhang, A.M. Asiri, L. Chen, Boosted Electrochemical N₂ Reduction to NH₃ by Defect-Rich MoS₂ Nanoflower, *Advanced Energy Materials* 8(30) (2018) 1801357.
- [68] B.H. Suryanto, D. Wang, L.M. Azofra, M. Harb, L. Cavallo, R. Jalili, D.R. Mitchell, M. Chatti, D.R. MacFarlane, MoS₂ polymorphic engineering enhances selectivity in the electrochemical reduction of nitrogen to ammonia, *ACS Energy Letters* 4(2) (2018) 430-435.
- [69] A.-Y. Lu, H. Zhu, J. Xiao, C.-P. Chuu, Y. Han, M.-H. Chiu, C.-C. Cheng, C.-W. Yang, K.-H. Wei, Y. Yang, Janus monolayers of transition metal dichalcogenides, *Nature nanotechnology* 12(8) (2017) 744.
- [70] J. Zhang, S. Jia, I. Kholmanov, L. Dong, D. Er, W. Chen, H. Guo, Z. Jin, V.B. Shenoy, L. Shi, Janus monolayer transition-metal dichalcogenides, *ACS nano* 11(8) (2017) 8192-8198.
- [71] C. Xia, W. Xiong, J. Du, T. Wang, Y. Peng, J. Li, Universality of electronic characteristics and photocatalyst applications in the two-dimensional Janus transition metal dichalcogenides, *Physical Review B* 98(16) (2018) 165424.
- [72] D. Er, H. Ye, N.C. Frey, H. Kumar, J. Lou, V.B. Shenoy, Prediction of enhanced catalytic activity for hydrogen evolution reaction in Janus transition metal dichalcogenides, *Nano Lett.* 18(6) (2018) 3943-3949.
- [73] L. Li, B. Li, Q. Guo, B. Li, Theoretical Screening of Single-Atom Anchored MoSSe Nanosheets for Electrocatalytic N₂ Fixation, *The Journal of Physical Chemistry C* (2019).
- [74] R. Michalsky, Y.-J. Zhang, A.J. Medford, A.A. Peterson, Departures from the adsorption energy scaling relations for metal carbide catalysts, *The Journal of Physical Chemistry C* 118(24) (2014) 13026-13034.
- [75] Y. Shi, Y. Yang, Y.-W. Li, H. Jiao, Mechanisms of Mo₂C (101)-catalyzed furfural selective hydrodeoxygenation to 2-methylfuran from computation, *ACS Catalysis* 6(10) (2016) 6790-6803.
- [76] W. Liu, B. Chen, X. Duan, K.-H. Wu, W. Qi, X. Guo, B. Zhang, D. Su, Molybdenum carbide modified nanocarbon catalysts for alkane dehydrogenation reactions, *ACS Catalysis* 7(9) (2017) 5820-5827.
- [77] H. Cheng, L.X. Ding, G.F. Chen, L. Zhang, J. Xue, H. Wang, Molybdenum carbide nanodots enable efficient electrocatalytic nitrogen fixation under ambient conditions, *Adv. Mater.* 30(46) (2018) 1803694.

Kansei Engineering Analysis of Purple-clay Teapot Based on Online Comment Data

Xinyu ZHANG¹, Bin QI^{1*}, Yanpu YANG², Xiaoming SUN¹

¹ Shandong University of Technology, Zibo, China

² Chang'an University, Xi'an, China

*Corresponding Author: Bin Qi, Shandong University of Technology, 255049, China; email: billboard0626@163.com

Abstract:

Product form has become an important communication medium between designers and consumers. Therefore, the collection and analysis of consumer evaluation of products can provide an important reference index for product form design. In this paper, purple-clay teapot was taken as an example and comments of Tmall consumers were collected through web crawler, and the product image vocabulary was extracted to analyze the needs of users. Using the research method of Kansei Engineering, the semantic space of the modeling and image of purple-clay teapot was established, and the relationship between the modeling elements and the image of purple-clay teapot was searched, which could provide valuable reference for the modeling design of purple-clay teapot.

Keywords: Kansei Engineering; image semantic; purple-clay teapot; crawler; quantitative theory

1. Introduction

As a unique pottery and clay handicraft in China, purple-clay teapot is a branch with distinct characteristics in Chinese ceramic culture. It combines the artistry of arts and crafts with the practicality of articles for daily use, which is closer to people's daily life. The unique shape of the purple-clay teapot can show its different emotional experience. In this paper, consumers' emotional image of purple-clay teapot was acquired through web crawler to research the relationship between modeling elements and image semantics of purple-clay teapot. When the craftsmen and designers design the purple-clay teapot, certain theoretical guidance can be provided according to the research on consumer demand.

2. Theoretical Basis and Technical Route

2.1. Kansei engineering

Originated in Japan, Kansei Engineering (KE) is a set of theories and methods to quantify the emotional psychological factors of users, which was put forward in 1970 by Mitsuo Nagamachi^[1], a scholar at Hiroshima University in Japan, and Kenichi Yamamoto, former chairman of Mazda automobile group. KE was initially put forward to better understand the needs of consumers and

to express the subconscious requirements of consumers on product attributes in a more clear and objective way. It can quantify irrational and difficult to describe emotional and psychological factors into rational expression, and finally establish a set of new product research and development system oriented by consumer demand. Analysis of KE is often used to understand consumers' expectations on product modeling, color, texture, layout, etc., and to explore consumers' feelings and demands for products^[2], so as to better guide the design.

2.2. Data-driven

Data-driven is a method to acquire, analyze and process massive data in time. Data-driven analysis combined with KE can enable designers to have many advantages in design analysis^[3]. Data-driven method has the following advantages: perceptual words are derived from user's comment data for this kind of products, and the collected perceptual words are highly targeted; the online comment data-oriented perceptual evaluation method is adopted to ensure the authenticity of the comment data; and the crawler program is used to automatically collect data, which makes the data collection efficient and numerical^[4]. In this paper, the first-hand evaluation data from consumers on purple-clay teapot can be directly obtained through data mining, which was not instructive, and the emotional words

collected are highly targeted to cases. A large number of online comment data were used for emotional evaluation, which can better ensure the authenticity and reliability of comment data. Moreover, the way of collecting data through web crawler is characterized by high efficiency, strong real-time performance and large amount of data collection.

2.3. Quantification-I theory

Quantification-I theory [5,6,7] is a method to establish the relationship between variables by using mathematical

model. For the field of Kansei Engineering, by establishing a mathematical model based on Quantification-I theory, qualitative problems can be quantitatively analyzed, which can more intuitively and clearly analyze the relationship between the emotional image of consumers and the form elements of modeling design^[8,9,10], and apply the analysis results to product design innovation.

In this paper, form elements of purple-clay teapot were analyzed by combining KE, data-driven and quantitative theories, and the research technical route is shown in Figure 1.

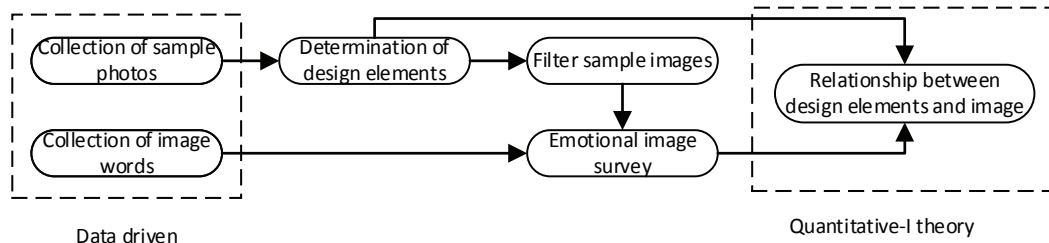


Figure 1. Research Technical Route



Figure 2. 64 Classic purple-clay teapot

Table 1. Feature Coding Matrix for Design of Morphological Elements

	Category C11	Category C12	Category C13	Category C14	Category C15	Category C16	Category C17	Category C18
Kettle body modelling element C1j								
	Spherical C11	Elliptical (vertical) C12	Elliptic (transverse) C13	Cylindrical C14	Cylindrical C15	Inverted table C16	Square platform C17	Square C18
Kettle spit modelling element C2j								
	Curved spit 1, C21	Curved spit 2, C22	Curved spit 3, C23	Straight spit, C24	Short straight spit, C25			
Kettle handle modelling element C3j								
	Arc front ear handle C31	Arc inverted ear handle C32	Handle with straight line C33	Round ear handle C34	Handle C34	Lifting beam handle C36	Flying kettle handle C37	
Kettle cover modelling element C4j								
	Nested cover pot C41	Pressing cover pot C42	Cutting cover pot C43					
Kettle button modelling element C5j								
	Spherical C51	Cylindrical C52	Bridge shape C53	Ellipse C54	Transverse ellipse C55			
Pott-foot modelling element C6j								
	Bottomless C61	Add bottom C62	Nail foot C63					

3. Study Process

3.1. Specimen collection

In this paper, the purple-clay teapot is taken as the research object. Through literature review[11], field visits and other ways to investigate the classic shapes of the purple-clay teapot, about 64 kinds of the classic shapes of the purple-clay teapot have been obtained. The form of 64 kinds of classic purple-clay teapots was analyzed. Tmall purple purple-clay teapot were crawled with crawler tools and the front view of the classic purple-clay teapot was obtained through screening, which is convenient for product evaluation and feature extraction and induction in the later stage. In order to better exclude the influence of other factors, the background of the collected pictures of 64 kinds of classic purple-clay teapot was unified, as shown in Figure 2.

3.2. Analysis and extraction of modeling elements

After determining the classic modeling samples, 64 kinds of purple-clay teapot were decomposed. Focus group method was used to extract the modeling design elements of purple-clay teapot and subdivide its design categories. It is known that the purple-clay teapot can be divided into six morphological design elements, such as lid, body, spout, handle, knob and foot, and its morphological design elements can be subdivided into 30 design categories. The shape and form design elements of purple-clay teapot were digitally coded to ensure that each shape and form element and design category was significantly differentiated. Finally, the shape and form design feature coding matrix of purple-clay teapot was formed as shown in Table 1.

3.3. Sample selection

64 pictures of purple-clay teapot were coded. The formula takes X_n to represent the sample and C_{ij} to represent the design features, then the combination of the characteristic elements of the purple-clay teapot is:

$$X_1 = \{C_{15}, C_{21}, C_{32}, C_{41}, C_{52}, C_{61}\}$$

$$X_2 = \{C_{12}, C_{22}, C_{34}, C_{42}, C_{53}, C_{62}\}$$

.....

$$X_m = \{\dots, \dots, \dots, C_{ij}, \dots, \dots\}$$

.....

$$X_{64} = \{C_{14}, C_{25}, C_{30}, C_{43}, C_{51}, C_{61}\}$$

In order to better screen out the appropriate samples, through cluster analysis, samples that can meet all the characteristics of 31 modeling elements were selected from 64 classical purple sand pot models. A total of 12 samples were screened out. The modeling elements of these samples include all types of purple-clay teapot. Twelve samples were processed with gray level to exclude the influence of color on the perceptual image, as shown in Figure 3.



Figure 3. Screened samples

3.4. Collection of emotional image words

Tmall platform is a comprehensive shopping website^[12], and its sales categories are complete, most of which are in the form of flagship stores. Therefore, we selected the review data of purple-clay teapot in Tmall e-commerce platform as the research object, and grabbed the sales data of June 7, 2019 through Python program, on which 79,377 related products of purple-clay teapot were sold on Tmall platform. In order to better capture useful data, we only captured 18035 review data from the stores with the highest sales volume and review volume. The stores with the highest sales volume and review volume can reflect that these stores are more in line with users' needs.

3.5. Comment data preprocessing

Data directly obtained by web crawler usually have a lot of noise data, so it is necessary to preprocess the data. Due to the influence of word diversity, wrong words and network buzzwords, this paper adopts stuttering participle for word segmentation and part of speech tagging.

To extract adjectives, that is, after tagging the collected comments with part of speech, the adjectives described in the comments for purple clay pot are selected.

Inductive similar adjectives. Summarize the collected adjectives and delete those who do not conform to the actual situation, such as "cheap" and other adjectives that are not suitable for evaluating the shape. Similar adjectives such as "beautiful", "good-looking" and "beautiful" are classified by the same category.

Get image vocabulary. Make descending order of the inducted adjectives and select the top 30 adjectives. The purple-clay teapot was evaluated through focus groups using selected adjectives. The focus group consists of 20 design students (male 11, female 9). Each member is limited to 10 words from 30 words, which can be used to evaluate purple sand teapots. Finally, the top 5 descriptive words were summarized, as shown in Table 2. And the negative words are summarized, cute - serious, soft - masculine, boring - fun, light - bulky, fragility - firmness.

Table 2. Frequency table of image vocabulary pairs

Pair of image words	Number of times used
Cute - serious	18
Soft - masculine	17
Boring - fun	17
Light - bulky	15
Fragility - firmness	13

3.6. Establish the space of image meaning

Based on the selected samples and image vocabulary groups, the questionnaire was compiled to establish an image semantic space for the description of morphological elements of purple-clay teapot. Using SD method and combining 7-point Likert Scale to grade the shape of purple-clay teapot, a semantic axis of 1~7 was formed.

A total of 273 questionnaires were distributed, 269 were collected, and 260 were valid statistical data. The analysis of the results is shown in Table 3.

The statistical results are exported to SPSS statistical software for analysis, and the standard deviation of image word pairs is obtained, as shown in Table 4. As shown in

Figure 4, the semantic axes of the images of samples were drawn. From the descriptive statistical analysis and the combination of the semantic axes of the samples, it can be concluded that the image vocabulary group of "masculinity -- softness" can better analyze the semantic space of the samples.

Table 3. Mean value of image evaluation

Sample	Cute - serious	Soft - masculine	Boring - fun	Lightweight - bulky	Fragility - firmness	Sample	Cute - serious	Soft - masculine	Boring - fun	Lightweight - bulky	Fragility - firmness
	-0.73	-1.54	-0.19	0.23	1.03		0.27	0.15	-0.09	0.49	-0.08
	-0.63	-0.67	-0.41	0.95	0.79		-2.16	-1.83	1.49	-0.79	-0.39
	-0.19	-0.32	1.03	0.47	0.51		1.46	1.36	0.45	0.45	0.09
	2.25	2.46	-1.02	1.65	1.84		-0.59	-1.21	-0.55	0.41	0.13
	-1.26	-2.02	1.21	-0.86	0.09		-1.31	-1.23	1.49	-0.59	-0.81
	0.01	-0.26	-0.85	0.39	0.65		1.79	1.76	-0.19	1.43	1.58

Table 4. Statistical results

	Descriptive Statistics													
	N	Range	Minimum	Maximum	Sum	Mean		Std. Deviation	Variance	Skewness		Kurtosis		
						Statistic	Std. Error			Statistic	Std. Error			
Cute - serious	12	4.41	-2.16	2.25	-1.09	-0.090833333	0.385882417	1.336735905	1.786862879	0.477065707	0.637302005	-0.526223831	1.232246474	
Soft - masculine	12	4.48	-2.02	2.46	-3.35	-0.279166667	0.421782757	1.461098331	2.134808333	0.726727726	0.637302005	-0.578306962	1.232246474	
Boring - fun	12	2.51	-1.02	1.49	2.37	0.1975	0.261311161	0.905208414	0.819402273	0.32552934	0.637302005	-1.447423632	1.232246474	
Lightweight - bulky	12	2.51	-0.86	1.65	4.23	0.3525	0.229082905	0.793566461	0.629747727	-0.100176	0.637302005	-0.471337322	1.232246474	
Fragility - firmness	12	2.65	-0.81	1.84	5.43	0.4525	0.22428717	0.77695355	0.603656818	0.338034787	0.637302005	-0.306634471	1.232246474	

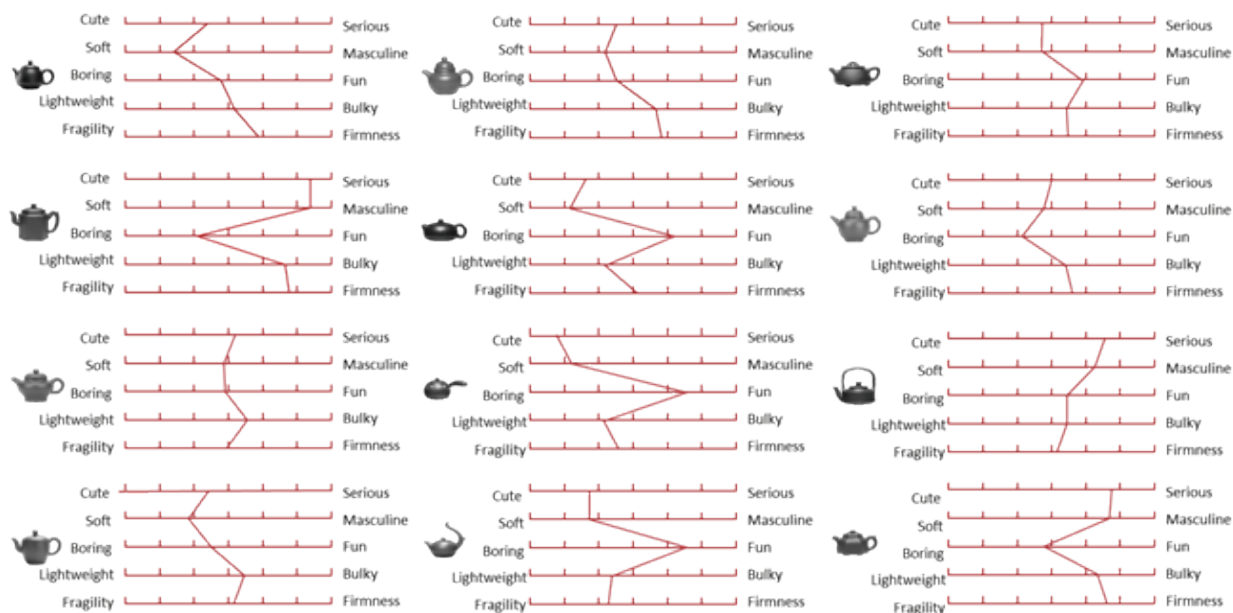


Figure 4. semantic axis of image

3.7. Construction of a theoretical model of quantification

After the statistical analysis of image words, the relationship between the modeling design elements and image words is described quantitatively by constructing a quantitative theoretical model. Here, the modeling and morphological elements of purple-clay teapot are taken as independent variables, and its perceptual image vocabulary evaluation value is taken as dependent variables, and the objective analysis is conducted by means of multiple regression. The formula is as follows :

$$Y_m = \sum_{i=1}^n \sum_{j=1}^{\eta} \delta_m(i, j) b_{ij} + \varepsilon_m$$

Where

$$\delta_m(i, j) = \begin{cases} 1 & \text{Insamplem, the qualitative factor for item is category j} \\ 0 & \text{Noorother} \end{cases}$$

$$Y_{\text{Soft-Masculine}} = \begin{cases} b_{11} \delta_m(1,1) \\ \vdots \\ b_{18} \delta_m(1,8) \end{cases} + \begin{cases} b_{21} \delta_m(2,1) \\ \vdots \\ b_{25} \delta_m(2,5) \end{cases} + \begin{cases} b_{31} \delta_m(3,1) \\ \vdots \\ b_{37} \delta_m(3,7) \end{cases} + \begin{cases} b_{41} \delta_m(4,1) \\ \vdots \\ b_{43} \delta_m(4,3) \end{cases} + \begin{cases} b_{51} \delta_m(5,1) \\ \vdots \\ b_{54} \delta_m(5,4) \end{cases} + \begin{cases} b_{61} \delta_m(6,1) \\ \vdots \\ b_{63} \delta_m(6,3) \end{cases} + \varepsilon_m$$

The value of masculinity - soft sensibility is analyzed.

4. Experimental Results and Analysis

Combined with the Quantification-I theory, the analysis of the Masculine - soft quantitative model is carried out, and the results are shown in Table 5.

According to the analysis of quantification-i theory^[13], the order of partial correlation coefficient is: Pot handle (0.553) > lid (0.311) > foot (0.23) > knob (0.125). This shows that in the perceptual evaluation of purple-clay teapot, the body has the greatest influence on "masculinity - soft", the spout and handle are the second, while the foot and knob have the least influence on "masculinity - soft". In a word, in the process of analyzing the scores of various morphological elements in the purple-clay teapot, the larger the positive value is, the greater the influence of the morphological elements on the image of "softness"; on the contrary, the lower the score is, the more masculine the image is.

Similarly, this method can quantitatively analyze the correspondence between other modeling elements and other perceptual image vocabulary groups.

5. Conclusion

With the development of network technology, more and more consumers carry out shopping through network. By collecting a large amount of comment data from e-commerce platforms for analysis, it can better provide data sources for design. By crawling online comment data, a large amount of data can be obtained and the part of speech and word frequency can be quickly analyzed, which is more efficient than the traditional collection of emotional words through books, advertisements, newspapers and other means. A large number of samples can be obtained by crawling the

e-commerce platform through the network crawler. The samples of the e-commerce platform are directly oriented to consumers, which is of great reference significance. In this paper, the purple-clay teapot was analyzed by combining Kansei Engineering and Quantification-I theory, which provides a new idea for product design research.

Table 5. Quantification-I theory analysis results

Design elements	Form elements	Category score	Partial correlation coefficient
Kettle body modelling element	Spherical C11	0.593	0.945
	Elliptical (vertical) C12	0.091	
	Elliptic (transverse) C13	0.213	
	Cylindrical C14	0.015	
	Cylindrical C15	-0.161	
	Inverted table C16	-0.015	
	Square platform C17	-0.203	
	Square C18	-0.352	
Kettle spit modelling element	Curved spit 1, C21	0.121	0.566
	Curved spit 2, C22	0.201	
	Curved spit 3, C23	0.462	
	Straight spit , C24	-0.104	
	Short straight spit , C25	0.321	
Kettle handle modelling element	Arc front ear handle C31	0.201	0.556
	Arc inverted ear handle C32	0.241	
	Handle with straight line C33	-0.218	
	Round ear handle C34	0.125	
	Handle C34	-0.103	
	Lifting beam handle C36	-0.315	
	Flying kettle handle C37	0.121	
Kettle cover modelling element	Nested cover pot C41	0.021	0.312
	Pressing cover pot C42	0.102	
	Cutting cover pot C43	0.333	
Kettle knob modelling element	Spherical C51	0.012	0.121
	Cylindrical C52	0.025	
	Bridge shape C53	-0.012	
	Ellipse C54	0.109	
	Transverse ellipse C55	0.033	
Kettle foot modelling element	Bottomless C61	0.319	0.21
	Add bottom C62	0.214	
	Nail foot C63	0.091	
Constant term			2.49

References

- [1] Mitsuo Nagamachi, Kansei engineering as a powerful consumer-oriented technology for product development. APPLIED ERGONOMICS. 33, 3(2002)
- [2] Yan Pu Yang, Deng Kai Chen, Rong Gu, Yu Feng Gu and Sui Huai Yu, Consumers' Kansei Needs Clustering Method for Product Emotional Design Based on Numerical Design Structure Matrix and Genetic Algorithms. Computational Intelligence & Neuroscience. 2016, (2016)
- [3] Alex Boulton, Testing the limits of data-driven learning: Language proficiency and training. ReCALL. 21, 1(2009)
- [4] L. I. Shaobo, Huafeng Quan, H. U. Jianjun, W. U. Yongming and Ansi Zhang, Perceptual evaluation method of

- products based on online reviews data driven. *Computer Integrated Manufacturing Systems*. (2018)
- [5] Marzieh Berenjkoub, Rodolfo Ostilla Monico, Robert S. Laramie and Guoning Chen, Visual Analysis of Spatio-temporal Relations of Pairwise Attributes in Unsteady Flow. (2019)
- [6] Jin Wang, L. U. Guo-Dong and Yun Long Zhang, Quantification-I theory based IGA and its application. *Journal of Zhejiang University*. (2013)
- [7] S. U. Ke and Shou Qian Sun, Product material image decision-making support model based on GEP. *Computer Integrated Manufacturing Systems*. 18, 2(2012)
- [8] B. Qi, S. Yu and W. He, Product cognitive style based on kansei engineering and visual track experiments. *Journal of Applied Sciences*. 13, 12(2013)
- [9] ZHANG Yufei BIAN Ze LUO Shijian, Status and Progress of Product Shape Bionic Design. *Journal of Mechanical Engineering*. 54, 21(2018)
- [10] Yan Pu Yang, A Method for Consensus Reaching in Product Kansei Evaluation Using Advanced Particle Swarm Optimization. *Computational Intelligence and Neuroscience*,2017,(2017-02-12). 2017, 2(2017)
- [11] Joyita Mallik, Ashok Samal and Scott L. Gardner, A content based image retrieval system for a biological specimen collection. *Computer Vision & Image Understanding*. 114, 7(2010)
- [12] Yan-pu Yang and Xing Tian, Combining users' cognition noise with interactive genetic algorithms and trapezoidal fuzzy numbers for product color design. *Computational Intelligence and Neuroscience*. 2019, (2019)

Biomass Straw Based Activated Porous Carbon Materials for High-Performance Supercapacitors

Mengdie GUAN, Xinle ZHANG, Yingping WU, Qihao SUN, Dongqi DONG, Xiaoling ZHANG, Jie WANG*

College of Chemistry and Pharmaceutical Sciences, Qingdao Agricultural University, Qingdao, China

*Corresponding Author: Jie WANG, Changcheng Road 700#, Chengyang District, Qingdao, 266109, China; wangjie@qau.edu.cn

Abstract:

Biomass straws are often regarded as agricultural waste, usually burned off in rural areas, which results in severe resource waste and air pollution. In this work, biomass-based porous carbon material with a lamellar microstructure is obtained via simple hydrothermal and subsequent KOH activation, the optimum activate process is determined by the proportion of activator. Scanning electron microscopy (SEM) and nitrogen adsorption techniques are conducted to investigate the physical properties of the materials. Cyclic voltammetry and constant current discharge/charge in the three-electrode system and symmetrical double-layer capacitors results indicate the best electrochemical performance of SCA-1.5 electrode material, with a capacity of 250.0 F g⁻¹ at 1.0 A g⁻¹. And notably, high recycling stability at a high cycling rate of 1.0 A g⁻¹ after 18,000 cycles.

Keywords: straw; biomass carbon; activation; porous lamellar structure; supercapacitor.

1. Introduction

The continuous consumption of fossil fuels has caused severe globally environmental pollution and resource depletion. Thus, research and development of renewable energy has attracted world-wide attention [1-4]. Many clean energy resources such as solar energy, tidal energy, wind energy are readily available and inexhaustible. Still, they possess low conversion efficiency, unbalanced power output, and hard to move and storage, which limited their applications in vehicles, portable devices, and other areas dramatically. Therefore, developing clean energy storage devices is of vital importance to potentially solve the problems. Feature of high energy density and fast discharge/charge rate, supercapacitors, has attracted worldwide attention [7-14]. The carbon-based supercapacitors also can be called the double electric layer capacitor. Such a device is potentially applied in energy storage devices because the capacity is significantly higher than traditional capacitors, and the output voltage is more stable than pseudocapacitors [15, 16]. The mechanism of electric double-layer capacitors is mostly based on the Herm Holtz principle [17-19]. An ideal capacitor material often needs a specific surface area as large as possible to serve a high capacity and conductivity, such as carbon nanotubes, graphene, carbon-based aerogels, etc.

In the industrial producing process, the cost of raw materials is an essential point for practical application. The raw materials from carbon nanotubes, graphene, carbon-based aerogels are not economically friendly, which limited the mass production of the related products [20, 21]. This project selected agricultural wastes (biomass straw) as raw materials, produced high capacity and stability carbon-based electrode materials via simple hydrothermal and subsequent KOH activation method. Such a template-free and the surfactant-free process are potentially applicable for industrial constructing.

2. Experimental Section

2.1. Materials synthesis

Selected the air-dried bio-straw, separated the skin and transferred the core into a 100 mL Teflon-lined stainless steel autoclave, raised the temperature to 200 °C and kept for 2 h. After cooled down to room temperature, the pre-carbonized materials were divided into five parts (2 g per part, approximately), added into solid KOH with the proportion by mass in 1:0.0, 1:0.5, 1:1.0, 1:1.5, 1:2.0, respectively. Then mixed in agate mortars thoroughly, transfer the mixture into the tubular furnace at a heating rate of 5 °C min⁻¹ to 900 °C in nitrogen atmosphere and

kept 2 h for activation. Cleaned the activated materials to neutral with deionized water and dried with air-dried oven to obtain the bio-straw-based carbon material. According to the proportion of activator, the five parts of materials are denoted as SCA-0, SCA-0.5, SCA-1.0, SCA-1.5, SCA-2.0, respectively.

2.2. Physical characterization

The micromorphology of the material was characterized by SEM (JSM-7500f), and the specific surface area and pore diameter of the materials were detected by the surface area analyzer (NOVA 2200e).

2.3. Electrochemical Measurements

The capacitors were assembled by using active materials, carbon black and PVDF at a proportion of 8:1:1 (respectively, by mass), respectively. Mixed and separated those materials in agate mortars, then applied in nickel foams and dried the nickel foam in a bake oven at 80°C for 2h. Cyclic voltammogram (CV) and discharge/charge measurements via a three-electrode system by electrochemical workstation were conducted to investigate the electrode activity. In the three-electrode system, saturated calomel electrode (SCE), carbon rod electrode, and 3 M KOH solution were served as reference electrode, counter electrode, and electrolyte, respectively.

3. Results and discussion

3.1. Structure and morphology analysis

Figure 1 presents the SEM image of SCA-0 and SCA-1.5. Without KOH activation, the smooth lamellar structure of SCA-0 (Figure 1a-b) can provide a large specific surface area. After KOH activated, the smooth surface turns rough, which indicates the active region was enlarged, the porous microstructure (Figure 1c-d) makes the electrolyte access into the pores easier. According to the discussion above, the KOH activator does not change the micromorphology of the materials significantly; thus, the activation process will not cast down the electrochemical stability as well.

Figure 2 exhibits the nitrogen adsorption-desorption curves (BET) of materials with different activator proportions. All four materials have hysteresis rings in the range of $P/P_0=0.5\sim 0.8$. Among them, SCA-1.5 is the most obvious, indicates the material has an excellent mesoporous structure. Table 1 shows the specific surface area and pore size distribution of the four materials from the BET test, in which SCA-1.5 has the highest specific surface area (177.0 $\text{m}^2 \text{g}^{-1}$), much higher than the other three materials. The relative lower specific surface area of SCA-0.5 and SCA-1.0 may be attributed to insufficient KOH activator. SCA-2.0 loses the original structure, perhaps attributed to the excessive KOH activator caused over-activation. From the pore size distribution, the average pore size of SCA-1.5 is 3.1 nm, which is smaller than the other three materials. It indicates that the KOH activator constructed micro-holes successfully in the lamellar carbon materials, which is consistent with the conclusion of SEM analysis. The detailed KOH activation mechanism is as follows^[22, 23]:

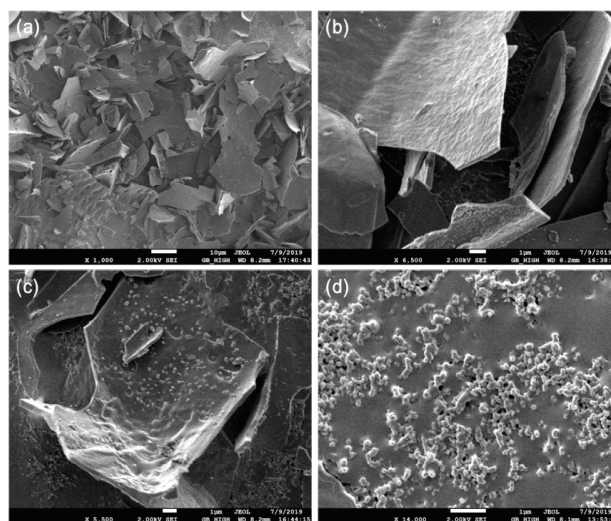
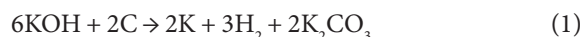


Figure 1 (a-b) SEM images of SCA-0 with step-by-step magnify; (c) SEM image of SCA-1.5 and the magnification image.

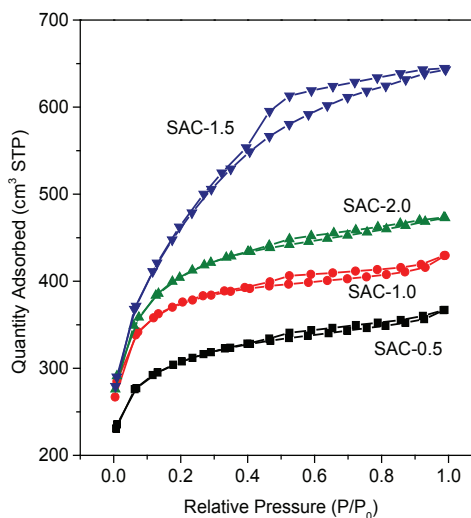


Figure 2 The N_2 desorption curves of the four activated materials.

Table 1 Surface area and pore size distribution of the four different active materials.

Samples	S ($\text{m}^2 \text{g}^{-1}$)	Pore Size (nm)
SCA-0.5	33.7	3.5
SCA-1.0	44.0	3.5
SCA-1.5	177.0	3.1
SCA-2.0	73.3	3.5

3.2. Electrochemical Performance

Figure 3a exhibits the CV curves of each activated electrode material in a 3 M KOH solution with a scanning rate at 50 mV s^{-1} . The electrode of SCA-1.5 material has the largest double electric layer capacity, and the CV curves exhibit a rectangular shape in the voltage of -1.0 - 0.2 V , which is close to the shape of ideal double electric layer capacitors. In comparison, the electrode of SCA-0 material has a lower double layer capacity in the potential range of -0.4 - 0.2 V , indicating that the activation process significantly enlarged the materials' surface area. The electrode of SCA-0, SCA-0.5, SCA-1.0, SCA-1.5 and SCA-2.0 materials contains 36.0 , 100.2 , 128.4 , 141.0 and 83.8 F g^{-1} , respectively (Figure 3b). Therefore, the electrode of SCA-1.5 material has the optimal activator proportion for the biomass carbon-based materials. The CV curves with different scanning rates were exhibited in Figure 3c. When the scanning rate above 200 mV s^{-1} , the material almost remains a regular rectangular shape, which indicates the material has a good rate capability. The capacitance line chart (Figure 3d) processed from the CV curve showed that with the scanning rate increases, the capacitance of SCA-1.5 material decreased significantly but remains 120.0 F g^{-1} at a scan rate of 200 mV s^{-1} , primarily

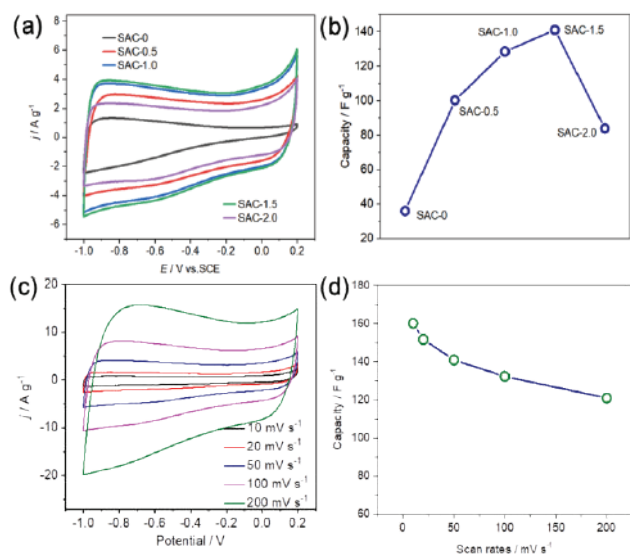


Figure 3 (a) CV curves of different activated materials, scan rate at 50 mV s^{-1} and the corresponding line chart of capacity (b); (c) CV curves of SAC-1.5 material at different scan rates and the corresponding line chart of capacity (d)

4. Conclusions

This project adopted the hydrothermal method-KOH activation process, for a biomass-based carbon material with a lamellar porous microstructure. The optimized activation process was conducted by adjusts the activator proportion. SCA-1.5 has the best electrochemical performance, the specific capacitance at 250.0 F g^{-1} , with

indicates the excellent capacitance performance.

Figure 4a exhibits the discharge/charge performance of four electrode materials with different activator proportions. SAC-1.5 has the best discharge duration with a 1.2 V potential window. The corresponding line chart of capacity (Figure 4b) demonstrates that SAC-1.5 material possesses a capacity of 311 F g^{-1} , which is much higher than SAC-0.5 (212 F g^{-1}), SAC-1.0 (247 F g^{-1}) and SAC-2.0 (183 F g^{-1}) and consistent with the CV curve analysis.

Considering the electrochemical behavior is often different from the ideal conditions, we assembled a symmetrical double-layer capacitor based on SAC-1.5 material and tested the electrochemical performance. Figure 4c exhibits the initial capacitance of the capacitor is 65 F g^{-1} at the discharge/charge rate of 1 A g^{-1} . After 2000 cycles activation, the capacity increased to 77 F g^{-1} . After 18000 cycles, the capacity remains stable, indicates that the SCA-1.5 based double-layer capacitor possesses excellent discharge/charge stability. Besides, this biomass-based supercapacitor lighted up a 2.2 V LED series, which combined with 28 bulbs successfully, proves the bio-straw based carbon materials are potentially applicable in the energy storage devices.

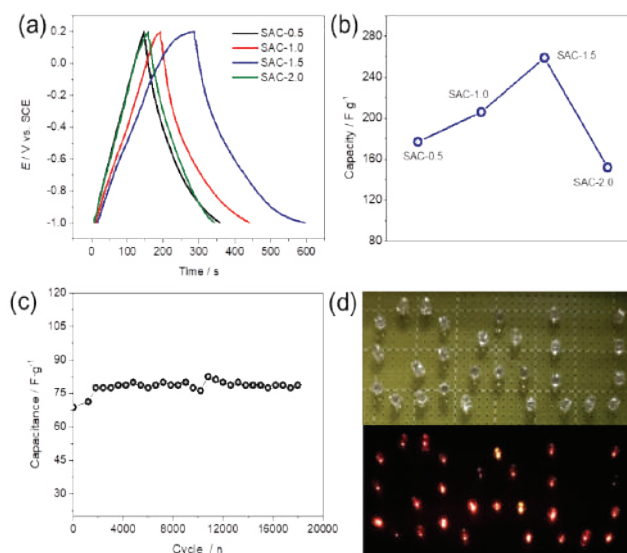


Figure 4 (a) Discharge/charge curves of different activated materials at current density of 1 A g^{-1} and the corresponding line chart of capacity (b); (c) Discharge/charge curves of SAC-1.5 based supercapacitor device at 1 A g^{-1} ; (d) Lighting LED series powered by SAC-1.5 based supercapacitor device.

the current density at 1.0 A g^{-1} . Besides, such electrode remained stable even after 18000 cycles at a high cycling rate of 1.0 A g^{-1} . The raw material of this project is cheap and easy to access, which potentially applied in the energy storage devices and for mass production. With an excellent electrochemical activity and stability, proves that the bio-straw based supercapacitors have a promising prospective application.

Author Contributions: J.W. conceived and designed the experiments. M.G., X.Z., Y.W. Q.S. and D.D. performed the materials synthesis. M.G. performed the electrochemical characterizations. J.W., X.Z. and D.D. wrote the manuscript. All authors discussed the results and commented on the manuscript.

Conflict of Interest: The authors declare that there is no conflict of interest regarding the publication of this paper.

Acknowledgments: This work was supported by the Research Foundation for Distinguished Scholars of Qingdao Agricultural University (665-1119008). The authors thank the Central Laboratory of Qingdao Agriculture University for the physical characterization.

References

- [1] Dhillon, R.; Wuehlisch, G. Mitigation of global warming through renewable biomass. *Biomass Bioener.* 2013, 48, 75-89.
- [2] Burke, A. Ultracapacitors: why, how, and where is the technology. *J. Power Sources*, 2000, 91, 37-50.
- [3] Xue, J. T.; Wu, Y.; Dai, Y.; Xia, Y. Electrospinning and Electrospun Nanofibers: Methods, Materials, and Applications. *Chem. Rev.*, 2019, 119, 5298-5415.
- [4] Yang, H.; Liu, S.; Cao, L.; Jiang, S.; Hou, H. Superlithiation of non-conductive polyimide toward high-performance lithium-ion batteries. *J. Mater. Chem. A*, 2018, 6, 21216-21224.
- [5] Vix-Guterl, C.; Frackowiak, E.; Jurewicz, K.; Friebe, M.; Parmentier, J.; Béguin, F. Electrochemical energy storage in ordered porous carbon materials. *Carbon*, 2005, 43, 1293-1302.
- [6] Liu, C.; Li, F.; Ma, L. P.; Cheng, H. M. Advanced Materials for Energy Storage. *Adv. Mater.*, 2010, 22, E28-E62.
- [7] Gu, W.; Yushin, G. Review of nanostructured carbon materials for electrochemical capacitor applications: advantages and limitations of activated carbon, carbide-derived carbon, zeolite-templated carbon, carbon aerogels, carbon nanotubes, onion-like carbon, and graphene. *WIREs Energy Environ.* 2014, 3, 424-473.
- [8] Zhang, L.L.; Zhao X. Carbon-based materials as supercapacitor electrodes. *Chem. Soc. Rev.* 2009, 38, 2520-2531.
- [9] Wang, W.; Shi, Y.; Su, Y.; Wang, Y.; Sun, H. Construction of MnO₂ Nanowire for a High-Performance Lithium Ion Supercapacitor. *Research and Application of Materials Science* 2019, 1, 18-23.
- [10] Xu, W., Ding, Y., Yu, Y., Jiang, S., Chen, L., & Hou, H. Highly foldable PANi@ CNTs/PU dielectric composites toward thin-film capacitor application. *Mater. Lett.*, 2017, 192, 25-28.
- [11] Wang, X.; Lu, X.; Liu, B.; Chen, D.; Tong, Y.; Shen, G. Flexible energy-storage devices: design consideration and recent progress. *Adv. Mater.*, 2014, 26, 4763-4782.
- [12] Zhang, Q.; Uchaker, E.; Candelaria, S. L.; Cao, G. Nanomaterials for energy conversion and storage. *Chem. Soc. Rev.*, 2013, 42, 3127-3171.
- [13] Mao, X.; Hatton, T. A.; Rutledge, G. C. A review of electrospun carbon fibers as electrode materials for energy storage. *Curr. Org. Chem.*, 2013, 17, 1390-1401.
- [14] Dai, L.; Chang, D. W.; Baek, J. B.; Lu, W. Carbon nanomaterials for advanced energy conversion and storage. *Small* 2012, 8, 1130-1166.
- [15] Ogoshi, T.; Sueto, R.; Yoshikoshi, K.; Sakata, Y.; Akine, S.; Yamagishi, T. A. Host-guest complexation of perethylated pillar [5] arene with alkanes in the crystal state. *Angew. Chem. Int. Ed.* 2015, 54, 9849-9852.
- [16] Hulicova-Jurcakova, D.; Seredych, M.; Lu, G. Q.; Kодиweera, N. K. A. C.; Stallworth, P. E.; Greenbaum, S.; Bandosz, T. J. Effect of surface phosphorus functionalities of activated carbons containing oxygen and nitrogen on electrochemical capacitance. *Carbon*, 2009, 47, 1576-1584.
- [17] Ma, H.; Zhou, Q.; Wu, M.; Zhang, M.; Yao, B.; Gao, T.; ... Shi, G. Tailoring the oxygenated groups of graphene hydrogels for high-performance supercapacitors with large areal mass loadings. *J. Mater. Chem. A* 2018, 6, 6587-6594.
- [18] He, S.; Chen, W. 3D graphene nanomaterials for binder-free supercapacitors: scientific design for enhanced performance. *Nanoscale* 2015, 7, 6957-6990.
- [19] H. Jing-quan, L. Kai-yue, Y. Yi-ying, et al. Synthesis and electrochemical performance of flexible cellulose nanofiber-carbon nanotube/natural rubber composite elastomers as supercapacitor electrodes[J]. *New Carbon Mater.* 2018, 33, 341-350.
- [20] Farma, R.; Deraman, M.; Awitdrus, A.; Talib, I. A.; Taer, E.; Basri, N. H.; ... Hashmi, S. A. Preparation of highly porous binderless activated carbon electrodes from fibres of oil palm empty fruit bunches for application in supercapacitors. *Bioresource Technol.* 2013, 132, 254-261.
- [21] Inagaki, M.; Kim, Y.A.; Endo, M. Graphene: preparation and structural perfection. *J. Mater. Chem.* 2011, 21, 3280-3294.
- [22] Wang, J.; Kaskel, S. KOH activation of carbon-based materials for energy storage. *J. Mater. Chem.*, 2012, 22, 23710-23725.
- [23] Bhattacharjya, D.; Yu, J. Activated carbon made from cow dung as electrode material for electrochemical double layer capacitor. *J. Power Sources*, 2014, 262, 224-231.

Effect of Heat Treatment on Microstructure and Mechanical properties of high strength low alloy (HSLA) steel

Siyuan ZHAO¹, Kaixuan CHEN¹, Yaliku•WUQIKUN¹, Xiaohua CHEN^{2*}, Zidong WANG^{1*}

1 School of Science and Engineering, University of Science and Technology Beijing, Beijing, China

2 State Key Laboratory for Advanced Metals and Materials, University of Science and Technology Beijing, Beijing, China

***Corresponding Author:** Xiaohua CHEN, State Key Laboratory for Advanced Metals and Materials, University of Science and Technology Beijing, Beijing, 100083, China, chenxh@skl.ustb.edu.cn; Zidong WANG, School of Science and Engineering, University of Science and Technology Beijing, Beijing, 100083, China, wangzd@mater.ustb.edu.cn

Abstract:

In this paper, a Fe-based Mn-Ni-Cr-Mo high strength low alloy (HSLA) steel was prepared by using Vacuum melting, following by hot rolling with 78% deformation and various heat treatment processes. Microstructure were characterized by optical microscope (OM), scanning electron microscope (SEM) equipped with energy dispersive spectrometer. Tensile tests were performed. After direct quenching (Q) from 860°C, the samples were subjected to secondary quenching (L) at different intercritical temperatures within the two-phase region and various tempering temperatures (T). Results show that QLT treatment increases elongation and decreases yield ratio compared with conventional quenching and tempering process (QT). The optimum QLT heat treatment parameter in terms of temperature are determined as Q: 860°C, L: 700°C, and T: 600°C, resulting in the better combined properties with yield strength of 756MPa, tensile strength of 820MPa, tensile elongation of 16.76% and yield ratio of 0.923.

Keywords: high strength low alloy (HSLA) steel; QLT heat treatment; tempering; microstructures; mechanical properties

1. Introduction

In order to meet the development of large-scale, high-speed and multi-sea operations of high strength low alloy (HSLA) steel, a steel system with high strength, high toughness and good weldability to allow reliable operation must be assured for extreme severe environments and service conditions^[1]. This indicate an increasing requirement for HSLA steel. In the decades, researchers have done a lot of works in the field of HSLA steel, for example, widely-used high yield (HY) series high-strength steel in the United States, Japanese NS series steel, and Russian Ab-series steel^[2-8]. Above mentioned traditional HSLA steels are based on low-carbon and low-alloys^[9,10], and their high strength and high toughness is attained based on the low-carbon tempered martensite structure obtained through the “quenching and tempering” heat treatment process. The high strength of steel required higher alloy element content, which simultaneously results enhanced in carbon equivalent and thus the deteriorating welding performance. Therefore, how to balance strength, toughness and welding performance of steel has become a key factor in the development of high strength steel.

New ideas have been provided to achieve strength-toughness-welding performance balance. The United States first proposed a new generation of copper-containing easy-welded high strength submarine steel plan to develop the same strength and toughness index as HY 80 steel^[11,12], with better weldability in comparison with HSLA 80 structural steel. HSLA 80^[13] is a low-carbon, copper-precipitated reinforced steel. The ϵ -Cu precipitation and ultra-fine bainite structure with high density dislocation in the steel yield excellent comprehensive mechanical properties. Through dispersion strengthening of ϵ -Cu phase formed in the aging process, the strength loss caused by C is compensated, and the welding crack sensitivity is reduced^[14].

At present, high strength steel systems of 390MPa, 440MPa, 590MPa and 785MPa have been formed^[15], which all use the Mn-Ni-Cr-Mo component system mostly treated with quenching and tempering. The Mn-Ni-Cr-Mo component system treated with quenching and tempering can meet the requirements of technical indicators, but also has some shortcomings. First of all, after heat treatment of quenching and tempering process

[16-18], yield ratio is relatively high, generally up to 0.93 or more, sometimes even as high as about 0.97, which greatly reduces the safe using performance. Secondly, tempering temperature range is narrower during the quenching and tempering process, which increases the difficulty of industrial production. In this paper, we employed a special heat treatment procedure, named QLT treatment [19] which consists of direct quenching (Q), relatively low temperature (intercritical) quenching (L) and tempering (T) to improve the mechanical properties and modify the microstructure of HSLA steel, respectively [20]. The microstructure is refined and ferrite is introduced on the basis of the strengthened phase (tempered martensite) during this heat treatment process. Recently, it has been recognized that the multi-phase microstructure which consists of “soft” ferrite/pearlite and “hard” bainite/martensite would improve the impact property of the steel [21,22]. The combination of soft ferrite and relatively hard secondary tempering martensite reduces the yield ratio and improves elongation. In this paper, a low carbon alloy steel containing alloying elements Ni, Cr, Mo, etc. in hot-rolled state was experienced QT and QLT treatments in sequence. The effects of conventional quenching and tempering heat treatment process (QT) and two-phase zone secondary quenching heat treatment process (QLT) on the microstructure and mechanical properties of the steel were investigated and compared. The results show that QLT heat treatment process improves the elongation and reduces yield ratio obviously.

2. Experimental Procedures

2.1. Preparation of samples

The steel sample with chemical compositions (see Table 1) similar to Mn-Ni-Cr-Mo HSLA steel was prepared. Steel ingot of 150 mm length, 70 mm width and 80 mm thickness was obtained by melting the mixture of all base metals in a corundum crucible in a vacuum furnace [23]. Before melting, degreasing, rust removal and drying treatment

were applied to reduce the introduced inclusions and gas. Vacuum deaeration was adopted and the system vacuum degree is 6×10^{-4} Pa. Oxygen level was controlled in a reasonable range of 40–60 ppm in the melt and nitrogen level in a range of 10–20 ppm. Finally, the melt was poured and cooled down inside the crucible in air. Fabrication process has been presented in detail in our former paper [24].

Then, as-cast ingots were heated at 1200 °C for 2 h and subjected to hot-rolling into 18 mm thick plates with a total cumulative reduction of 78% given in five passes, followed by air cooling to room temperature. By using far-infrared instrument, initial and final rolling temperatures were measured to be 1150 ± 10 °C and 850 ± 10 °C, respectively. Hot-rolled sample of 510 mm length, 105 mm width and 18 mm thickness was then cut into blocks by wire cut electrical discharge machining (WEDM). The sample after hot rolling is divided into two groups named I and II. Group I blocks of rolled-steel with size of 110 mm length, 30 mm width and 10 mm thickness were kept at 880 °C, 860 °C and 840 °C for 1 h quenched in water and subsequently tempered at temperatures of 600 °C for 1h. Group II are after direct quenching from 860 °C, the samples were subjected to secondary quenching (L) at different intercritical temperatures within the two-phase region and various tempering temperatures (T). The QLT treatment includes two step quenching and tempering. Table 2 illustrates the treatment processes used in this paper. The QLT process adds a two-phase zone quenching process between the QT processes. The measured AC1 temperature is 706 °C, and the AC3 temperature is 767 °C. For the QLT processing here, the selected heated temperature is set between 680 °C -760 °C, which is actually high tempering temperature. But the water quenching is chosen as the cooling method, instead of air cooling or furnace cooling. So we called this special processing as a kind of secondary quenching. Therefore, the secondary quenching temperature range is 680-760 °C.

Table 1. Actual chemical compositions of steels (wt.%).

Composition	C	Si	Mn	P	S	Cr	Ni	Cu	Mo	V	Nb	Al
Content	0.06	0.04	1.03	0.02	0.02	0.97	4.66	0.02	0.54	0.003	0.05	0.002

Table 2. The treatment processes of steel.

Name	1	2	3	4	5	6	7	8
Primary quenching temperature	860 °C ×1h							
Secondary quenching temperature	760 °C ×1h	730 °C ×1h	700 °C ×1h	680 °C ×1h	700 °C ×1h	700 °C ×1h	700 °C ×1h	700 °C ×1h
Tempering temperature	600 °C ×1h	600 °C ×1h	600 °C ×1h	600 °C ×1h	640 °C ×1h	620 °C ×1h	600 °C ×1h	580 °C ×1h

2.2. Material characterization and mechanical property test

Optical microscopy (OM), scanning electron microscopy (SEM), equipped with energy dispersive spectrometer

were performed to characterize the microstructures. The spot resolution for the energy dispersive spectrometer (EDS) analysis is 0.205 nm. Metallographic specimens were ground with silicon carbide paper and subsequently polished followed by etching with 4% alcohol nitric acid

solution. Tensile test specimens were cut from hot-rolled samples and tempered samples with WEDM, respectively. Tensile tests were conducted on dog-bone shaped specimens with a gage size of 30mm length, 12.5mm width and 2mm thickness at room temperature with a strain rate of 10–3s–1 using an FPZ 100 machine. The hardness test is conducted on the WHR-80D total Rockwell Hardness tester. The hardness of the experimental steel in rolled and heat-treated state is measured according to the GB/T 2850-1992. 6 points were measured at different positions on the metallographic samples with 10mm×10mm×10mm, and then the average value was obtained as the hardness for the tested samples.

3. Results and Discussion

3.1. Effect of QT process on microstructure and mechanical properties

Figure 1 and Figure 2 show the optical microscope images and scanning electron micrographs of the microstructure at different quenching temperatures. The steel in QT state exhibited a tempered troostite structure in temper state, with quenching at 840°C, 860°C, 880°C and tempering at 600°C. Most of the martensite structure in the troostite structure remained in slat-like shape as shown in SEM images of these QT steels. Numerous carbides were precipitated between martensite slats and at grain boundaries of original austenite. The tempering stability is improved due to the presence of strong carbide forming elements such as Mo, V, Nb, etc. Therefore, most of tempering microstructure

maintains the form of slat, accompanied with high strength.

Quenching temperature influences directly the grain size of austenite structure and correspondingly affects the distribution of quenching structure, leading to the variation of tempering structure (see Fig. 2). Specifically, the higher quenching temperature, the coarser structure in austenitizing (austenite grain), quenching (lath martensite) and tempering (tempering troostite) states. The final tempering structure causes the difference in mechanical properties (see Table 3). On the other hand, the experimental steel contains alloying elements including Ni, V, Cr, and Mo. As the quenching temperature increases, the solid solution contents of the alloying elements increase in the quenching state, which facilitate the precipitation of carbides and nitrides during tempering process. This makes a great contribution on the improvement of strength. The mechanical testing results in Table 3 demonstrate that increase of quenching temperature has the greatest impact on the decline of the yield and tensile strengths of steel. With quenching temperature increasing, specifically, tensile strength decreased from 1055MPa to 908MPa, and yield strength decreased from 882MPa to 878MPa. Tensile elongation and yield ratio at different QT states exhibit similar values around 13% and 0.96, respectively. Therefore, considering several mechanical properties parameters, we conclude that the steel quenched at 860°C and tempered at 600°C obtain the optimized comprehensive mechanical properties, with the yield strength of 881MPa, tensile strength of 909MPa, elongation after fracture of 13.92 %, and yield ratio of 0.969.

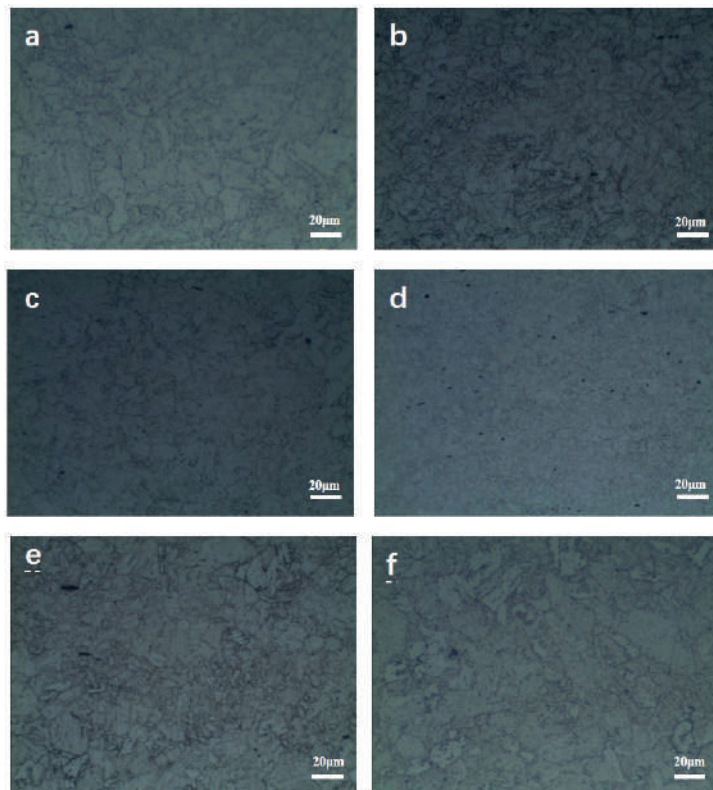


Figure 1. Low magnification optical micrographs of tempered samples at different quenching temperature. Quenching temperature: (a) 840°C; (b) 840°C; (c) 860°C; (d) 860°C; (e) 880°C; (f) 880°C. Tempering temperature: 600°C.

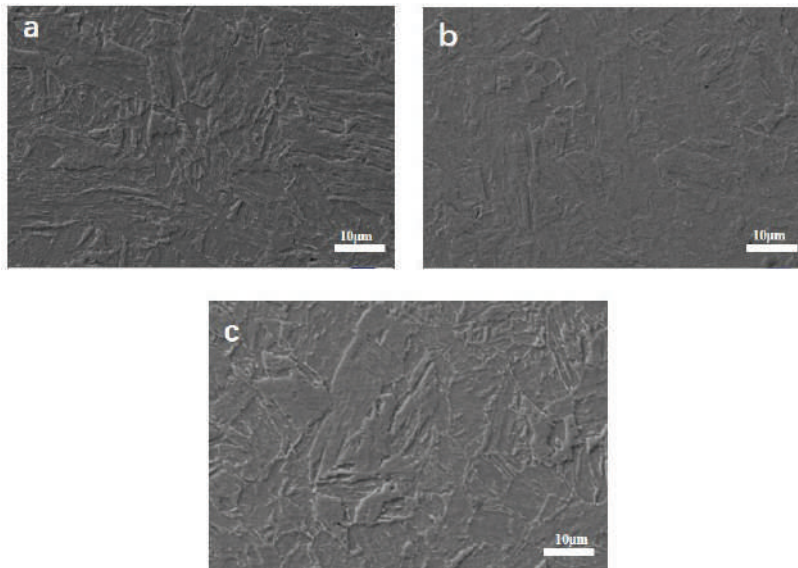


Figure 2. SEM images of at different quenching for 1h and tempering at 600°C, (a) 840°C; (b) 860°C; (c) 880°C

Table 3. Mechanical performance of QT state steel

number	quenching (°C)	temper (°C)	Yield Strength (MPa)	tensile strength (MPa)	Elongation (%)	hardness (HR)	Yield ratio
A	Rolled state	600	0	1055.514	12.16	29.7	0
B	880	600	878.813	908.8632	13.6	28.7	0.967
C	860	600	881.063	909.2028	13.92	26.9	0.969
D	840	600	882.121	910.853	13.84	27.3	0.968

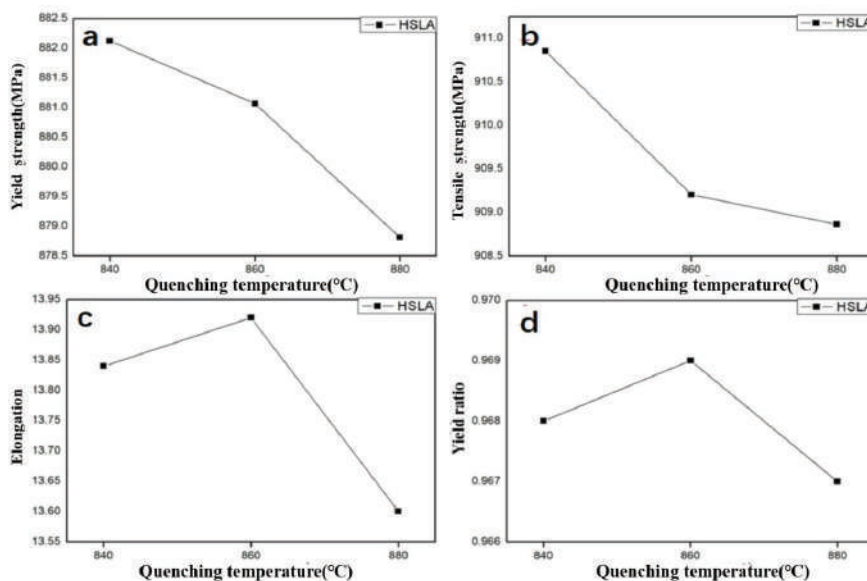


Figure 3. Evolution of mechanical properties with different quenching temperatures: (a) Yield strength; (b) Tensile strength; (c) Elongation; (d) Yield ratio

3.2. Effect of QLT process on microstructure and mechanical properties

In the previous stage, the effects of different quenching temperatures on the microstructure and properties of

steel were investigated. The optimum QT heat treatment parameter in terms of temperature are determined as Q: 860°C and L: 600°C, resulting in the better combined properties with yield strength of 881MPa, tensile strength

of 909MPa, tensile elongation of 13.92% and yield ratio of 0.969. The secondary quenching process was conducted to further verify the relevant properties of the experimental steel.

The secondary quenching produces the continuous distribution of the mixed structure of the secondary tempered martensite and ferrite, similar as the dual-phase steel structure. The combination of the soft ferrite and the hard secondary tempered martensite has the greatest impact on the decline of the yield ratio and the increase of the elongation. Table 4 gives detailed parameters of mechanical properties under different secondary quenching processes (i.e. QLT states). With the secondary quenching temperature increasing, specifically, tensile strength increased from 802 MPa to 912MPa, and yield strength increased from 740MPa to 887MPa. At different QLT states, tensile elongation exhibit similar values around 16%, and yield ratio is higher than 0.89.

Considering the mechanical properties in Table 4, processed in sequence by the quenching at 860°C, secondary quenching at 680-760°C and tempering at 600°C, the steel under 700°C secondary quenching obtain

the optimized comprehensive mechanical properties, with the yield strength of 756MPa, tensile strength of 820MPa, elongation after fracture of 16.96 %, and yield ratio of 0.923.

Then under the constant secondary quenching temperature of 700°C, tempering processes at 580°C, 600°C, 620°C, 640°C for 1 h were carried out to determine the best tempering temperature for the steel. After the secondary quenching and high temperature tempering (>500°C), the obtained microstructure displayed a ferrite+ secondary tempered martensite. When residual austenite is present in the quenched steel, it can even be transformed into pearlite or bainite during tempering and then martensitic transformation occurs. The austenite does not decompose in the tempering heat preservation. In the subsequent cooling, due to the catalysis (anti-stabilization) effect, it is likely to undergo martensitic transformation. This phenomenon is called secondary quenching. Then the structure obtained when tempering is secondary tempered martensite. As the tempering temperature increases, the ferrite content increases and the distribution areas becomes wider (see Fig. 4).

Table 4. Mechanical performance of QLT state steel

Secondary quenching temperature (°C)	Temper temperature (°C)	Yield Strength (MPa)	tensile strength (MPa)	Elongation (%)	Yield ratio
760	600	887.212	912.152	15.20	0.972
730	600	861.354	907.652	16.40	0.949
700	600	756.862	820.498	16.96	0.923
680	600	740.251	802.513	17.20	0.893

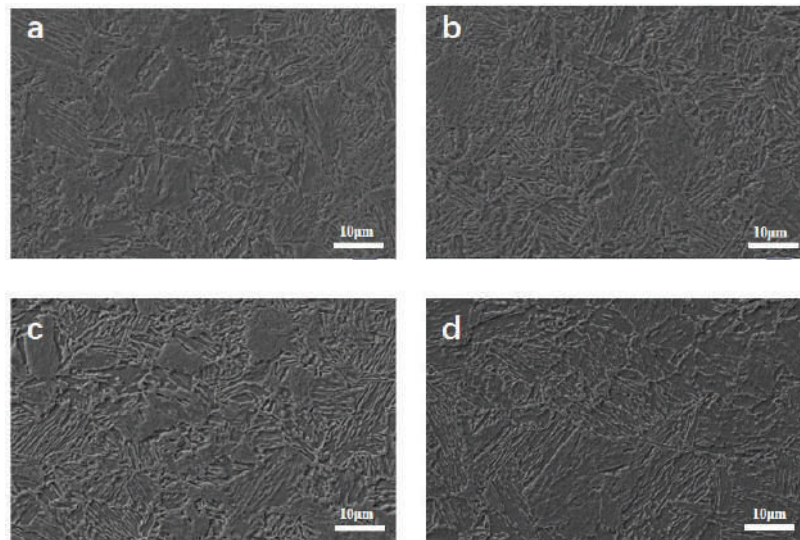


Figure 4. SEM images of at Secondary quenching 700°C for 1h and different tempering (a) 580°C; (b) 600°C, (c) 620°C, (d) 640°C

With the temper temperature increasing, specifically, tensile strength decreased from 846MPa to 787MPa, and yield strength decreased from 785MPa to 700MPa. At different QLT states, tensile elongation decreased

first and then rose, between 16.96-19.60, and yield ratio exhibited similar values around 0.93 (in Table 5 and Fig. 5). Considering the mechanical properties processed in sequence by the quenching at 860°C, secondary quenching

at 700 °C and tempering at 580-640 °C, the steel tempering at 600 °C obtained the optimized comprehensive mechanical properties.

The tensile fracture surfaces of the experimental steel after the QT and QLT process are shown in Figs. 6 and 7. The number density and depth of dimples in fracture surface of steel sample quenching at 840 are less and smaller than those at 860 °C, respectively. Besides, the number density

and depth of dimples in fracture surface of steel sample tempered at 580 °C are less and smaller than those at 600 °C, respectively. The toughness of steel sample quenching at 860 °C (during QT process) and tempered at 600 °C (during QLT process) respectively present higher values compared to their counterparts, which is consistent with the previous reports that dense and deep dimples during tensile fracture induce higher toughness [26,27].

Table 5. Mechanical properties of QLT Process steel

	Secondary quenching temperature (°C)	Temper temperature (°C)	Yield Strength (MPa)	tensile strength (MPa)	Elongation (%)	hardness (HR)	Yield ratio
1	700	640	700.43	787.020	19.60	22.2	0.890
2	700	620	765.16	814.232	19.28	23.4	0.940
3	700	600	756.86	820.498	16.96	23.1	0.923
4	700	580	785.10	846.560	18.16	22.9	0.928

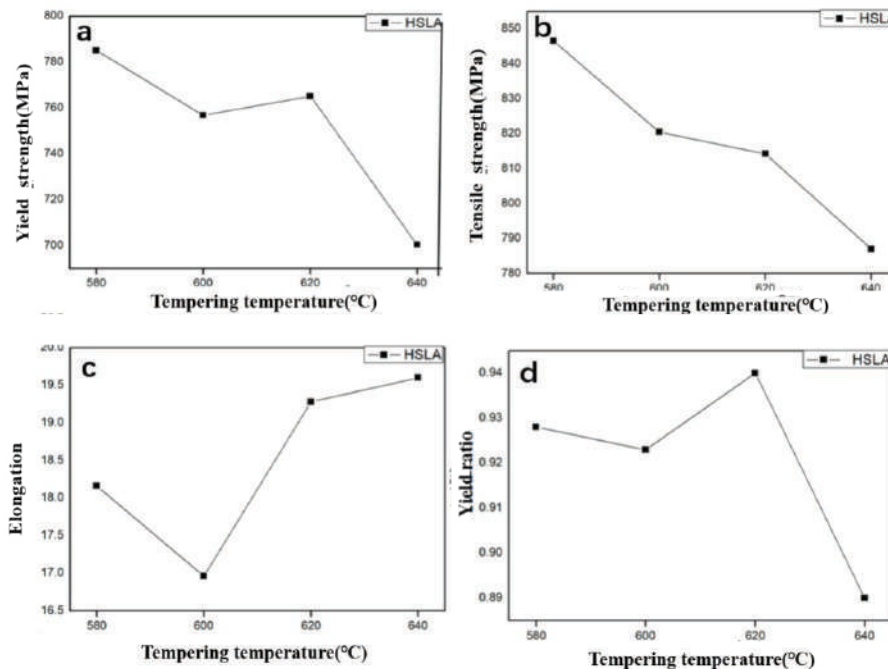
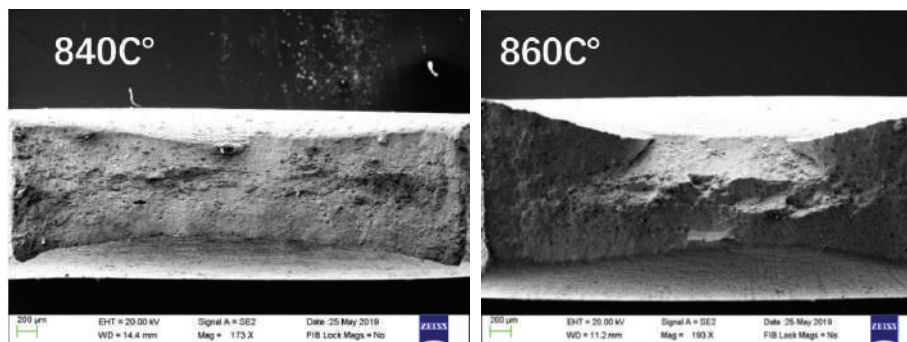


Figure 5. Mechanical properties of different tempering temperatures at 700 °C secondary quenching (a) Yield strength (b) Tensile strength (c) Elongation (d) Yield ratio



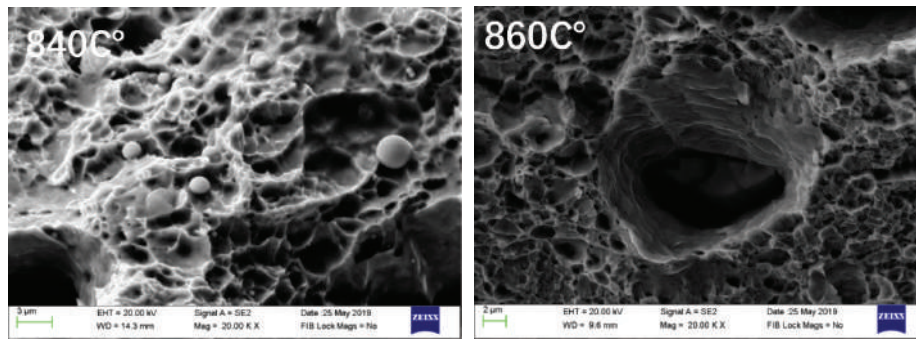


Figure 6. Fracture surface of steel sample quenched at 840 and 860 °C

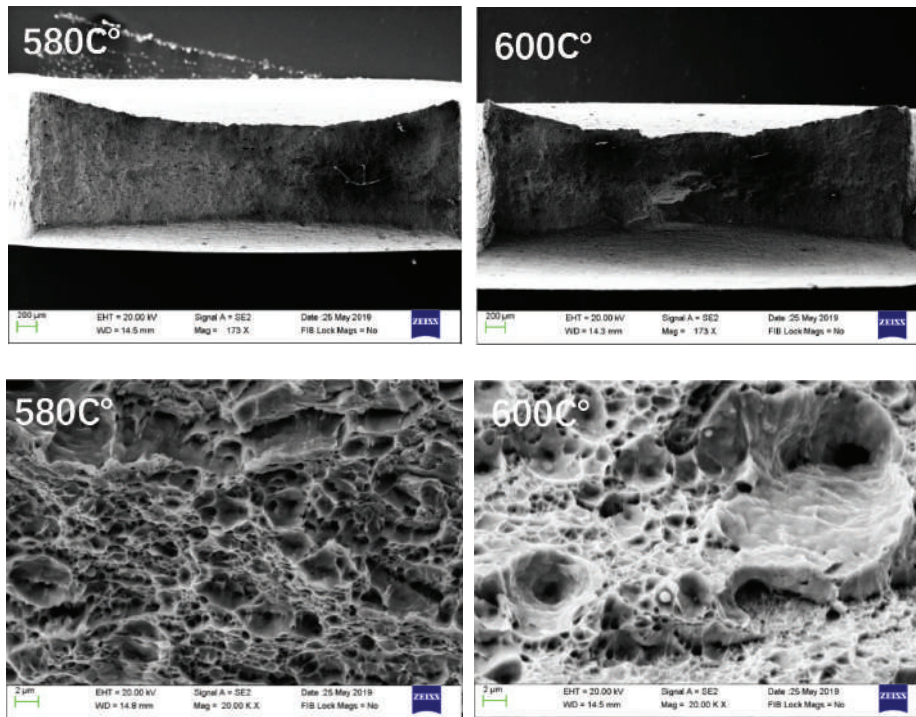


Figure 7. Fracture surface of steel sample tempered at 580 and 600 °C, following secondary quenching at 700 °C

4. Conclusion

(1) Metallographic structure under QT state is mainly consisted of tempered troostite in slat form. The steel under QT state (quenching at 860°C and tempering at 600°C) obtains the optimized comprehensive mechanical properties, with the yield strength of 881 MPa, tensile strength of 909MPa, elongation after fracture of 13.92 %, and yield ratio of 0.969.

(2) The QLT treatment gives the best elongation values compared with QT process, and the optimum QLT heat treatment parameters are determined as Q: 860 °C, L: 700 °C and T: 600 °C, with the yield strength of 756MPa, tensile strength of 820MPa, elongation after fracture of 16.76 %, and yield ratio of 0.923. After QLT treatment, the two-phase structure is formed with soft ferrite and hard tempered martensite, which degrades yield ratio and improves elongation.

(3) The tensile fracture surfaces of the QT and QLT

steels show that the number density and depth of dimples quenching at 840°C (during QT process) and tempered at 580°C (during QLT process) are less and smaller than those of their counterparts, respectively. The dense and deep dimples during tensile fracture induce higher toughness in the former steels.

Acknowledgments: This work was supported by the Project funded by China Postdoctoral Science Foundation, the Fundamental Research Funds for the Central Universities (No. FRF-TP-19-002A1), Domain Foundation of Equipment Advance Research of 13th Five-year Plan (No. 61409220124).

References

- [1] Czyryca, E.J. Advances in High Strength Steel Technology for Naval Hull Construction. Key Eng. Mater. 84–85, 491–520.

- [2] Jun Shao. Research status and development of ship steel [J]. *Angang Technology* 2013, (04), 1-4.
- [3] Wenkui Hao; Zhiyong Liu; Xianzong Wang; Xiaogang Li. The current status and development trend of strength and corrosion resistance of high-strength steel for ships [J]. *Equipment Environmental Engineering* 2014, 11 (01), 54-62.
- [4] Shike Yin, Changhong He, Yalin Li. Submarine steel and its welding materials in the United States and Japan [J]. *Materials Development and Application* 2008, (01), 58-65.
- [5] Heng Ma, Zhonghua Li, Xiaobo Zhu, et al. Development status of thick steel for aircraft carrier [J]. *Shandong Metallurgy* 2010, 32 (2), 8-10.
- [6] Xiaoyan Huang, Bo Liu. Structural materials for ships current status and development [J]. *Ship & Boat* 2004, (3), 21-24.
- [7] Shidong Wu. Development and Application of Structural Steel for U.S. Ships Study [J]. *Shanghai Shipbuilding* 2006, (4), 57-60.
- [8] Xin'an Cheng. Review and Prospect of Overseas Ship Steel [J]. *Development and Application of Materials* 1997, 12 (2), 46-48.
- [9] Chen X Z, Huang Y M. Microstructure and properties of 700MPa grade HSLA steel during high temperature deformation [J]. *Journal of Alloys and Compounds* 2015, 631:225-231. Fernandez J, Illesca S S, Guilemany J M. Effect of microalloying elements on the austenitic grain growth in a low carbon HSLA steel [J]. *Materials Letters* 2007, 61 (11), 2389-2392.
- [10] Fernandez J, Illesca S S, Guilemany J M. Effect of microalloying elements on the austenitic grain growth in a low carbon HSLA steel [J]. *Materials Letters* 2007, 61 (11), 2389-2392.
- [11] Heller S R, Friti I, John V. An evaluation of HY-80 steel as a structural material for submarine, Part I [J]. *Naval Engineering Journal* 1965, (2).
- [12] Heller S R, Friti I, Vasta J. An evaluation of HY-80 Steel as a structural material for submarine Part II [J]. *Naval Engineering Journal* 1965, (4).
- [13] Katsumata M, Ishiyama O, Inoue T. Microstructure and Mechanical Properties of Bainite Containing Martensite and Retained Austenite in Low Carbon HSLA Steels 1991(08).
- [14] S D, A G, S C. Microstructural characterization of controlled forged HSLA-80 steel by transmission electron microscopy [J]. *Materials Characterization* 2003, 50 (4-5), 305-315.
- [15] The State-of-Art and Development Trends of HSLA Steels in China [J]. *Journal of Iron and Steel Research* 2011, 18 (S1), 1-13.
- [16] Yuan G. Kang J, Zhaodong W, Guodong W. Effect of Heat Treatment on Microstructure and Mechanical Properties of HSLA Plate Steel [A]. Chinese Society for Metals. Proceedings of the 10th International Conference on Steel Rolling [C]. 2010; 4.
- [17] Chaudhury Z A, Sarma D S. Influence of Heat Treatment on Structure and Properties of a HSLA Steel, 1982; (02).
- [18] Bai D Q, Yue S, Maccagno T M. Effect of Deformation and Cooling Rate on the Microstructures of Low Carbon Nb-B Steels, 1998; (04).
- [19] S.J. Wu, G.J. Sun, Q.S. Ma, Q.Y. Shen, L. Xu. Influence of QLT treatment on microstructure and mechanical properties of a high nickel steel [J]. *Journal of Materials Processing Tech* 2013, 213 (1).
- [20] Yongchang Liu, Lei Shi, Chenxi Liu, Liming Yu, Zesheng Yan, Huijun Li. Effect of step quenching on microstructures and mechanical properties of HSLA steel [J]. *Materials Science & Engineering A* 2016, 675.
- [21] M.R. Akbarpour, A. Ekrami, Effect of Ferrite Volume Fraction on Workhardening Behavior of High Bainite Dualphase (DP) Steels, *Mater. Sci. Eng. A* 477, 2008; 306-310.
- [22] R. Bakhtiari, A. Ekrami, The Effect of Bainite Morphology on the Mechanical Properties of a High Bainite Dualphase (HBDP) Steel, *Mater. Sci. Eng. A* 525, 2009; 159-165.
- [23] Yasong Li, Ruixuan Li, Yong Zhang. Effects of Si Addition on Microstructure, Properties and Serration Behaviors of Lightweight Al-Mg-Zn-Cu Medium-entropy Alloys [J]. *Research and Application of Materials Science* 2019, (01), 13-22.
- [24] Xiaohua Chen, Lili Qiu, Hao Tang, Xiang Luo, Longfei Zuo, Zidong Wang, Yanlin Wang. Effect of nanoparticles formed in liquid melt on microstructure and mechanical property of high strength naval steel [J]. *Journal of Materials Processing Tech.*, 2015, 223-224
- [25] Tang, H., Chen, X.H., Chen, M.W., Zuo, L.F., Hou, B., Wang, Z.D., Microstructure and Mechanical Property of In-situ Nano-particle Strengthened Ferritic Steel by Novel Internal Oxidation, *Mater. Sci. Eng.* 2014; A 609, 293-299.
- [26] Ruiyang Wang, Shiqing Sun, Song Wang, Nianlun Wei, Boshuai Cui. Analysis of M50 bearing steel turning bend fracture [J]. *Internal Combustion Engines and Parts* 2019, (04), 61-62.
- [27] Kai Feng, Daming Jiang, Bande Hong. Fracture Analysis of Low Carbon Duplex Steel [J]. *Materials for Mechanical Engineering* 1992, (03), 58-61.

Adsorption of U(VI) onto Amidoxime-functionalized Hydrothermal Carbon in the Presence of Ca-U(VI)-CO₃ Complexes

Yinghui XIE, Zhimmin DONG, Haoyan ZHANG, Runze ZHOU, Yunhai LIU, Zhibin ZHANG*

State Key Laboratory of Nuclear Resources and Environment, East China University of Technology, Nanchang, Jiangxi, China, 330013

*Corresponding Author: Zhibin ZHANG, at Key Laboratory of Nuclear Resources and Environment, East China University of Technology, Nanchang, Jiangxi, China

Abstract:

The aim is collecting uranium from groundwater in which uranium mainly exists in negative species, the amidoxime-functionalized hydrothermal carbon (AO-HTC) was synthesized. From the results of N₂ adsorption-desorption and SEM, AO-HTC is a small spherical surface; FT-IR and Elemental analysis showed that the amidoxime group was successfully grafted onto the surface of the material; Zeta-potential measurement showed that the amino nitrogen atom is protonated in the oxime group. The optimum pH value of AO-HTC for uranium adsorption is 6.0, and the adsorption equilibrium is reached within 80 min, which is in accordance with the pseudo-second order adsorption kinetic model. The adsorption of uranium by AO-HTC accords with the Langmuir isotherm adsorption model, and the single-layer saturated adsorption capacity is 254.13 mg·g⁻¹. The thermodynamic parameters calculated by the adsorption isotherm indicate that AO-HTC adsorption of uranium is a spontaneous endothermic chemical process and Carbonate ion, calcium ion and humic acid concentration have great influence on uranium adsorption. The experiments results show that AO-HTC has the potential to elimination of U(VI) from groundwater.

Keywords: uranium; amidoxime; hydrothermal carbon; adsorption; Ca-U(VI)-CO₃ complexes

1. Introduction

Nowadays, the soil has been polluted to varying degrees around the uranium smelter and the tailings pond, causing serious damage to the surrounding environment, and the groundwater has been seriously threatened with the migration of nuclide in the soil^[1, 2]. Groundwater is an important resource for human being survival, it is a limited ecological resource that only accounts for a small part of the total water resources. The contribution of groundwater is crucial perhaps as many as 2 billion people rely directly on aquifers for drinking water^[3]. In China, some of the regions like arid zones of Northwest China are entirely dependent on groundwater^[4]. If it is not well managed, groundwater resources are highly vulnerable to widespread pollution.

There are some differences in the presence of uranium under aerobic and anaerobic conditions^[5]. Under aerobic conditions, uranium mainly exists in the oxidation state of U(VI). For example, uranium form is UO₂²⁺ (uranyl) in acidic water with pH < 2.5. Under anaerobic conditions, U(VI) is easily reduced to insoluble U(IV), and the solubility of the reduced state is only one ten-thousandth of the oxidation state^[6]. Therefore, the reduced state U(IV)

is not easy to migrate in the environment, the pollution source is not easily diffused, and as not as possible widespread contamination. The existence of U(VI) in soil and groundwater is the key point of current research^[7].

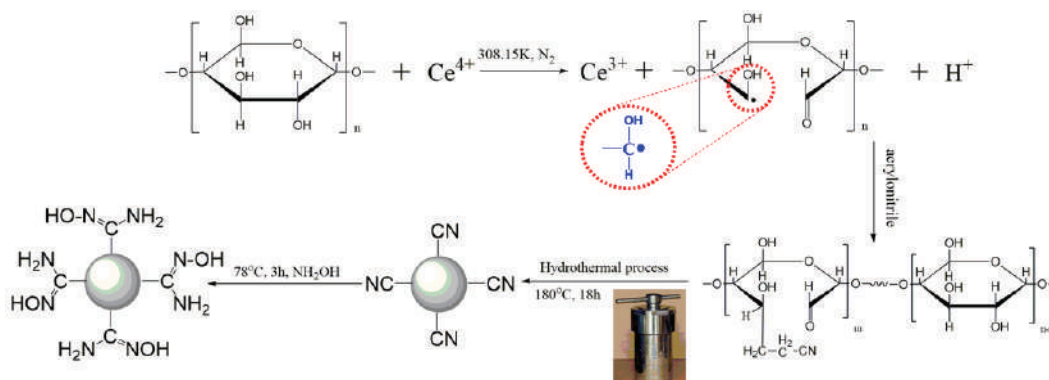
The difference in morphology is the main reason for the low removal efficiency. In the complex natural environment, many factors affect the morphology of uranium, mainly two points. First, soluble organic carbon, which is mainly humic acid in soil and groundwater, humic acid is one a mixture rich in oxygen-containing functional groups (hydroxyl, carboxyl, etc.). humic acid reacts with U(VI) to form soluble salt in natural water (alkaline), thus changing the existing form of uranium. In groundwater, uranium does not precipitate with anions such as (UO₂)₂(OH)₂²⁺, but one or several soluble complexes ions are easy to migrate such as UO₂(CO₃)₂²⁻, UO₂(CO₃)₃⁴⁻, UO₂CO₃ (aq), etc^[8-10]. Second, calcium and alkaline earth metal ions in the environment, rocks and soil rich in carbonate minerals, after the erosion of rainwater and river water, some carbonate minerals will be washed into small particles, the surface portion will dissolve at the same time^[11]. Therefore, natural water contains a certain amount

of alkaline earth metal ions such as Ca^{2+} and Mg^{2+} . The pH of water in nature is close to neutral, which is conducive to the dissolution of carbon dioxide gas in the air, further increasing the concentration of carbonate ions in water^[12, 13]. It has been reported that the main forms of uranium are $\text{Ca}_2\text{UO}_2(\text{CO}_3)_3(\text{aq})$, $\text{CaUO}_2(\text{CO}_3)_2^-$ and $\text{MgUO}_2(\text{CO}_3)_3^{2-}$ in the natural waters^[14].

The form of uranium in soil or groundwater (such as $\text{UO}_2(\text{CO}_3)_2^{2-}$, $\text{UO}_2(\text{CO}_3)_3^{4-}$, $\text{UO}_2\text{CO}_3(\text{aq})$, $\text{Ca}_2\text{UO}_2(\text{CO}_3)_3(\text{aq})$ and $\text{CaUO}_2(\text{CO}_3)_2^-$, etc.) is similar to that in seawater ($\text{UO}_2(\text{CO}_3)_3^{4-}$, $\text{CaUO}_2(\text{CO}_3)_2^-$ and $\text{MgUO}_2(\text{CO}_3)_3^{2-}$, etc.)^[15, 16]. The terrible ability to identify interacting species of oxygen-containing functional group, which limits the application of HTC functional materials in certain fields. However, the amidoxime group has attracted much attention for the high chelation affinity and selectivity of uranium by the reaction of nitrile groups with hydroxylamine, which has been supported on various materials (such as polymeric fibers, porous polymers, metal organic framework) exhibit superiority to uranium adsorption^[17, 18]. In groundwater, uranyl was contacted with amidoxime in the form of $\text{UO}_2(\text{CO}_3)_2^{2-}$ or $\text{UO}_2(\text{CO}_3)_3^{4-}$, and

then the chelating uranyl was coordinated with amidoxime group and absorbed by the amidoxime-based adsorbent^[19, 20]. Therefore, the feasibility and abundance of amidoxime are two key points determining the adsorption capacity of uranium.

In this work, an amidoxime functionalized hydrothermal carbon adsorption material was prepared as an adsorbent for treatment of uranium-containing groundwater. The amidoxime group can be obtained by reduction of a nitrile group, and the reaction conditions are were no longer various conventional modification processes. The acrylonitrile can be grafted onto the starch by a polymerization grafting method^[21]. The grafted starch is further hydrolyzed to obtain a nitrile-grafted hydrothermal carbon intermediate. Finally, the nitrile group is reduced to an amidoxime group in a hydroxylamine hydrochloride solution to obtain a desired hydrothermal carbon adsorbent. The effects of amidoxime-functionalized hydrothermal carbon adsorbent on the removal of uranium from water were studied by batch experiments. The effects of pH value, carbonate, calcium and humic acid content on the removal efficiency were investigated.



Scheme 1. Schematic of processes for AO-HTC

2. Experimental

2.1 Synthesis of amidoxime-functionalized hydrothermal carbon (AO-HTC)

The preparation process of AO-HTC is shown in Scheme 1. Generally, 10 g soluble starch was dissolved in 100 mL of deionized water, then, the reaction system was heated at 35 °C for 2 h and stirred under a nitrogen atmosphere, added to ceric ammonium nitrate solution to react for 30 min, 2 mL acrylonitrile was added into and reacted 80 °C for 2 h. It was observed that the starch remained solid and not gelatinized, the product was washed 3 times with absolute ethanol, and finally the product was washed twice with deionized water and dried. An acrylonitrile grafted starch (AN-Starch) was obtained. The prepared 6.67 g of AN-starch was dissolved in 50 mL of distilled water, uniformly stirred for 30 min, and then transferred to a 100 mL Teflon-lined stainless steel autoclave, followed by heating at 180 °C for 18 h. The intermediate product was washed thoroughly with deionized water and ethanol, and

then dried in a vacuum oven at 60 °C for 24 hours. Finally, 1.0 g intermediate product was added to 40 mL of 40 g·L⁻¹ hydroxylamine hydrochloride solution and stirred at 78 °C for 3 h. Then, the mixture was filtered; the resultant was thoroughly washed with deionized water and ethanol, and then dried under vacuum at 60 °C overnight.

2.2 Results and discussion Characterization

SEM

The scanning electron microscope was used to characterize the micro-morphology and particle size of carbon microspheres. The images of the as-synthesized samples displayed in Fig. 1(a) clearly show that large number of spherical nanoparticles after hydrothermal carbonization, moreover, the surface is regular, and no significant morphological change is observed for AO-HTC and the particle size of the AO-HTC is in the range of about 2 to 7 μm. It is found in that the AO-HTC particles are decentralized with each other.

FT-IR

The FT-IR spectra were analyzed to investigate the surface

functional groups of AO-HTC (Fig. 1(b)). The AO-HTC shows the common stretching bands at 1604 and 3248 cm^{-1} , which are associated with C=O carboxylate and O-H groups, respectively^[22]. After being modified with AO, three peaks appear at 1631 cm^{-1} , 1272 cm^{-1} and 927 cm^{-1} , belonging to C=N or C=C, C-N and N-O stretching vibrations, respectively^[21]. It is clearly indicating that the nitrile group have been converted to the amidoxime group in the presence of hydroxylamine hydrochlorid^{e[23]}.

Zeta potential

Fig. 1(c) shows the zeta potential curve of AO-HTC, indicating that the zeta potential of AO-HTC is positive at $\text{pH} < 4.76$, due to the protonation of the N atom of $-\text{NH}_2$ in the amidoxime groups, this is favorable for adsorption of positively uranyl ions. Moreover, with the pH value increasing, the potential of the AO-HTC becomes negative value, the reason is that the deprotonation of $-\text{NH}_2$ in the amidoxime groups and increased the dissociation of oxime hydroxyl groups^[24]. After $\text{pH} > 4.76$, due to the deprotonation of the amidoxime group, the dissociation of the oxime hydroxyl group is increase, and the zeta potential of the AO-HTC becomes negative, which is favorable for binding to the positive radionuclide ion. Moreover, the point of zero charges of AO-HTC was 4.76 mV, which is beneficial to reduce the surface of AO-HTC adsorbent Electrostatic repulsion of uranium in solution. The property of the amidoxime group is of great importance for the removal of uranium in the environment.

N₂-BET

The N₂ adsorption-desorption isotherm and pore size distribution of AO-HTC are shown in Fig. 1(d) and Table 1. It can be observed that type IV isotherm curves with

H₂ hysteresis loops at relative pressures ($P/P_0 = 0.5$), which is typical for mesoporous structures and also indicates that the mesostructure of AO-HTC. However, the average pore diameter was 7.93 nm indicating that the polyacrylamidoxime groups distribution on the surface of the material and limited the pore size. This amidoxime surface of the AO-HTC was good for binding the uranium and allowing the uranium to adsorb on the adsorption sites on the surface of the material.

Table 1. Structural and textural properties of AO-HTC.

Material	Surface area SBET ($\text{m}^2 \cdot \text{g}^{-1}$)	Pore volume ($\text{cm}^3 \cdot \text{g}^{-1}$)	Average pore diameter (nm)
AO-HTC	2.75	0.02	7.93

2.3 Elemental analysis

Elemental analysis was used to calculate the exact number of amidoxime group in AO-HTC. Table 2 shows the content of carbon, nitrogen and hydrogen by modifying HTC, the nitrogen content of AO-HTC is 7.15%, indicating that the amidoxime group is grafted onto the surface of the HTC, as supporting by the previous FT- IR. The number of amidoxime group was calculated to be about 2.55 $\text{mmol} \cdot \text{g}^{-1}$ based on the increase in nitrogen content.

Table 2. The element analysis of AO-HTC.

Samples	C%	H%	N%
AO-HTC	50.82	4.62	7.15

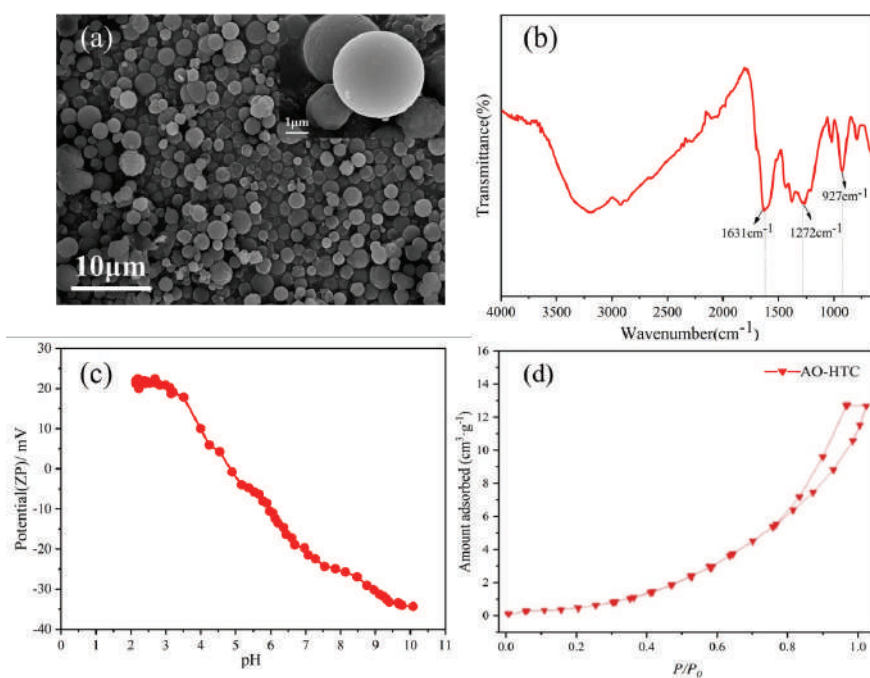


Figure 1. SEM images of AO-HTC (a), FT-IR spectra of AO-HTC (b), Zeta potentials of AO-HTC as a function of pH (c), Nitrogen adsorption-desorption isotherms and pore-size distribution for AO-HTC (d).

2.4 Batch sorption experiments

Effect of pH

The pH was regarded as one of the most important environmental factors effect the speciation of uranium ions^[25]. The influence of pH on the adsorption among AO-HTC and uranium ions was displayed in Fig. 2(a). With the increase of pH, the adsorption capacity of U(VI) was increased on AO-HTC, the maximum adsorption capacity was 254.13 mg·g⁻¹ at pH =6.0, it can be seen that the adsorption capacity of AO-HTC was better than other situations. Comparison of U(VI) adsorption of AO-HTC with other related adsorbents is listed in table 3. The AO-HTC has excellent performance under different adsorption conditions, which indicates that AO-HTC is an excellent choice for actual environmental pollution groundwater. U(VI) was mainly present in the form of UO_2^{2+} in this absorption reaction. The morphological distribution of uranium (VI) was simulated by Visual MINTEQ 3.1, as shown in Fig. 2(b), the morphology of uranium (VI) is UO_2^{2+} , UO_2OH^+ and $(UO_2)CO_3(aq)$ at $3.0 < pH < 5.0$ and $Ca_2(UO_2)(CO_3)_2(aq)$, $Ca(UO_2)(CO_3)_3^{2-}$ at $pH > 6$, combined with the Zeta potential, the calcium-uranium-carbonate complex $Ca_2UO_2(CO_3)_3$ and $UO_2(CO_3)_3^{2-}$ are increasing with pH, the amount of positively charged uranyl ion species gradually decreases, Which have a great influence for adsorption of uranium (VI).

2.5 Effect of carbonate

Uranium is usually present in the natural water environment as the form of uranyl carbonate, because uranium carbonate is a strong ligand^[34]. The effect of carbonate ions on the adsorption of uranium by AO-HTC was shown in Fig. 2(c). The adsorption capacity of AO-HTC for uranium gradually decreased from 214.54 mg·g⁻¹ to 103.32 mg·g⁻¹ by

increasing the carbonate ion concentration. It is observed from Fig. 2(d) that the carbonate concentration increased from 0 to 4.0 mmol·L⁻¹, the ions such as $(UO_2)_3(OH)_5^+$, UO_2^{2+} and $(UO_2)_4(OH)^{7+}$ decreased to an extremely low level and neutral $Ca_2UO_2(CO_3)_3(aq)$ and negative $(UO_2)_2CO_3(OH)_3^-$, $CaUO_2(CO_3)_3^{2-}$ species were obviously increased. In addition, the increase of the concentration of carbonate ions was lead to decrease potential value on the surface of the AO-HTC, and the formation of electrostatic repulsion between the uranium-carbonate and calcium-uranium-carbonate complex anions, which will impact the adsorption of uranium in the solution by the material, further reducing the AO-HTC adsorption capacity.

2.6 Effect of calcium

Calcium plays a key role in the adsorption of uranium in groundwater, Which forming a dikaryon or multikaryon complex such as $Ca_2UO_2(CO_3)_3(aq)$ and $CaUO_2(CO_3)_3^{2-}$ ^[35]. The effect of calcium ions on the adsorption of uranium by AO-HTC was shown in Fig. 2(e). With the increasing of calcium ions concentration, the adsorption capacity of AO-HTC to uranium gradually decreased from the original 201.34 mg·g⁻¹ to 107.12 mg·g⁻¹. Combined with the distribution pattern of uranyl ions in the aqueous phase, the morphological distribution at different calcium concentrations was calculated by Visual MINTEQ 3.1 software as shown in Fig. 2(f). With the increase of Ca^{2+} concentration from 0 to 2.0 mmol·L⁻¹, the negatively charged $UO_2(CO_3)_3^{4-}$, $UO_2(CO_3)_2^{2-}$ and $(UO_2)_2CO_3(OH)_3^-$ were almost disappeared, which are forming a calcium-uranium-carbonate complex $Ca_2UO_2(CO_3)_3$ and $CaUO_2(CO_3)_3^{2-}$ that declined the ability of materials to adsorb uranium.

Table 3. Comparison of adsorption capacities of various adsorbents for uranium(VI)

Sorbents	Experimental conditions	Adsorption capacities (mg·g ⁻¹)	References
Mesoporous Carbon	PH=6.5	178.6	[26]
PANI/CMK-3	PH=6.0	118.3	[27]
AO-CMK-3	PH=5.0	238.7	[28]
AO-OMC	PH=5.0	322.6	[22]
Activated Carbon	pH=3.0	28.3	[29]
AO-Polyethylene Fibers	PH=4.0	176.1	[30]
Fe3O4	PH=5.5	228.2	[31]
CMK-5	PH=4.0	65.4	[32]
CMK-3-COOH	PH=6.5	250.0	[26]
HTC-COOH	PH=6.0	205.8	[33]
AO-HTC	PH=6.0	254.1	This Work

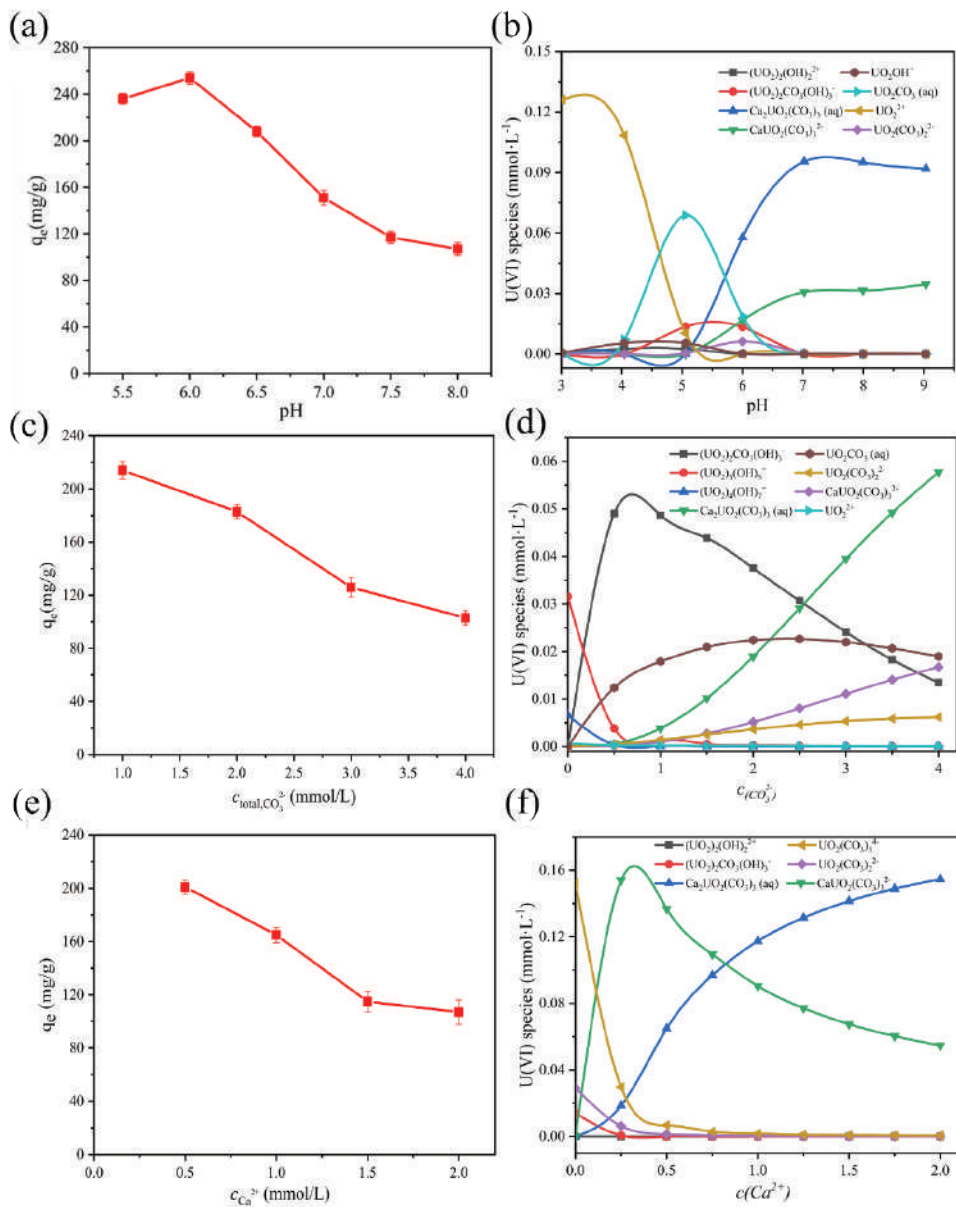


Figure 2. Effect of (a) pH on the adsorption of uranium on AO-HTC and (b) the distribution of uranium in in different pH solution ($C_0 = 50 \text{ mg}\cdot\text{L}^{-1}$, $m = 10 \text{ mg}$, $C[\text{Ca}^{2+}] = 2.0 \text{ mmol}\cdot\text{L}^{-1}$, $C[\text{CO}_3^{2-}] = 4.0 \text{ mmol}\cdot\text{L}^{-1}$, $t = 180 \text{ min}$, $T = 298.15 \text{ K}$), Effect of (c) CO_3^{2-} concentration on the adsorption of uranium on AO-HTC and (d) the distribution of uranium in in different concentration of CO_3^{2-} solution ($\text{pH} = 6.0$, $m = 10 \text{ mg}$, $C_0 = 50 \text{ mg}\cdot\text{L}^{-1}$, $C[\text{Ca}^{2+}] = 2.0 \text{ mmol}\cdot\text{L}^{-1}$, $t = 180 \text{ min}$, $T = 298.15 \text{ K}$), Effects of (e) Ca^{2+} concentration on the adsorption of uranium on AO-HTC and (f) the distribution of uranium in different concentration of Ca^{2+} solution ($\text{pH} = 6.0$, $C_0 = 50 \text{ mg}\cdot\text{L}^{-1}$, $m = 10 \text{ mg}$, $C[\text{CO}_3^{2-}] = 4.0 \text{ mmol}\cdot\text{L}^{-1}$, $t = 180 \text{ min}$, $T = 298.15 \text{ K}$)

2.7 Effect of humic acid

Humic acid has a strong affinity for environmental substances in various natural water systems, which possibly have an impact on uranium adsorption^[36, 37]. The effect of humic acid on the adsorption of uranium by AO-HTC is shown in Fig. 3(a). The adsorption capacity of AO-HTC for uranium decreased from $109.92 \text{ mg}\cdot\text{g}^{-1}$ to $39.78 \text{ mg}\cdot\text{g}^{-1}$ with the increase of humic acid concentration. The reason is that humic acid is rich in affinity of adsorption groups such as carbonyl, carboxyl, and hydroxyl groups, which

can occupy the adsorption sites of the adsorbents, resulting in a decrease in the adsorption amount of uranium. humic acid in the solution easily combines with free uranium to generate a U(VI)-humic acid complex, which has a tight colloidal structure and is not easily adsorbed by AO-HTC^[17]. Meanwhile, humic acid will compete with uranium to adsorb on the surface of AO-HTC^[38]. The adsorbed humic acid is not easy to combine with uranium in the solution, further reducing the adsorption of uranium on AO-HTC.

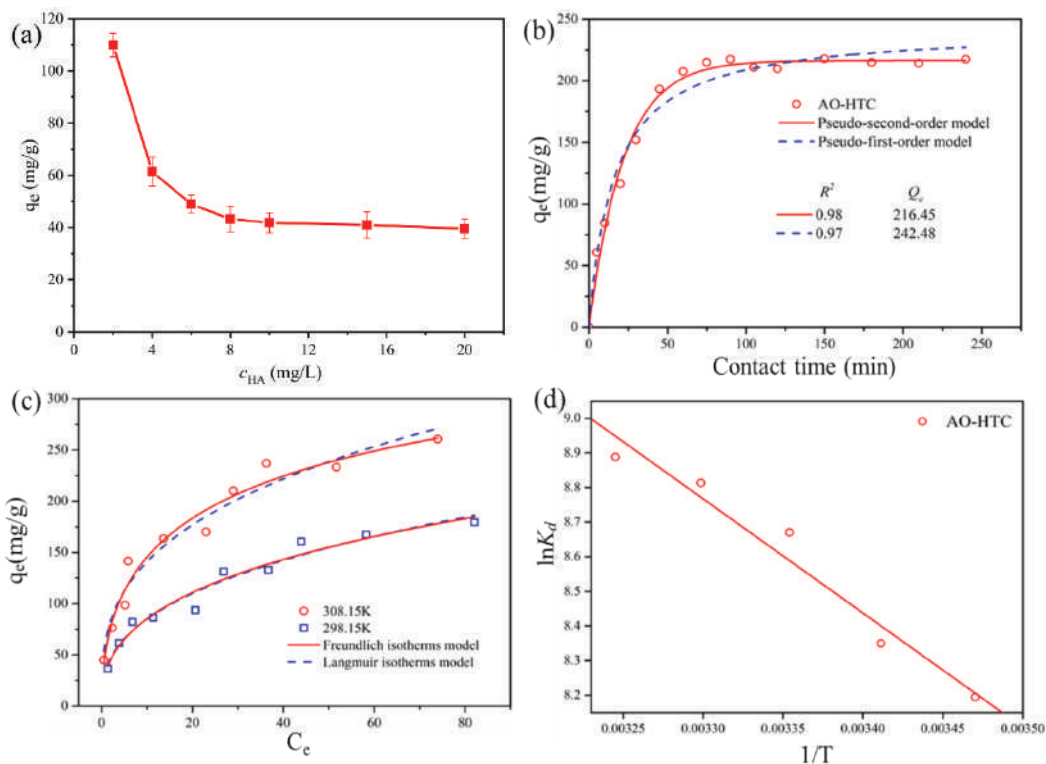


Figure 3. (a) Effects of humic acid concentration on the uranium adsorption on AO-HTC ($C_0 = 50 \text{ mg}\cdot\text{L}^{-1}$, $m = 10 \text{ mg}$, $[\text{Ca}^{2+}] = 2.0 \text{ mmol}\cdot\text{L}^{-1}$, $[\text{CO}_3^{2-}] = 4.0 \text{ mmol}\cdot\text{L}^{-1}$, $t = 180 \text{ min}$, $T = 298.15 \text{ K}$). (b) The adsorption kinetics of U(VI) on AO-HTC ($C_0 = 50 \text{ mg}\cdot\text{L}^{-1}$, $m = 10 \text{ mg}$, $\text{pH} = 6.0$, $T = 298.15 \text{ K}$). (c) The adsorption isotherms of U(VI) on AO-HTC at 298.15 K and 308.15 K ($\text{pH} = 6.0$, $m = 10 \text{ mg}$, $t = 180 \text{ min}$, $T = 298.15 \text{ K}$). (d) The thermodynamic fitting ($C_0 = 50 \text{ mg}\cdot\text{L}^{-1}$, $m = 10 \text{ mg}$, $\text{pH} = 6.0$, $t = 180 \text{ min}$)

2.8 Kinetic studies

The contact time has a great influence on the mass transfer rate of metal ions in aqueous solution. The result shown in Fig. 3(b), it is seen that the adsorption quantity of AO-HTC increases with the contact time, and reaches the adsorption equilibrium at 80 min. When the equilibrium time is exceeded, since the active site on the surface of the adsorbent material has been occupied, the amount of adsorption no longer changes significantly. It was attributed to the synergy of the rich oxygen-containing functional groups with the C-N bond, providing sufficient active sites for the immobilization and binding of U(VI).

The contact time can reflect adsorption kinetics, and the experimental data can be used to calculate whether the pseudo-first-order and pseudo-second-order kinetic equations are analyze the adsorption process.^[39, 40], which were exhibited as follows:

$$\ln(q_e - q_t) = \ln q_e - k_1 t \quad (1)$$

$$\frac{t}{q_t} = \frac{1}{k_2 q_e^2} + \frac{t}{q_e} \quad (2)$$

Where q_e and q_t were the amounts of absorbed U(VI) after equilibrium at a time “t”, k_1 and k_2 were the constant for the pseudo-first-order and pseudo-second-order kinetic rat, respectively. These values can be obtained from the linear graph of $\ln(q_e - q_t)$ vs t as shown in Fig. 3(b), and these parameters were tabulated in table 4. The higher correlation coefficient indicated that the adsorption kinetics of U(VI) on AO-HTC fitted well with the pseudo-second-order kinetic model. Meanwhile, the theoretical calculated q_2 ($234.74 \text{ mg}\cdot\text{g}^{-1}$) of the pseudo-second-order kinetic model is very close to the experimental q_e ($207.06 \text{ mg}\cdot\text{g}^{-1}$) at 298.15 K. Therefore, adsorption behavior was mainly controlled by chemical reaction rather than physical process. In addition, this is also based on the assumption that the rate-limiting step may be chemical adsorption, involving valence electron forces through electron sharing or exchange between the surface groups of AO-HTC and uranium.

Table 4. Parameters for Kinetic models of U(VI) adsorption by AO-HTC and HTC

Absorbent	$q_{e,exp}$ ($\text{mg}\cdot\text{g}^{-1}$)	pseudo-first-order kinetic model			pseudo-second-order kinetic model		
		$q_{1,cal}$ ($\text{mg}\cdot\text{g}^{-1}$)	k_1 (min^{-1})	R^2	$q_{2,cal}$ ($\text{mg}\cdot\text{g}^{-1}$)	k_2 ($\text{g}\cdot\text{mg}^{-1}\cdot\text{min}^{-1}$)	R^2
HTC	50.02	17.97	1.42×10^{-2}	0.908	50.99	2.21×10^{-3}	0.997
AO-HTC	207.06	125.22	2.75×10^{-2}	0.906	234.74	2.32×10^{-3}	0.991

2.9 Adsorption Isotherms Studies

To explore the adsorption behavior and reaction mechanism of uranium ionic, two typical isotherm models, i.e., the Langmuir isotherm models and Freundlich isotherm models^[41], were studied under the condition of T = 298.15 K and T = 308.15 K. The adsorption isotherms of U(VI) were shown in Fig. 3(c). It can be seen that the adsorption reacting reach equilibrium rapidly. The adsorption capacity of U(VI) on AO-HTC was improved with increasing equilibrium concentration of U(VI). Langmuir and Freundlich's models were applied to fit the experimental data and analyze the adsorption mechanism of uranium on AO-HTC. The two adsorption isotherms models were expressed as Eqs. (3) and (4):

$$\frac{C_e}{q_e} = \frac{1}{q_m K_L} + \frac{C_e}{q_m} \quad (3)$$

$$\ln q_e = \ln K_F + \left(\frac{1}{n}\right) \ln C_e \quad (4)$$

Where q_e was regarded as the sorption capacity of U(VI) on AO-HTC at equilibrium time. K_L and K_F considered as constants of Langmuir and Freundlich separately, n was the factor of Freundlich related to the sorption intensity. C_e was the equilibrium concentration of U(VI), q_m was the maximum saturated sorption capacity between AO-HTC and uranyl ions.

Langmuir isotherm model used to extensively describe monolayer adsorption which occurs between the homogeneous active sites on the surface of adsorbent and target ions. Freundlich isotherm model assumes a multilayer sorption reaction was present among adsorbent with heterogeneous active sites and adsorbate. The relative parameters were obtained from the two isotherms models simulation curves Fig. 3(c) and table 5, which illustrated that the experimental data was fitted the Langmuir isotherm models well ($R^2 > 0.99$). Demonstrating the adsorption behavior was monolayer sorption process. Compared with HTC, the maximum saturated adsorption capacity of U(VI) on AO-HTC (244.11 mg·g⁻¹) increased significantly. Which was attributed to the enhanced active sites and abundant amidoxime groups were distributed on the surface of HTC.

2.10 Thermodynamic studies

The thermodynamic indices were introduced to investigate

Table 5. Parameters for Langmuir, Freundlich isotherm models

Adsorbent	Langmuir isotherm			Freundlich isotherm		
	K_L	q_m (mg·g ⁻¹)	R^2	K_F	n	R^2
HTC	0.025	128.58	0.957	13.33	2.29	0.939
AO-HTC	0.048	244.11	0.991	22.01	1.80	0.933

Table 6. Thermodynamic parameters of U(VI) adsorption on AO-HTC and HTC

Adsorbent	ΔH (kJ·mol ⁻¹)	ΔS (J·mol ⁻¹ ·K ⁻¹)	ΔG (kJ·mol ⁻¹)				
			288.15 (K)	293.15 (K)	298.15 (K)	303.15 (K)	308.15 (K)
HTC	25.39	143.04	-15.82	-16.54	-17.25	-17.97	-18.68
AO-HTC	18.04	128.29	-18.92	-19.56	-20.21	-20.85	-21.49

the effect of temperature on adsorption reaction and analysis adsorption mechanism. Various thermodynamic parameters i.e., ΔS (J·K⁻¹·mol⁻¹), ΔG (kJ·mol⁻¹) and ΔH (kJ·mol⁻¹), were based on the equations (5)-(6) which were employed to calculate the feasibility of the sorption process^[42].

$$\ln K_d = \frac{\Delta S}{R} - \frac{\Delta H}{RT} \quad (5)$$

$$\Delta G = \Delta H - T\Delta S \quad (6)$$

Where the K_d was the constant of the thermodynamic equilibrium, and $R = 8.314$ J·mol⁻¹·K⁻¹ was the ideal gas constant. T represented the absolute temperature.

The thermodynamic experimental data were listed in table 6 which under the condition of T=288.15 K, T=293.15 K, T=298.15 K, T=303.15 K and T=308.15 K. the ΔH value and ΔS value for the sorption process were obtained by simulating the slope and intercept of the curves as shown in Fig. 3(d). The values of ΔG were regressed to describe the thermodynamic properties of the sorption process. The positive ΔS values and the positive ΔH values indicating that the adsorption reactive was an endothermic process with entropy increased, and under the condition of the increasing temperature the values of negative ΔG were decreased. It was demonstrated that higher temperature has positive effect on the spontaneous sorption behavior, and more active groups catch uranium ions by complexation reaction. This result superimposed revealing that the adsorption behavior was controlled by chemisorption.

2.11 Desorption and reusability

Regeneration-reusability is very important for economic value and environment friendly in practical application. desorption experiments of U(VI) were performed with 1 mol/L Na₂CO₃ solution, 1 mol/L HCl solution and 1 mol/L HNO₃ solution, As can be seen from Fig. 4(a), 1 mol/L HNO₃ solution was best eluent for desorption of U(VI) on AO-HTC. The results were shown in Fig. 4(b), the sorption capacity of U(VI) decreased slightly from 231.8 mg·g⁻¹ to 220.2 mg·g⁻¹ after five consecutive sorption-desorption cycles, which indicates that the surface groups of material exhibits high structural stability in HTC, and revealing the AO-HTC presented excellent reusability that is great importance for the groundwater remediation of U(VI).

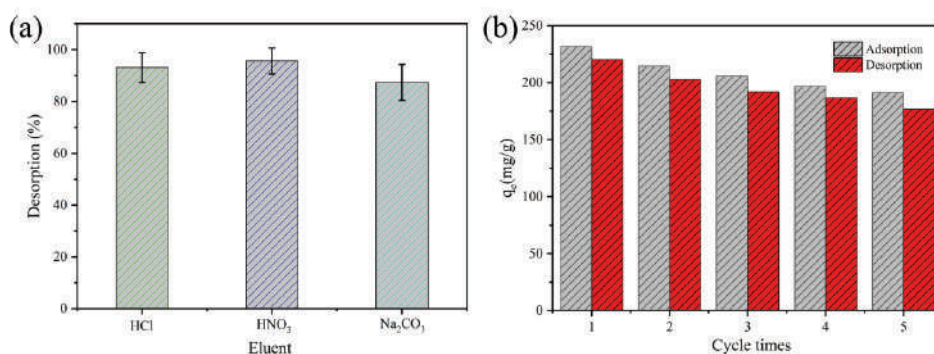


Figure 4. Desorption of uranium with various eluent (a), regenerated use of AO-HTC (b).

2.12 Post-sorption characterization

FT-IR and SEM were used to further observed the changes in the microstructure and morphology of the AO-HTC after adsorption of U (VI). In the FT-IR spectrum of Fig. 5(a), the characteristic stretching vibration of $[O=U(VI)=O]^{2+}$ at 919 cm⁻¹ to 968 cm⁻¹ was overlapped by the stretching vibration of C-O or N-O^[43]. In addition, the characteristic peaks of other groups obviously displacements among the amidoxime, carboxylic and hydroxylic or amidogen groups (766 cm⁻¹ to 1056 cm⁻¹, 1506 cm⁻¹ to 1788 cm⁻¹, 3390 cm⁻¹

to 3448 cm⁻¹), which could be amidoxime and carboxylic groups banding with uranyl ion on the surface of AO-HTC, and reduced the band intensity of functional groups^[44]. The SEM images confirmed that the morphology of AO-HTC was well preserved after adsorption (Fig. 5(b-c)), and the surface of AO-HTC showed abundant pores, which was helpful to improve the grafting rate of amidoxime groups on HTC. In Fig. 5(d), The SEM elemental mapping images further proves that the radionuclide was anchored onto the surface of AO-HTC during the adsorption process.

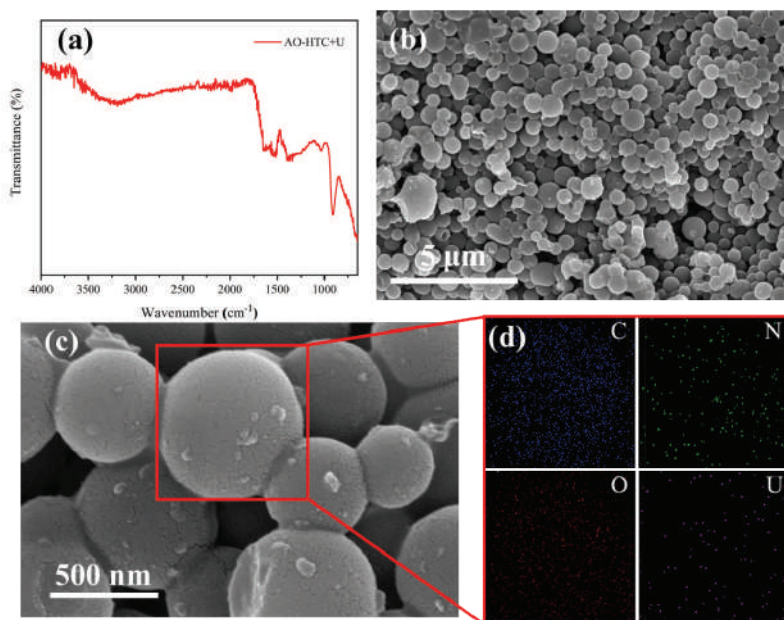


Figure 5. The FT-IR spectra (a), SEM images (b-c) and elemental mapping (d) of the post-sorption of U(VI) on AO-HTC.

Conclusion

In this study, a novel adsorbent is synthesized by amidoxime-functionalized HTC using a common, commercially available, inexpensive raw material and a simple, mild preparation process. It was characterized by SEM, FT-IR, BET and Elemental analysis. The results of AO-HTC adsorption of uranium showed that the adsorption was negatively correlated with pH, total carbonic acid concentration, calcium ion concentration and humic acid

concentration. The results of influencing factors such as contact time, initial uranium concentration and temperature indicate that the adsorption of U(VI) on AO-HTC is a pH-dependent, endothermic, spontaneous and pseudo second-order process. The AO-HTC adsorbent exhibited excellent reusability without significant changes in the adsorption capacity and structural stability after five cycles. The novel AO-HTC adsorbent has broad application prospects in uranium separation from radioactive groundwater and

other related water sources.

Acknowledgments: This work was financially supported by the National Natural Science Foundation of China (21561002, 21866004, 21866003).

References

- [1] B. Kornilovych, M. Wireman, S. Ubaldini, D. Guglietta, Y. Koshik, B. Caruso and I. Kovalchuk, *Metals*, 2018, 8,408
- [2] A. A. H. Faisal and Z. A. Hmood, *Desalination and Water Treatment*, 2015, 53, 1377-1386.
- [3] F. Obiri-Nyarko, S. J. Grajales-Mesa and G. Malina, *Chemosphere*, 2014, 111, 243-259.
- [4] X. Liu, J. Sun, X. Xu, A. Alsaedi, T. Hayat and J. Li, *Chem. Eng. J.*, 2019, 360, 941-950.
- [5] M. Jimenez-Reyes and M. Solache-Rios, *Water Air and Soil Pollution*, 2018, 229.
- [6] Z. B. Zhang, J. Liu, X. H. Cao, X. P. Luo, R. Hua, Y. Liu, X. F. Yu, L. K. He and Y. H. Liu, *J. Hazard. Mater.*, 2015, 300, 633-642.
- [7] X. Han, Y. Wang, X. Cao, Y. Dai, Y. Liu, Z. Dong, Z. Zhang and Y. Liu, *Appl. Surf. Sci.*, 2019, 484, 1035-1040.
- [8] J. Yang, M. Ge, Q. Jin, Z. Chen and Z. Guo, *Chemosphere*, 2019, 231, 405-414.
- [9] H. Tu, T. Lan, G. Yuan, C. Zhao, J. Liu, F. Li, J. Yang, J. Liao, Y. Yang, D. Wang and N. Liu, *Journal of Environmental Radioactivity*, 2019, 197, 23-29.
- [10] S. Lu, K. Zhu, H. Guo, H. Wang, N. Zhang, A. Alsaedi, T. Hayat, Y. Li and Y. Sun, *Chem. Eng. J.*, 2019, 368, 598-605.
- [11] D. K. Gupta, A. V. Voronina, V. S. Semenishchev and S. Chatterjee, in *Green Adsorbents for Pollutant Removal: Innovative Materials*, eds. G. Crini and E. Lichtfouse, 2018, vol. 19, pp. 377-396.
- [12] X. Wang, S. Yu, Y. Wu, H. Pang, S. Yu, Z. Chen, J. Hou, A. Alsaedi, T. Hayat and S. Wang, *Chem. Eng. J.*, 2018, 342, 321-330.
- [13] C. Chen, K. Zhao, J. Shang, C. Liu, J. Wang, Z. Yan, K. Liu and W. Wu, *Environ. Pollut.*, 2018, 240, 219-226.
- [14] Y. Zou, X. Wang, F. Wu, S. Yu, Y. Hu, W. Song, Y. Liu, H. Wang, T. Hayat and X. Wang, *ACS Sustainable Chemistry & Engineering*, 2017, 5, 1173-1185.
- [15] P. Li, J. Wang, Y. Wang, J. Liang, B. He, D. Pan, Q. Fan and X. Wang, *Chem. Eng. J.*, 2019, 365, 231-241.
- [16] W. Li, Q. Liu, R. Chen, J. Yu, H. Zhang, J. Liu, R. Li, M. Zhang, P. Liu and J. Wang, *Inorganic Chemistry Frontiers*, 2018, 5, 1321-1328.
- [17] H. Basu, S. Saha, M. V. Pimple and R. K. Singhal, *Journal of Environmental Chemical Engineering*, 2019, 7,103-110
- [18] Z. Zeng, Y. Wei, L. Shen and D. Hua, *Industrial & Engineering Chemistry Research*, 2015, 54, 8699-8705.
- [19] S. H. Choi, M. S. Choi, Y. T. Park, K. P. Lee and H. D. Kang, *Radiat. Phys. Chem.*, 2003, 67, 387-390.
- [20] Y. Yuan, S. Zhao, J. Wen, D. Wang, X. Gu, L. Xu, X. Wang and N. Wang, *Adv. Funct. Mater.*, 2019, 29,2
- [21] Z. Zhang, Z. Dong, Y. Dai, S. Xiao, X. Cao, Y. Liu, W. Guo, M. Luo and Z. Le, *RSC Adv.*, 2016, 6, 102462-102471.
- [22] Z. Zhang, Z. Dong, X. Wang, D. Ying, F. Niu, X. Cao, Y. Wang, R. Hua, Y. Liu and X. Wang, *Chem. Eng. J.*, 2018, 341, 208-217.
- [23] M. Monier, D. A. Abdel-Latif and H. A. Mohammed, *International Journal of Biological Macromolecules*, 2015, 75, 354-363.
- [24] X. Lu, S. He, D. Zhang, A. T. Reda, C. Liu, J. Feng and Z. Yang, *RSC Adv.*, 2016, 6, 101087-101097.
- [25] R. Coskun and C. Soykan, *Journal of Applied Polymer Science*, 2009, 112, 1798-1807.
- [26] Y.-Q. Wang, Z.-B. Zhang, Y.-H. Liu, X.-H. Cao, Y.-T. Liu and Q. Li, *Chem. Eng. J.*, 2012, 198, 246-253.
- [27] Y. Liu, Q. Li, X. Cao, Y. Wang, X. Jiang, M. Li, M. Hua and Z. Zhang, *Appl. Surf. Sci.*, 2013, 285, 258-266.
- [28] Z.-p. Cheng, Y.-h. Liu, G.-x. Xiong, X.-p. Luo, X.-h. Cao, M. Li and Z.-b. Zhang, *J. Radioanal. Nucl. Chem.*, 2015, 306, 365-375.
- [29] A. Mellah, S. Chegrouche and M. Barkat, *Journal of Colloid and Interface Science*, 2006, 296, 434-441.
- [30] C. Y. Xie, S. P. Jing, Y. Wang, X. Lin, H. L. Bao, C. Z. Guan, C. Jin and J. Q. Wang, *Nucl. Sci. Tech.*, 2017, 28, 8.
- [31] S. Duan, X. Xu, X. Liu, Y. Wang, T. Hayat, A. Alsaedi, Y. Meng and J. Li, *Journal of Colloid and Interface Science*, 2018, 513, 92-103.
- [32] G. Tian, J. Geng, Y. Jin, C. Wang, S. Li, Z. Chen, H. Wang, Y. Zhao and S. Li, *J. Hazard. Mater.*, 2011, 190, 442-450.
- [33] Y.-H. Liu, Y.-Q. Wang, Z.-B. Zhang, X.-H. Cao, W.-B. Nie, Q. Li and R. Hua, *Appl. Surf. Sci.*, 2013, 273, 68-74.
- [34] A. S. Kar, A. Saha, A. Chandane, S. Kumar and B. S. Tomar, *Radiochimica Acta*, 2018, 106, 191-205.
- [35] Y. Zhang, Y. Li, Y. Ning, D. Liu, P. Tang, Z. Yang, Y. Lu and X. Wang, *Water Science and Technology*, 2018, 77, 920-930.
- [36] J. Hui, Y. Wang, Y. Liu, X. Cao, Z. Zhang, Y. Dai and Y. Liu, *J. Radioanal. Nucl. Chem.*, 2019, 319, 1251-1259.
- [37] E. Prasetyo, *Mineral Processing and Technology International Conference*, 2018, 285,012011
- [38] T. Lan, J. Liao, Y. Yang, Z. Chai, N. Liu and D. Wang, *Environ. Sci. Technol.*, 2019, 53, 5102-5110.
- [39] L. Liu, J. Liu, X. Liu, C. Dai, Z. Zhang, W. Song and Y. Chu, *Journal of Environmental Radioactivity*, 2019, 203, 117-124.
- [40] F. Meng, G. Yuan, S. L. Larson, J. H. Ballard, J. R. White, Z. Arslan and F. X. Han, *International Journal of Environmental Research and Public Health*, 2019, 16,9
- [41] Y.-Q. Wang, Z.-b. Zhang, Q. Li and Y.-H. Liu, *J. Radioanal. Nucl. Chem.*, 2012, 293, 231-239.
- [42] Z. Zhang, Z. Dong, X. Wang, Y. Dai, X. Cao, Y. Wang, R. Hua, H. Feng, J. Chen, Y. Liu, B. Hu and X. Wang, *Chem. Eng. J.*, 2019, 370, 1376-1387.
- [43] S. Song, S. Zhang, S. Huang, R. Zhang, L. Yin, Y. Hu, T. Wen, L. Zhuang, B. Hu and X. Wang, *Chem. Eng. J.*, 2019, 355, 697-709.
- [44] X. Yang, J. Li, J. Liu, Y. Tian, B. Li, K. Cao, S. Liu, M. Hou, S. Li and L. Ma, *J. Mater. Chem. A*, 2014, 2, 1550-1559.

Preparation of cobalt ferrite nanoparticles using fulvic acid as a capping agent and its effect on catalytic activity

Jinxing LI¹, Abdelrahman A. Badawy², Guanben DU¹, Xiaojian ZHOU^{1*}, Hisham A. Essawy^{3*}

1 Yunnan Provincial Key Laboratory of Wood Adhesives and Glued Products, Southwest Forestry University, China.

2 Physical Chemistry Department, National Research Centre, 33 El Behooth St., Dokki Giza, Egypt.

3 Department of Polymers and Pigments, National Research Centre, Dokki 12622, Cairo, Egypt.

***Corresponding Author:** Xiaojian ZHOU, No. 300, Panlong District, Kunming, 650224, China, email: xiaojianzhou@hotmail.com; Hisham Essawy, Egypt Research Center, Cairo, Egypt, email: hishamessawy@yahoo.com

Abstract:

Cobalt ferrite was prepared by co-precipitation from cobalt and iron soluble precursors in presence of fulvic acid at different pH values, namely, 6 and 8 and compared with the same preparation in absence of fulvic acid. The presence of fulvic acid is expected to bind metal ions through bridging before co-precipitation and mineralization. The extent of binding is determined according to the pH of the process. This influences the mineralization of the resulting cobalt ferrite and the crystallization/ordering of its lattice. In addition, the extent of residual ferric oxide is also a function of the efficiency of binding process. This route of modification for the co-precipitation process was found to be accompanied by enhanced surface area and total pore volume for most of the prepared samples. The involvement of these oxides as catalysts in the photo-catalytic degradation of phenol from wastewater was found to contribute very efficiently and the removal reached about 88% in some cases, which can be attributed to olation and oxolation process of the formed nanoparticles.

Keywords: nanostructured materials; precipitation; oxidation; X-ray diffraction

1. Introduction

The surface and catalytic activity of mixed metal oxides are mainly dominated by the methods of preparation and calcination conditions^[1-4]. Mixed oxides are mostly prepared to merge some properties that cannot be gained from single oxide. The development of new active compounds that can contribute to several fields of applications is a direct result for this merge of properties.

The very attractive properties of nanometric structures derived from metal oxides made them receiving great attention as promising materials for fields such as catalysis and adsorption^[4-8]. Some reports in the open literature dealt with the adsorption of different dyes to surfaces such as iron oxides^[9, 10].

Fabrication of adsorbents with controlled features like the size and crystallinity is a challenging task. Thus, the preparation procedure can have a major influence in terms of the chemical composition and microstructure. Co-precipitation is a facile method among those that have been employed for preparation of catalysts. It is favored because it leads to homogenous catalysts from the

chemical point of view thereby both the surface and bulk of the prepared catalysts can contribute to catalytic course. These advantages made this method widely applicable to catalysts dedicated for performance under high pressure and moderate temperature^[11-14]. As an example, the ferrites fabricated via the co-precipitation route acquired a non-aggregated and uniform structure^[11-20]. Many studies explored the consequence of using some organic compounds on the coprecipitation process of metal ferrites^[21-25]. Among them, polyvinyl pyrrolidone (PVP) was added as capping agent during the course of coprecipitation of cobalt ferrite^[21]. Essawy and co-workers^[26-28] used fulvic acid in the preparation of polymeric superabsorbents to pass on reinforcement and functionalization to the resulting structures. This provoked elevation of the chemical activity especially the chelation potential^[26]. The high functionality and elevated binding capacity of fulvic acid to metal ions allowed their role as templates through the synthesis of metal oxides starting from nitrate precursors via coprecipitation^[7,8]. This progresses via initial coprecipitation in the form of metal hydroxides in existence of fulvic acid and the

desired oxides are finally obtained by calcination at high temperatures. Grouping a number of precursors of metal ions in presence of fulvic acid would be expected to result in homogenous metal oxides exhibiting variation in their composition and characteristics [26-28].

Phenol is commonly used as a raw material for the preparation of many products. This includes pesticides, pharmaceuticals, resins and many others. Nevertheless, it is toxic, carcinogenic, and non-biodegradable [29-32].

Pollution of water sources became a parallel fact to the numerous industrial activities. This necessitates the great need to take care of these pollutants prior to their transport into plants of wastewater treatment. Highly developed oxidation techniques are suggested deal with the organic contaminants present in water [33, 34]. Rigorous efforts are devoted to improve these technologies by changing the catalytic system or the oxidizing agent. Nevertheless, using catalysts that belong to oxidizing reagents in liquid phase may elevate this contamination.

The ongoing study is an effort to obtain nanometric mixed metal oxides incorporating iron and cobalt while revealing a wide range of surface characteristics and chemical composition following modified co-precipitation method of nitrate precursors in solution by employing sodium hydroxide in existence of fulvic acid at pH 6 and 8. This is expected to provide control over the rates of co-precipitation and hence changeable mineralization and ordering of the prepared mixed oxides. The use of such metal oxides as advanced oxidants in the solid form to stop any further contamination to the water through their catalytic cycle is also among the purposes of this study. The work will be also extended to their application in the photocatalytic removal of phenol from wastewater.

2. Experimental

2.1 Materials and methods

Fulvic acid was supplied from Changsha Xian Shan Yuan Agriculture Technology Co., China. Cobalt nitrate and ferric nitrate were purchased from Sigma-Aldrich, Germany. Phenol aqueous solution (80%, w/w) was obtained from BDH Chemicals, England. Otherwise, the rest were analytical grade chemicals that were used with no further purification.

2.2 Preparation of metal oxide nanoparticles via coprecipitation process

The wet chemical co-precipitation procedure was involved in the preparation of Cobalt ferrite (CoFe_2O_4) [12]. Nitrates of cobalt and iron were dissolved in distilled water at a certain molar ratio ($\text{Fe}/\text{Co}=2$) while sodium hydroxide solution (1M) was used for the precipitation. The nitrate solutions and sodium hydroxide were mixed in existence of fulvic acid. The mixing was accomplished via drop wise addition from 3 different burettes into a collective vessel containing 1000 mL distilled water while continuous stirring was kept running. The dropping rate was managed in such a way to keep the pH (6 or 8) and the temperature (70 °C)

unchanged during the co-precipitation. The precipitate was rinsed with distilled water several times to get rid of NO_3^- and Na^+ ions. Filtration was undertaken followed by overnight drying at 100 °C. Lattice formation of the oxides was targeted by calcination at 700 °C for 4h. Thus, for simplicity, the sample prepared at pH 6 in absence of fulvic acid is denoted as P6 while F6 designates the same when fulvic acid was included in the recipe. Similarly, P8 reveals the coprecipitation performed at pH 8 in absence of fulvic acid whereas F8 indicates the equivalent sample prepared in existence of fulvic acid F8.

2.3 Measurements

X-ray diffractograms of the solids obtained by calcination at 700 °C were collected using Bruker diffractometer (D 8 advance target) with CuK_α secondly monochromator ($\lambda = 1.5405 \text{ \AA}$), operated at 40 kV and 40 mA, at a scanning rate of $0.8^\circ 2\theta \text{ min}^{-1}$ for phase identification and line broadening. The crystallite size of each phase calculated by Scherrer equation (Eq. 1):

$$d = K \lambda / \beta_{1/2} \cos \theta \quad (1)$$

Where d represents the mean crystalline diameter, λ is the wavelength of x-rays, K is the Scherrer constant (0.89), $\beta_{1/2}$ is the full width at half maximum (FWHM) of the main peaks of diffraction and θ is the angle of diffraction.

The morphology and surface structure of the oxides were imaged by JEOL JEM-1230 transmission electron microscope (TEM) coupled with JEOL-SEM scanning electron microscope (SEM) operated at acceleration voltage of 80 kV.

The properties of the surface were investigated by undertaking adsorption of nitrogen gas at 350 °C using Quantochrome ASI WinTM- automated gas-sorption apparatus (USA). The samples were degassed at 200 °C for 2 h prior to the adsorption processes then the specific surface area (S_{BET}) was estimated by applying Brunauer–Emmett–Teller (BET) equation. On the hand, the pore size distribution was evaluated from the desorption part of the isotherm using the standard method.

The catalytic removal of phenol from wastewater was undertaken by suspending 1 g of mixed oxide in a glass reactor containing 100 mL of distilled water and 100 ppm of phenol and immersed in water bath fitted with temperature controller. Shaking on the solution was applied continuously at 150 rpm and 25 °C for up to 4 h.

For evaluation of the concentrations of residual phenol in wastewater, 5 mL suspension was withdrawn from the reactor and centrifuged for 10 min before recording the absorbance was performed at 270 nm using a calibrated UV-VIS spectrophotometer (UV-VIS-NIR-3101 PC, Shimadzu) [35]. The removal efficiency of phenol was assessed as average of three readings and applying Eq. 2:

$$\text{Removal, \%} = ((A^\circ - A) / (A^\circ)) \times 100 \quad (2)$$

Where A° and A are the absorbance of the blank and sample, respectively. According to Beer-Lambert's law, A° and A are proportional to C° and C , which refer to the concentrations of the blank and sample at time t [35].

3. Results and discussion

The X-ray diffractograms of mixed oxides prepared in presence and absence of fulvic acid before calcination at 700 °C are displayed in Figure 1 and summarized in Table 1.

Table 1. The effect of fulvic acid on the peak intensity of the main diffraction lines of Fe_2O_3 and CoFe_2O_4 along with their crystallite size .

Sample	Intensity (a.u.) of diffraction peaks for Fe_2O_3 and CoFe_2O_4		size of Fe_2O_3 and CoFe_2O_4 Crystallites (nm)	
	Fe_2O_3	CoFe_2O_4	Fe_2O_3	CoFe_2O_4
P6	130	106	93.3	72.8
P8	-	95.6	-	26.5
F6	-	66.8	-	23.4
F8	85.4	74.6	70.5	55.2

It is obvious from Figure 1 that the coprecipitation achieved at pH 6 in absence of fulvic acid (P6) took place with a portion of Fe_2O_3 not taking part in the reaction ($2\theta = 33^\circ$) whereas cobalt ferrite ($2\theta = 35^\circ$) was the major phase. When fulvic acid was involved in the process (F6), it propagated without formation of Fe_2O_3 while at pH 8, in absence of fulvic acid (P8), CoFe_2O_4 was born as a sole phase with high crystallinity (95.6 a.u.). Interestingly, at pH 8 the presence of fulvic acid (F8) led to birth of both Fe_2O_3 and CoFe_2O_4 .

Table 1 signifies that the existence of fulvic acid at pH 8 (F8) gave rise to formation of nanometric Fe_2O_3 as a main component along with CoFe_2O_4 that underwent a two-fold increase in the crystallite size (55.2 nm) in comparison to the same procedure in absence of fulvic acid (26.5 nm, P8). The increase was accompanied by a visible decline in the crystallinity of CoFe_2O_4 (74.6 a.u.).

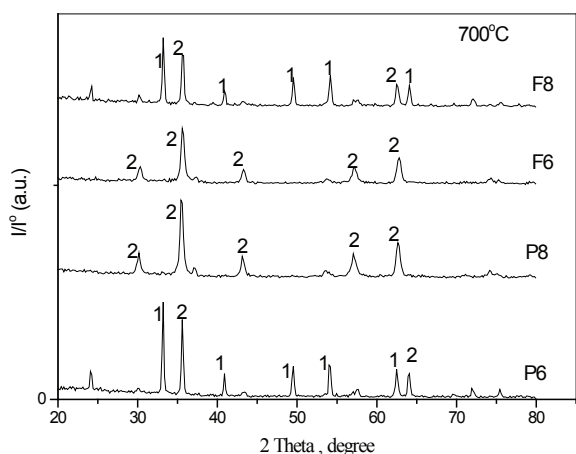
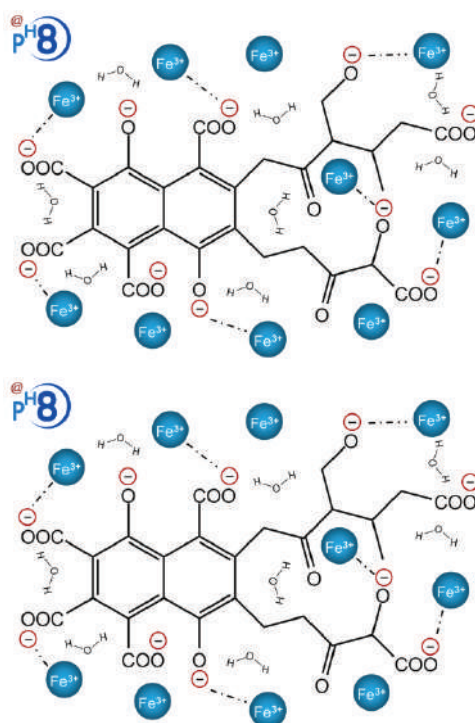


Figure 1. X-ray diffraction profiles for products of coprecipitations undertaken with and without fulvic acid after calcination at 700 °C; 1 indicates Fe_2O_3 , 2 indicates CoFe_2O_4 .

The observed significant high crystallite size of CoFe_2O_4 in case of F6 might have resulted from a considerable decline in the degree of dispersion of CoFe_2O_4 in its crystal lattice [1]. As so, CoFe_2O_4 is known with its catalytic activity while in this case the lack of distribution over its crystal lattice is expected to bring about a major drop in its catalytic activity, which was actually the case as will be shown in the next parts.

This could be better understood by the illustration presented in scheme 1 which shows that at pH 6, the fulvic acid present in a protonated form. Thus, the conditions are not appropriate for coordination of Fe^{3+} and Co^{2+} by fulvic acid. Opposite trend was encountered at pH 8 in which strong interaction developed between Fe^{3+} ions and the oxygenated and carboxylate sites. This suggests that this process might be dominated by the tendency of ferric hydroxide to precipitate first, which is harmonizing with the considerable variation in the solubility product values of the hydroxide precursors; 5.92×10^{-15} and 2.79×10^{-39} for cobalt and ferric ions, respectively. Accordingly, the fulvic acid is thought to have capped the ferric ions while another portion of ferric ions was involved in the construction of the uniformly distributed solid phase of cobalt ferrite as a result of calcination. During this process the organic material (fulvic acid) has been totally removed by calcination whereas Fe_2O_3 developed progressively phase. From Table 1, we can notice that particle size of Fe_2O_3 increases by the presence of fulvic acid. This may be ascribed to many close particles combine together and contribute to the particle size increase by melting of their surfaces [36].



Scheme 1. A suggested mechanism of involving interactions between fulvic acid and ferric ions at pH 6 and 8 prior to calcinations.

These findings were supported from high resolution transmission electron microscopy images (Figure 2 a-d). Figure 2a indicates the presence of two different groups of particles; one exhibits a size of 69-85 nm while the other one acquired a size between 22-28 nm. The inset of this image confirms that the heterogeneity of the electron diffraction is high which indicates incomplete mineralization of CoFe_2O_4 (XRD of P6, Figure 1). On the other hand, Figure 2 c ensures that the presence of fulvic acid (F6) caused drop in the overall crystallinity of the formed CoFe_2O_4 despite the complete coprecipitation reaction which leads to effective mineralization. Further, the electron diffraction shows no obvious change in the heterogeneity feature (inset of Figure 2 c).

Figure 2 b, d gives rise to the interesting feature

induced by existence of fulvic acid in the coprecipitation course whereupon the overall ordering became more homogenous (inset of Figure 2d) as compared to the same product in absence of the fulvic acid (inset of Figure 2b). In addition all the formed crystals were in the nanometric scale.

Therefore, it is noticeable that the size of crystallites and of crystallinity degree are very much dependent on the pH of the medium during precipitation and the presence a capping agent such as fulvic acid. This is in full accordance with earlier studies, which showed that fulvic acid can be involved in different ways during the coprecipitation due to its variable binding potential to metal ions at different pH values [35, 37].

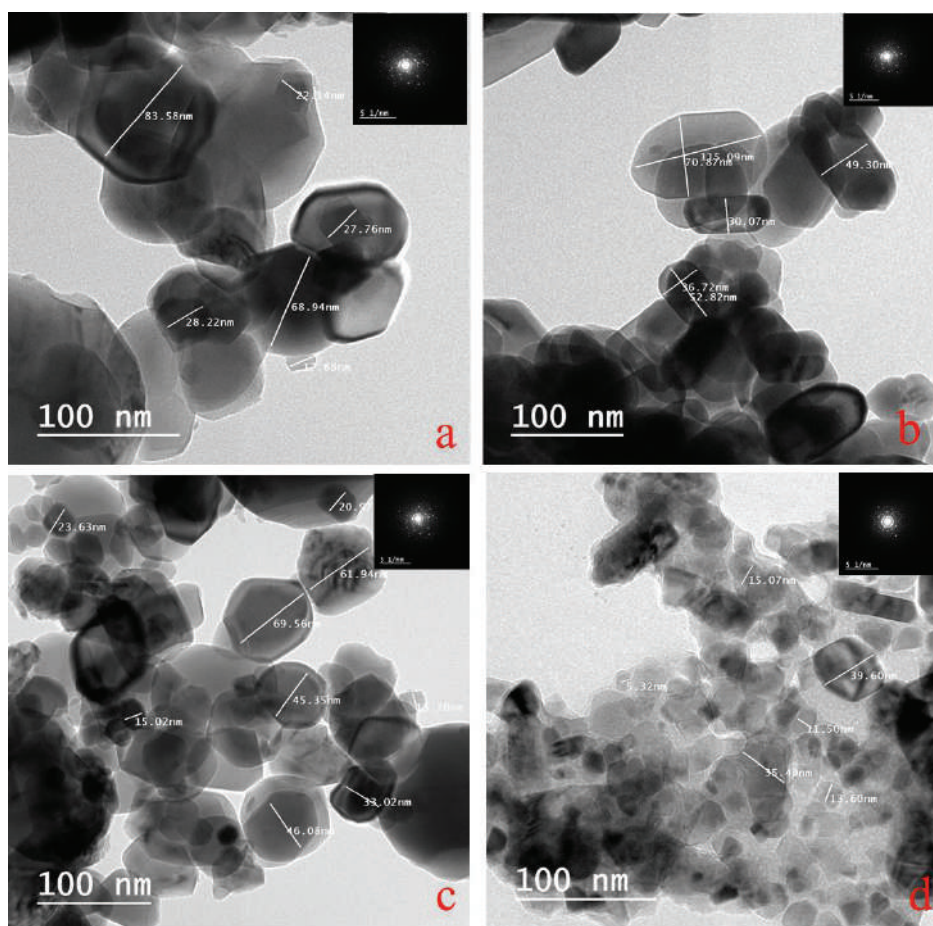


Figure 2. High resolution transmission electron microscopy (HRTEM) imaging of, a: P6, b: P8, c: F6 and d: F8 after calcination at 700 °C.

Table 2. Surface properties of the solids emerged from the various recipes after calcination at 700 °C.

Sample	S_{BET} (m^2/g)	total pore volume V_p (cc/g)	mean pore radius r (nm)
P6	7.3	0.06	164.4
P8	20.7	0.03	29.0
F6	11.4	0.01	17.5
F8	13.9	0.02	28.8

Investigation of the surface properties for the prepared solids were accomplished by nitrogen gas adsorption-desorption as clear from Figure 3 and Table 2. It can be easily recognized that the involvement of fulvic acid at pH 6 (F6) caused a substantial increase in S_{BET} (56%) as compared to P6. This can be accounted for by the associated drop in r

(Table 2). On the other hand, the practical decrease of S_{BET} in existence of fulvic at pH 8 (F8) in comparison with P8, in which the fulvic acid was absent, can be justified by the domination of the increase in the crystallite size of $CoFe_2O_4$ (Table 1)

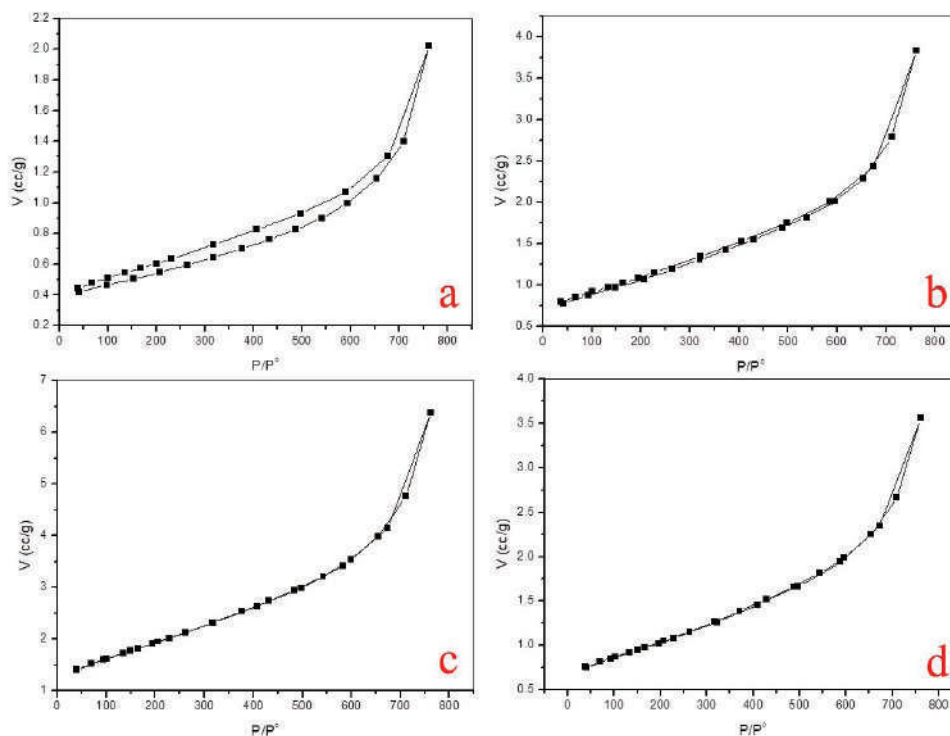
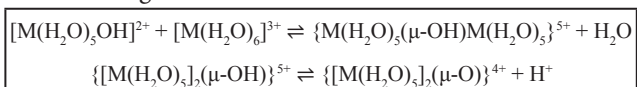


Figure 3. Corresponding nitrogen gas adsorption-desorption isotherms for the solids obtained by calcination at 700 °C; a:P6, b: P8, c:F6 and d: F8.

This was motivating for us to carry out a preliminary photocatalytic study and employ the prepared metal oxides as catalysts during the photocatalytic degradation of phenol present in wastewater. Fig. 4 demonstrates an interesting catalytic action that increases progressively with the time and reaches 88% and 75% after 3h in case of F8 and P6, respectively. The catalytic efficiency can be arranged in the following order: $F8 > P6 > P8 > F6$. The elevated catalytic activity of F8 and P6 with respect to the other formulations (P8 and F6) can be explained by a joint catalytic action of $CoFe_2O_4$ and Fe_2O_3 , which was not the case for P8 and F6. This may refer to enhancement of the catalytic power of $CoFe_2O_4$ by Fe_2O_3 . This behavior might be attributed to olation of both metal ions in the form of hydroxides that could be survived during the calcination process. The olation-based structure exhibited oxolation during their employment in photocatalytic reactions which provides hydrogen ions that are able to combine with the phenol and causes its degradable as shown in scheme 2 [38-41].



Scheme 2. Chemical reactions illustrating the formation of olation-oxolation structure.

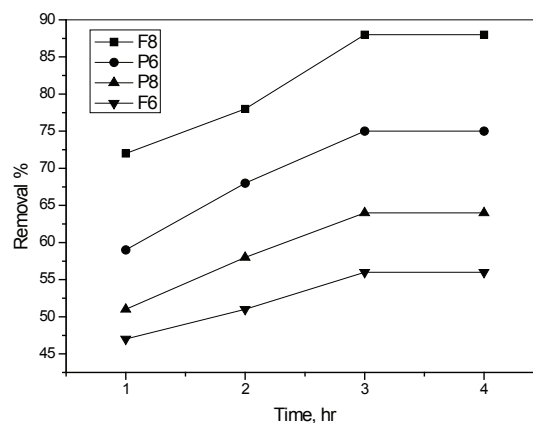


Figure 4. Photocatalytic removal efficiency of phenol using metal oxides prepared by calcination at 700°C.

4. Conclusions

Highly ordered cobalt ferrite can be prepared by modified coprecipitation process starting from cobalt nitrate and ferric nitrate in existence of fulvic acid at different pH

values. Fulvic acid exhibits high coordination potential to the starting metal ions during the co-precipitation process. This provides control over the extent of mineralization and the crystallization/ordering of the resulting cobalt ferrite lattice. The control over the co-precipitation can contribute efficiently to the surface area and porosity which made these mixed oxides liable for catalytic applications. The use of the different forms of these oxides as catalysts in the photocatalytic degradation of phenol present in wastewater gives pronouncing levels of removal which reached 88%. This can be accounted for by enhancement of the photocatalytic activity as a result of combination of cobalt ferrite and ferric oxide in a structure exhibiting ololation and oxolation.

Author Contributions: Jinxing LI and Dr. Abdelrahman A. Badawy as first author contributed equally to this work, finalize the experiment and gave the ideas. Prof. Xiaojian Zhou and Prof. Hisham A. Essawy, both are the responding author, responsible for whole manuscript.

Acknowledgment: The authors highly appreciate “Yunnan Provincial Reserve Talents for Middle & Young Academic and Technical Leaders (2019HB026)” and “Ten-thousand Program”-youth talent support program”, and the financial support from the administration of the National Research Centre- Egypt, as well as grant No.111814.

References

- [1] El-Shobaky GA, El-Shobaky HG, Badawy AA, Mohamed GM, Effect of Li_2O -doping on physicochemical, surface and catalytic properties of nanosized $\text{CuO-Mn}_2\text{O}_3/\text{cordierite}$ system. *Materials Chemistry and Physics* 2002; 136(2-3):1143-1147.
- [2] El-Shobaky GA, El-Shobaky HG, Badawy AA et al. Physicochemical, surface and catalytic properties of nanosized copper and manganese oxides supported on cordierite. *Applied Catalysis A: General* 2011; 409:234-238.
- [3] Badawy AA, Ibrahim ShM. The influence of La_2O_3 -doping on structural, surface and catalytic properties of nanosized cobalt–manganese mixed oxides. *International Journal of Industrial Chemistry* 2016;7(3):287-296.
- [4] Reddy LH, Arias JL, Nicolas J. et al. Magnetic nanoparticles: design and characterization, toxicity and biocompatibility, pharmaceutical and biomedical applications. *Chemical Reviews* 2012; 112(11):5818-5878.
- [5] Huggins FE, Bali S, Huffman, GP et al. Iron-oxide aerogel and xerogel catalyst formulations: Characterization by 57Fe Mössbauer and XAFS spectroscopies. *Spectrochimica Acta Part A: Molecular and Biomolecular Spectroscopy* 2010; 76(1):74-83.
- [6] Zhong, D.K., Sun, J.W., Inumaru, H., Gamelin, D.R., 2009. Solar water oxidation by Composite Catalyst/ $\alpha\text{-Fe}_2\text{O}_3$ Photoanodes. *Journal of the American Chemical Society*, 131(17), pp. 6086-6087.
- [7] Zhang YZ, He HP, Ye ZZ, et al. Preparation and photoluminescent properties of p-type Li-doped ZnMgO thin films. *Materials Letters* 2008; 62(8-9):1418-1420.
- [8] Tang H, Zhou WJ, Lu A, et al. Characterization of new sorbent constructed from $\text{Fe}_3\text{O}_4/\text{chitin}$ magnetic beads for the dynamic adsorption of Cd^{2+} ions. *Journal of Materials Science* 2014; 49(1):123-133.
- [9] Mahapatra A, Mishra BG, Hota G. Adsorptive removal of Congo red dye from wastewater by mixed iron oxide–alumina nanocomposites. *Ceramics International* 2013; 39(5):5443-5451.
- [10] Zhang X, Zhang PY, Wu Z. Adsorption of methylene blue onto humic acid-coated Fe_3O_4 nanoparticles. *Colloids and Surfaces A: Physicochemical and Engineering Aspects* 2013; 435:85-90.
- [11] Kumar P, Sharma SK, Knobel M. et al. Effect of La^{3+} doping on the electric, dielectric and magnetic properties of cobalt ferrite processed by co-precipitation technique. *Journal of Alloys and Compounds* 2010; 508(1):115-118.
- [12] Fagal GA, Badawy AA, Hassan NA. et al. Effect of La_2O_3 -treatment on textural and solid–solid interactions in ferric/cobaltic oxides system. *Journal of Solid State Chemistry* 2012; 194:162-167.
- [13] Khandekar MS, Kambale RC, Patil JY, et al. Effect of calcination temperature on the structural and electrical properties of cobalt ferrite synthesized by combustion method. *Journal of Alloys and Compounds* 2011; 509(5):1861-1865.
- [14] Zhou J, Ma J, Sun C, et al. Low temperature synthesis of NiFe_2O_4 by a hydrothermal method. *Journal of the American Ceramic Society* 2005; 88(12):3535-3537.
- [15] Peng L, Qin P, Lei M, et al. Modifying Fe_3O_4 nanoparticles with humic acid for removal of Rhodamine B in water. *Journal of Hazardous Materials* 2012; 209:193-198.
- [16] Illés E, Tombácz E. The effect of humic acid adsorption on pH-dependent surface charging and aggregation of magnetite nanoparticles. *Journal of Colloid and Interface Science* 2006; 295(1):115-123.
- [17] Mondal S, Methods of dye removal from dye house effluent-an overview. *Environmental Engineering Science* 2008; 25(3): 383-396.
- [18] Berneth H, Azine Dyes. *Ullmann's Encyclopedia of Industrial Chemistry* 2005.
- [19] Program NT, Toxicology and carcinogenesis studies of methylene blue trihydrate (Cas No. 7220-79-3) in F344/N rats and B6C3F1 mice (gavage studies). *National Toxicology Program Technical Report Series* 2008; 540:1.
- [20] Sharma YC, Uma Upadhyay SN, An economically viable removal of methylene blue by adsorption on activated carbon prepared from rice husk. *The Canadian Journal of Chemical Engineering* 2011; 89(2):377-383.
- [21] Naseri MG, Saion EB, Ahangar HA, et al. Simple synthesis

- and characterization of cobalt Ferrite nanoparticles by a thermal treatment method. *Journal of Nanomaterials* 2010; 75:1-8.
- [22] Calero-Ddelc VL, Rinaldi C. Synthesis and magnetic characterization of cobalt-substituted ferrite ($\text{Co}_x\text{Fe}_{3-x}\text{O}_4$) nanoparticles. *Journal of Magnetism and Magnetic Materials* 2007; 314(1):60-67.
- [23] Chen L, Shen Y, Bai J. Large-scale synthesis of uniform spinel ferrite nanoparticles from hydrothermal decomposition of trinuclear heterometallic oxo-centered acetate clusters. *Materials Letters* 2009; 63(12):1099-1101.
- [24] Zarnega Z, Safari J. Modified chemical coprecipitation of magnetic magnetite nanoparticles using linear-dendritic copolymers. *Green Chemistry Letters and Reviews* 2017; 10(4):235-240.
- [25] Gharagozlou M. Synthesis, characterization and influence of calcination temperature on magnetic properties of nanocrystalline spinel Co-ferrite prepared by polymeric precursor method. *Journal of Alloys and Compounds* 2009; 486(1-2):660-665.
- [26] Essawy HA, Mohamed MF, Ammar NS, et al. Potassium fulvate-functionalized graft copolymer of polyacrylic acid from cellulose as a promising selective chelating sorbent. *RSC Advances* 2017; 7(33):20178-20185.
- [27] Mohamed MF, Essawy HA, Ammar NS, et al. Potassium fulvate-modified graft copolymer of acrylic acid onto cellulose as efficient chelating polymeric sorbent. *International Journal of Biological Macromolecules* 2017; 94:771-780.
- [28] Essawy HA, Mohamed MF, Ammar NS, et al. The promise of a specially-designed graft copolymer of acrylic acid onto cellulose as selective sorbent for heavy metal ions. *International Journal of Biological Macromolecules* 2017; 103:261-267.
- [29] Park Y, Ayoko GA, Kurdi R, et al. Adsorption of phenolic compounds by organoclays: Implications for the removal of organic pollutants from aqueous media. *Journal of Colloid and Interface Science* 2013; 406:196-208.
- [30] Amin NAS, Akhtar J, Rai HK. Screening of combined zeolite-ozone system for phenol and COD removal. *Chemical Engineering Journal* 2010; 158(3):520-527.
- [31] Hsu YC, Chen JH, Yang HC. Calcium enhanced COD removal for the ozonation of phenol solution, *Water Research* 2007; 41(1):71-78.
- [32] Busca G, Berardinelli S, Resini C, et al. Technologies for the removal of phenol from fluid streams: A short review of recent developments. *Journal of Hazardous Materials* 2008; 160(2-3):265-288.
- [33] AbdelRehim MH, El-Samahy MA, Badawy AA, et al. Photocatalytic activity and antimicrobial properties of paper sheets modified with TiO_2 /sodium alginate nanocomposites. *Carbohydrate Polymers* 2016; 148:194-199.
- [34] Ghanem AF, Badawy AA, Ismail N, et al. Photocatalytic activity of hyperbranched polyester/ TiO_2 nanocomposites. *Applied Catalysis A: General* 2014; 472:191-197.
- [35] Xie J, Meng W, Wu D, et al. Removal of organic pollutants by surfactant modified zeolite: Comparison between ionizable phenolic compounds and non-ionizable organic compounds. *Journal of Hazardous Materials* 2012; 231-232:57-63.
- [36] Mikutta C, Kretzschmar R. Synthetic coprecipitates of exopoly-saccharides and ferrihydrite. Part II: Siderophore-promoted dissolution. *Geochimica et Cosmochimica Acta* 2008; 72(4):1128-1142.
- [37] Yang R, Li Z, Huang B, et al. Effects of Fe(III)-fulvic acid on Cu removal via adsorption versus coprecipitation. *Chemosphere* 2018; 197:291-298.
- [38] Pechenyuk SI, Semushin VV, Kashulina TG. Aging of oxyhydroxide sorbents saturated with the cations of nonferrous metals. *Chemistry for Sustainable Development* 2003; (11): 627-633.
- [39] Jiang L, Mao X. Degradation of phenol-containing wastewater using an improved electro-fenton process. *International Journal of Electrochemical Science* 2012; 7:4078-4088.
- [40] Qu Y, Yang H, Yang N, et al. The effect of reaction temperature on the particle size, structure and magnetic properties of coprecipitated CoFe_2O_4 nanoparticles. *Materials Letters* 2006; 60(29-30):3548-3552.
- [41] Marques Neto JO, Bellato CR, de Souza CHF, et al. Synthesis, Characterization and Enhanced Photocatalytic Activity of Iron Oxide/Carbon Nanotube/Ag-doped TiO_2 Nanocomposites. *Journal of the Brazilian Chemical Society* 2017; 28(12):2301-2312.

Publisher: Viser Technology Pte. Ltd.

URL: www.viserdata.com

Add.:21 Woodlands Close, #08-18,

Primz Bizhub SINGAPORE (737854)